
**The past is the key:
testing Earth models from seismic
waveform to continental uplift through
reconstructions of past mantle states**

Lorenzo Colli



München 2016

**The past is the key:
testing Earth models from seismic
waveform to continental uplift through
reconstructions of past mantle states**

Lorenzo Colli

Dissertation
an der Fakultät für Geowissenschaften
der Ludwig-Maximilians-Universität
München

vorgelegt von
Lorenzo Colli
aus Tradate (Italien)

München, den 06 Dezember 2016

Erstgutachter: Prof. Dr. Hans-Peter Bunge

Zweitgutachter: Prof. Dr. Andreas Fichtner

Tag der mündlichen Prüfung: 25 Januar 2017

Keine Metaphysik mehr!

Contents

Summary	xv
1 Introduction	1
2 Full waveform tomography of the upper mantle in the South Atlantic	5
2.1 Introduction	6
2.2 Method	8
2.2.1 The adjoint method	8
2.2.2 Numerical method and initial model	8
2.2.3 Crustal structure	9
2.2.4 Misfit function	9
2.2.5 Sensitivity kernels	9
2.2.6 Inversion procedure	9
2.3 Data	10
2.4 Results	11
2.4.1 3-D S-wave speed model	11
2.4.2 South America and Africa	11
2.4.3 South Atlantic Ocean	12
2.4.4 Waveform fit	12
2.4.5 Point spread functions	13
2.5 Discussion	14
2.5.1 Comparison with previous tomographic studies	15
2.5.2 Geodynamic implications	16
2.6 Conclusions	18
2.7 Acknowledgments	19
2.8 Appendix A. The adjoint equation	19
2.9 Appendix B. Supplementary data	19
2.10 References	19
3 Rapid South Atlantic spreading changes and coeval vertical motion	21
3.1 Introduction	22
3.2 Tectonic Setting in the South Atlantic Region	24
3.2.1 South Atlantic Spreading History	24

3.2.2	Topographic Evolution of the Andes	25
3.2.3	Regional Upper Mantle Seismic Structure	26
3.3	Torque Balance Estimates for the South American Plate	27
3.4	Asthenosphere Flow	29
3.5	Spreading Rate Changes and Coeval Epeirogenic Motions	30
3.6	Discussion	32
3.6.1	Unmodeled Effects	32
3.6.2	Implications	33
3.7	Conclusions	34
3.8	References	34
4	On retrodictions of global mantle flow with assimilated surface velocities	41
4.1	Introduction	42
4.2	Method	43
4.3	Results	44
4.3.1	Isoviscous Models	44
4.3.2	Layered Models	44
4.3.3	Long-Wavelength Perturbation	45
4.4	Discussion	46
4.5	Conclusion	48
4.6	References	48
5	On the ratio of dynamic topography and gravity anomalies	51
5.1	Introduction	52
5.2	Method	53
5.3	Results	54
5.4	Discussion	56
5.5	Conclusions	56
5.6	References	57
6	Retrodictions of late Paleogene mantle flow and dynamic topography	59
6.1	Introduction	61
6.2	Method	65
6.2.1	Forward equations	66
6.2.2	Adjoint equations	66
6.2.3	Inferences on the present-day thermal state of the mantle	67
6.2.4	Misfit function	68
6.2.5	Mantle Convection Model	71
6.2.6	Dynamic Topography: Semi-Analytical Solutions	73
6.3	Results	73
6.3.1	Hemispherical scale	73
6.3.2	Regional scale	81
6.3.3	Local scale	85

6.4	Discussion	85
6.4.1	Mantle flow velocities	87
6.4.2	Tomographic resolution and mantle convection lengthscales	87
6.4.3	Misfit function	88
6.4.4	Viscosity structure	89
6.4.5	Plate motion history	89
6.5	Conclusions	89
6.6	References	90
7	Outlook	101
	Acknowledgments	103

List of Figures

2.1	Topographic map of the South Atlantic	7
2.2	Age-area distribution of the ocean floor and residual basement depth	7
2.3	Observed and synthetic seismogram and computed phase difference	10
2.4	Sensitivity kernels	10
2.5	Ray coverage	11
2.6	Horizontal slices at 100 and 150 km depth	11
2.7	Horizontal slices at 200 and 250 km depth	12
2.8	Horizontal slices at 300 and 350 km depth	12
2.9	Horizontal slices at 400 and 450 km depth	13
2.10	Vertical profiles	13
2.11	Waveform comparison I	14
2.12	Waveform comparison II	15
2.13	Waveform comparison III	16
2.14	Waveform comparison IV	17
3.1	Maps of relevant South Atlantic datasets	23
3.2	South Atlantic spreading rate for different plate reconstruction models	25
3.3	Inferred Andean topographic evolution since Late Cretaceous	26
3.4	Horizontal slices of upper mantle seismic structure	26
3.5	Geometry and main features of the tectonic model and the scaling analysis	27
3.6	Predicted evolution of Andean paleoelevation	29
3.7	Main uplift events along Africa's South Atlantic margin	31
3.8	Plate configurations and ocean floor age	33
4.1	Evolution of the discrepancy for isoviscous models	44
4.2	Evolution of the discrepancy for two-layer models	45
4.3	Evolution of the discrepancy for three-layer models	45
4.4	3-D view of the temperature field of the three-layer model	46
4.5	Evolution of the discrepancy for models with a long-wavelength perturbation	47
5.1	Free-air gravity anomalies and low-pass-filtered geoid	53
5.2	Viscosity profiles and kernels	54
5.3	Three-dimensional view of assumed density anomaly	55

5.4	Modeling results	55
6.1	Topographic map of the Atlantic Ocean and adjacent continents	63
6.2	Shear wave velocity as a function of depth and temperature	67
6.3	Regression parameters	69
6.4	Misfit reduction	70
6.5	Radial viscosity and temperature profiles and dynamic topography kernels	71
6.6	3-D views of the reconstructed history AM_1	74
6.7	Temperature anomalies and velocity histograms	75
6.8	3-D views of the reconstructed history SM_1	78
6.9	3-D views of the reconstructed history AM_2	79
6.10	3-D views of the reconstructed history SM_2	80
6.11	Regional views of the reconstructed history AM_1	81
6.12	Regional views of the reconstructed history SM_1	82
6.13	Regional views of the reconstructed history AM_2	83
6.14	Regional views of the reconstructed history SM_2	84
6.15	Dynamic topography history at a number of selected locations	86

List of Tables

3.1	Flow Velocities Required by the Torque Balance	28
3.2	Calculated Poiseuille Mantle Flow Velocities	30
4.1	Model Parameters Employed in This Study	44
6.1	Model parameters	70
6.2	Summary of reconstructed histories	72

Summary

Numerical models of mantle convection have become increasingly more sophisticated in the last two decades and are growing in complexity. Unfortunately, the increase in resolution and the incorporation of new features based on empirical relationships, parametrizations and long-range extrapolations limit the predictive power of these models, while at the same time allowing for an easy fit of individual geophysical and geological datasets. This calls for a more thorough testing of geodynamic models and a shift in their use, from scenario calculations to explicit modeling of Earth's dynamics. A promising pathway to test geodynamic models relies on geodynamic retrodictions, that is reconstructions of past mantle flow states obtained using presently available information. They link explicitly assumptions and inferences from various fields of the Earth Sciences in a comprehensive Earth model based on the physics of mantle convection, thus highlighting their interrelations. Moreover, reconstructing the past history of mantle convection allows for a test of the underlying model against the geological record.

The emphasis on the cross-disciplinary testing of model results against observations marks the transition from numerical to observational geodynamics, of which this dissertation can be seen as a primer. Using the Atlantic realm as a case study, we collect a number of geophysical observations — from seismic structure to the history of plate motions, from epeirogenic movements to gravity anomalies — and bring them to bear. We first analyse them using theoretical considerations and analytical solutions, to gain some fundamental insight and formulate clear geophysical hypotheses. We then proceed to formally solve the geodynamic inverse problem, obtaining the first retrodictions of geodynamically plausible mantle flow in the Atlantic region.

Chapter 1

Introduction

The last century has seen considerable developments in our understanding of the Solid Earth. The theory of plate tectonics provides a consistent kinematic framework for the horizontal motion of the Earth's surface and a unifying explanation for the magnetic anomalies of the sea floor and for most of Earth's seismicity and volcanic activity. Progress has also been made with respect to Earth's dynamics, with the consolidation of the concept of mantle convection. It posits that the Earth's mantle is slowly deforming through solid-state creep caused by thermally-induced buoyancy anomalies, with tectonic plates being the upper thermal and mechanical boundary layer of this convective system. The theory of mantle convection provides the forces necessary to drive plate tectonics and a means to cool the Earth's core, thus powering its dynamo.

Geodynamic work in the past decades has explored planetary convection, starting from the fundamental fluid dynamic properties of a highly viscous Stokes flow at the planetary scale and moving on to first order questions such as the heating mode of the mantle, its radial viscosity structure, the role of phase transitions and the link with the internal structure of the Earth as imaged by seismic tomography. Indeed, a thermal interpretation of seismic anomalies reveals the presence of long-subducted oceanic plates, now sinking towards the core-mantle boundary, and hot upwelling currents, rising up and deforming the surface of the Earth.

While many fundamental aspects of planetary convection are now clear, a detailed technical understanding of convection for the Earth's mantle is still lacking, for two main reasons: On the one hand the real Earth is a complex system, its various components interacting over spatial and temporal scales that span many orders of magnitude, thus limiting our ability to arrive at satisfactory approximations or syntheses. On the other hand, Solid Earth's dynamics are nearly impossible to probe directly, partly because the mantle is for the most part physically inaccessible and partly because it evolves over timescales well beyond a human lifespan.

Numerical geodynamics has responded to these issues mostly by developing more com-

plex mantle convection models — which, in theory, should make them more Earth-like — and by using them in simple scenario calculations. Many of the added complexities, features like non-linear rheology, temperature-dependent viscosity, thermochemical flow and melting, are frequently based on ad-hoc parametrizations and long-range extrapolations of empirical equations, and very rarely on first principle physics. Geodynamic models thus have an increasingly large number of free parameters and are at serious risk of being over-fitted. It is thus of fundamental importance to test mantle convection models and the assumptions and approximations they are based upon.

Testing a model usually involves the comparison of model predictions for the future evolution of the system against direct observations. An estimate for the present-day state of the Earth can be obtained by combining the elastic wavespeed structure imaged by a seismic tomography with models of mantle mineralogy. A model Earth can thus be initialized and future predictions can be computed. Mantle convection, unfortunately, evolves over timescales of many thousands of years and testing such future predictions is completely impractical. A way around this limitation requires to recast mantle convection as an inverse problem, reconstructing past states of the Earth’s mantle in order to compare them against direct geophysical and geological observations.

In the last fifteen years there have been significant advancements in our ability to solve geophysical inverse problems with the development of the adjoint method for geodynamics and for seismology. At its core, the adjoint method is a technique that allows the optimization of the model parameters with respect of a set of observables. In a seismic tomography the model is a 3D elastic structure while the observations are in the form of seismograms. In geodynamics, instead, the adjoint method allows to find an earlier flow state that naturally evolves into its known present-day state and, as a consequence, the complete history of mantle convection.

This dissertation explores various aspects of geodynamic retrodictions in the broad context of the Earth Sciences. We start in chapter 2 by introducing a seismic tomography for the South Atlantic region. It has been obtained with a formulation of the adjoint method based on a full-waveform approach, which takes into account a more complete physics of wave propagation than classical raypath tomography and allows the extraction of more information from each seismogram. As such, it naturally yields higher resolution tomographic images, in particular in regions of poor coverage such as the South Atlantic. The resulting seismic structure shows a peculiar change in the pattern and amplitude of seismic anomalies, which led us to the formulation of a working hypothesis: the sublithospheric mantle is characterized by a relatively thin asthenosphere of strongly reduced viscosity.

In chapter 3 we discuss how this hypothesis can explain a number of observations for the tectonic history of the South Atlantic basin and its surrounding continents. In particular, we show with simple analytical solutions that temporal changes of pressure-driven asthenospheric flow imply a correlation of horizontal and vertical plate motions, thus link-

ing the rapid spreading rate changes of the Mid-Atlantic Ridge with epeirogenic movements in southern and central Africa. The simple analysis performed in this chapter is very important: not only we have a confirmation that our hypothesis is, to a first approximation, correct, but by providing a strong insight into the basic physics of this system it allows us to approach more confidently more complex models.

Chapter 4 presents a theoretical study on the role of assimilated horizontal surface velocities in retrodictions of global mantle flow. Mantle convection is chaotic, and as such it is affected by the *butterfly effect*: any error in the initial condition, no matter how small, increases exponentially in time causing the reconstructed history to diverge from the true one, with clear consequences for the long-term predictability of mantle convection. Retrodictions of mantle convection, however, are always performed in the presence of abundant knowledge for the past history of plate motion. Here we show with synthetic *twin experiments* that assimilation of past plate motions prevents the chaotic long-term drift of unconstrained mantle convection, allowing the reconstruction of past flow states for periods comparable to the available time span of past plate motion models.

As the final goal of a geodynamic retrodiction is to compare model results against direct observations, it is important to make sure that the theoretical model, in particular its assumptions and approximations, are appropriate to understand and interpret the observation. Two primary observables for the dynamics of the solid Earth are its dynamic topography and its gravitational field. Chapter 5 discusses their relationship and illustrates how an incomplete model can lead to a fundamental misuse of the observation. In particular, simple analytical models based on an infinite half space approximation predict a simple relationship between gravity anomalies and dynamic topography and imply a dynamic topography characterized by very small amplitudes. More complete models that take into account Earth's sphericity, the finite thickness of the mantle and its viscous layering, instead, show that the relationship between gravity anomalies and dynamic topography is complex, thus limiting the usefulness of gravity anomalies as predictors for dynamic topography, and allow for relatively large amplitudes of dynamic topography without a corresponding gravitational fingerprint.

Finally in chapter 6 we present the first retrodictions of geodynamically plausible mantle flow in the Atlantic region, going back in time to the late Paleogene. Past flow states are reconstructed uniquely using the geodynamic adjoint method thanks to the assimilation of past plate motions, as discussed in chapter 4. The target present-day structure is obtained using, together with others, the tomographic model presented in chapter 2. Moreover we assume a thin sub-lithospheric low viscosity zone, as suggested by our analysis in chapter 3, and we explore the history of dynamic topography implied by the reconstructed flow states using global, self-gravitating, viscously stratified Earth models, in accord with the results of chapter 5.

Chapter 2

Full waveform tomography of the upper mantle in the South Atlantic region: Imaging a westward fluxing shallow asthenosphere?

This chapter was published in the Journal “Tectonophysics” in 2013. It presents a seismic model for the upper mantle in the South Atlantic region obtained with a full-waveform approach based on the adjoint method, and discusses its possible implications for a thin and low-viscosity asthenosphere.



Full waveform tomography of the upper mantle in the South Atlantic region: Imaging a westward fluxing shallow asthenosphere?

Lorenzo Colli^{a,*}, Andreas Fichtner^b, Hans-Peter Bunge^a

^a Department of Earth and Environmental Sciences, Ludwig Maximilian University, Theresienstrasse 41, 80333 Munich, Germany

^b Department of Earth Sciences, ETH Zurich, Sonneggstrasse 5, 8092 Zurich, Switzerland

ARTICLE INFO

Article history:

Received 23 July 2012

Received in revised form 18 June 2013

Accepted 19 June 2013

Available online 28 June 2013

Keywords:

Full waveform inversion

Adjoint method

Seismic tomography

Pressure-driven asthenospheric flow

Upper mantle convective planform

ABSTRACT

A prominent feature of the South Atlantic region is its strongly asymmetric residual bathymetry across the ocean basin. It has been suggested that the residual bathymetry is dynamic in nature, arising from the large slow velocity seismic anomaly located in the lower mantle beneath the African plate. Unfortunately, the pattern of mantle heterogeneity particularly in the upper mantle is not well known owing to the sparsity of seismic stations and the existence of large aseismic regions on the African and South American plates. Here we present a new seismic tomographic study of the South Atlantic upper mantle. Our model is based on a full seismic waveform inversion of ≈ 4000 high-quality seismograms for isotropic 3-D seismic structure using a powerful adjoint methodology capable of extracting maximum information from each seismogram. The theory requires simulation of seismic wave propagation in 3-D heterogeneous earth models computed with a spectral-element method where the differences between observed and synthetic seismograms are quantified using phase misfits obtained through a time–frequency transform. The model images a continuous channel of pronounced slow seismic velocity in the shallow sublithospheric mantle between ≈ 150 and ≈ 300 km depth that branches in between the cratonic roots under the African and South American continents. At greater depth, below 300–350 km, the slow anomalies are less pronounced and a change in the convective planform is indicated by isolated, round shaped patches in an overall faster mantle. It is possible that the depthwise change of the convective planform from vertical to horizontal advection of hot buoyant material in a low viscosity asthenosphere can reconcile the anomalous residual bathymetry in the region, and we present a simple fluid dynamic model of pressure driven flow to assess the feasibility of this scenario.

© 2013 Elsevier B.V. All rights reserved.

1. Introduction

The South Atlantic region is characterized by major structural elements that include the conjugate margins of South America and Africa with their adjacent cratonic cores, the Parana and Etendeka continental flood basalts and their hotspot tracks along the Walvis Ridge and Rio Grande Rise, as well as the Tristan da Cunha, St. Helena and Ascension hotspots (Fig. 1). The presence of well preserved magnetic isochrons (Fig. 2a), moreover, allows one to constrain the opening history of the basin, so that residual ocean floor topography can be assessed after removing thermal cooling effects within the oceanic lithosphere. An outstanding observation from the residual topography maps (Fig. 2b) is the existence of strongly anomalous bathymetry cutting across the structural elements. Elevated topography,

termed the African superswell by Nyblade and Robinson (1994), consists of uplifted portions of the African continent and areas of abnormally high bathymetry in the south-eastern Atlantic, while much of the south-western Atlantic especially in the Argentine Basin is abnormally deep.

Pronounced residual bathymetry in the South Atlantic implies that significant topography must be supported by heterogeneity beneath the tectonic plates. Whether this topography originates from upper mantle flow directly beneath the lithosphere, or whether it reflects dynamic support of deeply seated buoyancy in the lower mantle, remains unclear. Global tomography models (e.g., Grand, 2002; Grand et al., 1997; Ritsema et al., 2011; Simmons et al., 2007) persistently image slow seismic velocities in the lower mantle beneath the African plate, and a substantial portion of this wave speed reduction is probably due to highly elevated temperature (Schuberth et al., 2009a, 2009b) so that the region may act as a source of considerable thermal instabilities.

Anderson (1982) noted that the sub-African mantle had long been shielded from subduction by the former supercontinent Pangea.

* Corresponding author. Tel.: +49 89 2180 4215; fax: +49 89 2180 4205.

E-mail addresses: lorenzo.colli@geophysik.uni-muenchen.de (L. Colli), andreas.fichtner@erdw.ethz.ch (A. Fichtner), hans-peter.bunge@geophysik.uni-muenchen.de (H.-P. Bunge).

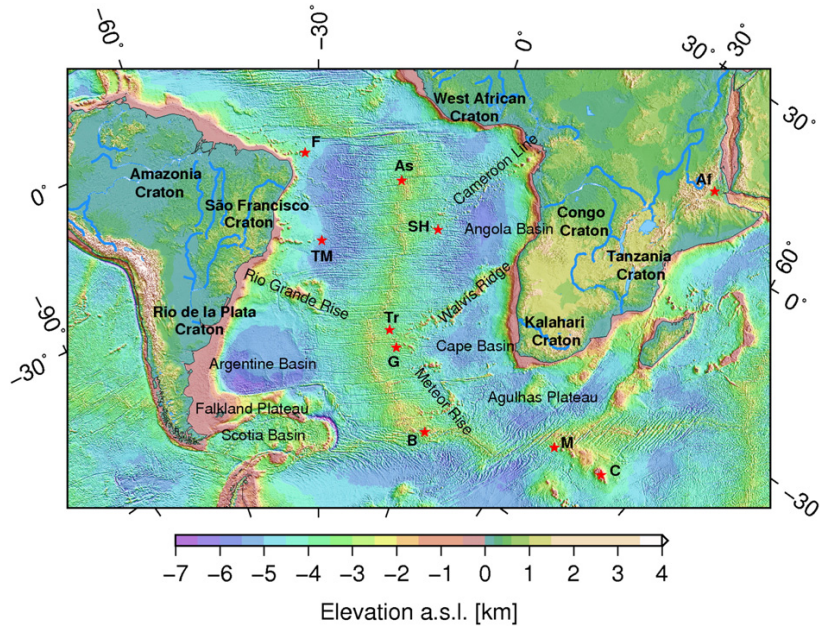


Fig. 1. Topographic map of the South Atlantic and adjacent continents from EOTPO1 (Amante and Eakins, 2009), annotated with major structural elements cited in the text. Oblique Mercator projection: central parallel passes through the points (30°S, 30°W) and (0°S, 60°E), projection centred on (28.024°S, 7.204°W). Craton names are boldface, while stars denote prominent hotspots (F: Fernando de Noronha; As: Ascension; Af: Afar; SH: Saint Helena; TM: Trinidad and Martim Vaz; Tr: Tristan da Cunha; G: Gough Island; B: Bouvet Island; M: Marion; C: Crozet Islands).

Significant hot thermal upwellings are thus expected in the region, in agreement with inferences that Africa experienced greater uplift in the Tertiary than other continents (e.g., Burke and Gunnell, 2008). A variety of geodynamic models (e.g., Forte et al., 2010; Gurnis et al., 2000; Lithgow-Bertelloni and Silver, 1998; Moucha and Forte, 2011) suggest deep mantle heterogeneity as a plausible cause for high topography in Africa and the South Atlantic, and that the entire region is influenced by a major mantle convection cell (Husson et al., 2012).

The African plate contains many volcanic centres that may be interpreted as the surface expression of mantle plumes rising from the lower mantle, but the path of deep material taken on its passage

from the lower into the upper mantle, and its advective redistribution within the asthenosphere and toward the Mid-Atlantic ridge system is not well known. It must be inferred from seismic studies.

Upper mantle structure in the South Atlantic region remains poorly studied owing to the sparse distribution of seismic stations and the existence of large aseismic areas on the African and South American plates. Temporary deployments of seismometers were carried out at some localities, for example across the shields in southern Africa, to provide detailed seismic images of the crust and upper mantle (e.g., Chevrot and Zhao, 2007; Freybourger et al., 2001). Tomographic studies have revealed thick, seismically fast

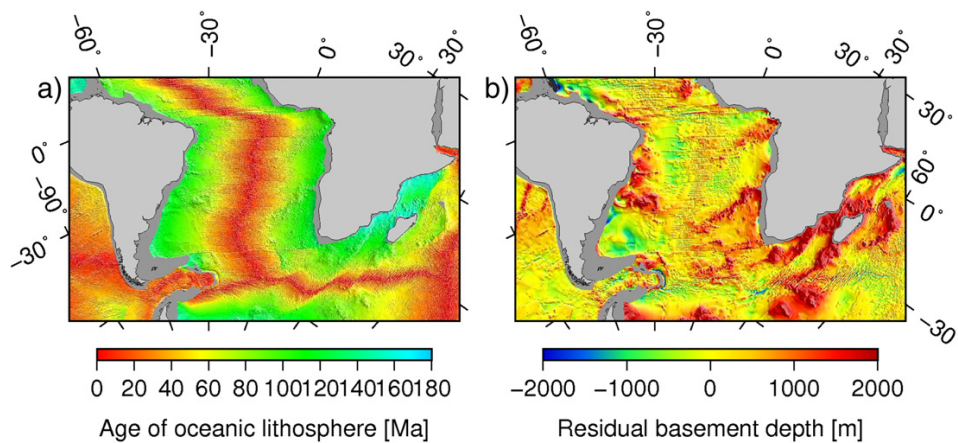


Fig. 2. Left: age-area distribution of the ocean floor from Müller et al. (2008); right: residual basement depth grid computed by calculating the difference between the predicted basement depth and the sediment unloaded basement depth. Predicted basement depth is obtained by applying Crosby et al.'s (2006) North Pacific thermal boundary layer model to the age-area distribution from Müller et al. (2008). Oblique Mercator projection. Note the anomalous bathymetry cutting across the regional structural elements, with excess topography in correspondence with the African superswell and anomalously high bathymetry in the south-eastern Atlantic.

“keels” under the cratonic regions of Africa, with slow structure prevailing elsewhere (e.g., Priestley et al., 2006; Ritsema et al., 1999). Many seismic studies relied on surface wave data (Pasyanos and Nyblade, 2007; Ritsema and van Heijst, 2000) for spatial coverage, mapping significant shear velocity features down to depth levels of 200 km and corresponding mostly to cratonic structures. Maps of upper mantle anisotropy (Debayle et al., 2005; Priestley et al., 2008; Sebai et al., 2006) have yielded additional constraints on material flow directions in the region and have concluded that there is a strong and spatially complex azimuthal anisotropy in the African lithosphere, while the signal is weaker and simpler in the asthenosphere below.

While raypath tomography is progressing, a refined physical modelling of seismic wave propagation has become possible: finite-frequency effects, such as wave scattering and wavefront healing, bear significantly on the behaviour of seismic waves, and should be taken into account to improve the seismic images. To yield synthetic seismograms, one must compute the propagation of the full wavefield in a three-dimensional heterogeneous Earth model. Finite-frequency effects must also be accounted for in the inversion procedure and in the construction of effective misfit functions.

Full waveform tomography, made possible by the dramatic gain of computational resources in recent years, takes advantage of a numerical solution of the wave equation to account for the effects of 3-D heterogeneous seismic structures on wave propagation. The numerical solution allows one to treat simultaneously all direct, reflected and scattered body and surface waves, thus considerably increasing the exploitable information carried by each seismogram. Here we employ this technique to invert for seismic structure in the South Atlantic region, which is characterized by scarcity of high quality seismograms. In order to best extract information and invert for 3-D seismic structure, a suitable misfit function needs to be used. To this end, we apply a time–frequency misfit (Fichtner et al., 2008) for comparison of observed and synthetic data, together with an efficient adjoint method (Fichtner et al., 2006) for the iterative correction of model parameters.

2. Method

2.1. The adjoint method

The aim of our present work is to obtain the speed of propagation of seismic waves in the South Atlantic upper mantle region. As direct, in situ measurements of the seismic wave speed are impossible, we have to resort to an indirect one. By exploiting the data recorded at seismic stations across the region of interest, we can obtain a synthetic model of the upper mantle seismic structure, defined by a set of parameters \mathbf{p} , that can reproduce the observed ground motion. We thus want to minimize the misfit between real data recorded at seismic stations and synthetic data generated with our model.

To quantify the misfit between synthetic and observed seismograms, one must establish a misfit function $\chi(\mathbf{u}, \mathbf{p})$ that depends on the model parameters \mathbf{p} and the synthetic seismogram \mathbf{u} generated using those parameters. It is possible to improve the synthetic model starting from an initial guess for the model parameters \mathbf{p}_0 that produced the mismatched initial solution \mathbf{u}_0 . One then calculates a parameter correction \mathbf{d} which minimizes the misfit function by gradient descent, that is by computing the total derivative (Fréchet derivative) of χ with respect to the model parameters \mathbf{p} :

$$D_{\mathbf{p}}\chi(\mathbf{u}, \mathbf{p})(\mathbf{d}) = \partial_{\mathbf{u}}\chi(\mathbf{u}, \mathbf{p})D_{\mathbf{p}}\mathbf{u}(\mathbf{d}) + \partial_{\mathbf{p}}\chi(\mathbf{u}, \mathbf{p})(\mathbf{d}). \quad (1)$$

While the partial derivatives of χ can be computed quite easily, the computation of $D_{\mathbf{p}}\mathbf{u}(\mathbf{d})$, that is the variation of the synthetic seismogram \mathbf{u} due to a change \mathbf{d} in the model parameters, is involved.

Classical finite differencing techniques can be employed, but they become infeasible in the case of a large parameter space, like the one needed to properly describe the seismic structure of the Earth. It is here that the adjoint method provides an elegant way to compute the derivative with respect to the parameters by combining the synthetic forward solution \mathbf{u} with an ancillary function ψ , the solution of the adjoint equation.

The adjoint technique is a general and versatile method to compute partial derivatives with respect to model parameters, and has been implemented for a range of geophysical applications that include, in addition to seismic tomography, lithosphere, mantle and core dynamics (Bunge et al., 2003; Chen et al., 2007; Fournier et al., 2010; Iaffaldano et al., 2007; Tape et al., 2009; Tarantola, 1988; Tromp et al., 2005). The adjoint method exploits the fundamental fact that the change in the observed quantity generated by a change in the model parameters is governed by the physics of the system. In the case of seismology, a change in the elastic properties of some part of the model causes the wavefield passing through that region to be reflected, refracted and diffracted differently, leading to a variation in the synthetic seismograms. This perturbation of the wavefield is still a wavefield itself, and propagates in accordance to the constraints of the wave equation. It is possible to backtrack the place of origin of the perturbation by solving for a subsidiary wavefield subject to a set of equations, called adjoint equations, that are derived from the original wave equation. The adjoint equations are still of the wave type, and the source term in the adjoint equation is derived from the misfit between observed and synthetic seismograms (further details are available for the interested reader in Appendix A). The choice of the misfit function χ is thus particularly important: since we are using a first-order algorithm, a misfit function which relates linearly to perturbations in the parameters will give a faster and smoother convergence.

We next present the adjoint problem for continental-scale full waveform tomography and describe our choice for the misfit function.

2.2. Numerical method and initial model

As we mentioned before, it is important to compute the propagation of the full wavefield through the 3-D heterogeneous seismic model, in order to avoid artefacts generated by simplifying approximations. Since this is beyond an analytic solution, simulation of elastic wave propagation and computation of Fréchet kernels is done numerically with the code SES3D (Fichtner et al., 2009), implemented on dedicated capacity computing infrastructure (Oeser et al., 2006). The similarity between the original wave equation and its adjoint equation implies that the same code used to solve for the forward wavefield can be used, with only minor changes, to solve for the adjoint field. SES3D is based on the spectral-element method and operates in a spherical section. The unphysical boundaries of the spherical section cause spurious reflections that prevent a meaningful comparison between synthetic and observed data. In order to avoid these reflections we absorb waves close to the boundaries by using the anisotropic perfectly matched layer technique proposed by Teixeira and Chew (1997) and Zheng and Huang (1997). We employ a spherical section of $140^\circ \times 80^\circ \times 1440$ km going from the surface to the mid-mantle, divided into nearly 165,000 elements that are $1.5^\circ \times 1.6^\circ \times 40$ km. Inside each element the dynamic fields are approximated by degree 6 Lagrange polynomials, for a total of nearly 30×10^6 gridpoints. The minimum theoretical period for this grid is around 55 s. We implement Ritsema's s20rts (Ritsema and van Heijst, 2004) as our initial model, to speed up convergence, so that the longest wavelength features of the South Atlantic upper mantle are already present in the initial model. This ensures an acceptable initial fit between synthetic seismograms and data and allows us to effectively correct the model.

2.3. Crustal structure

The long-period (120 s and longer) waves used in this study are influenced by the crust without being able to resolve its fine layering. The only way to represent the crustal structure accurately is to honour all its thin layers within the spectral-element mesh, which results in an extremely fine mesh. However, as the dominant wavelength is roughly 400 km in our study, such fine mesh would waste computational time, both because the wavefield is well represented on a coarser grid, and because the waves are not as sensitive to each thin layer of the model as they are to its long-wavelength features. We therefore implement a smooth long-wavelength equivalent (Fichtner and Igel, 2008) of the MDN crustal model by Meier et al. (2007) constructed explicitly to provide a crustal correction for long-period tomography. This allows us to use larger elements without introducing artefacts due to the absence of a proper crust. Together with the rest of the model, we then improve the crustal model iteratively even if it remains a long-wavelength equivalent. The upper 50 km of our model thus cannot be interpreted in terms of real-earth seismic structure.

2.4. Misfit function

As stated before, it is important to choose a suitable misfit function for the quantification of the differences between synthetic and observed seismograms, in order to extract the maximum amount of meaningful information from each seismogram and to improve the convergence rate. A direct comparison of the seismograms' amplitudes (e.g., the L_p norm of the difference $\mathbf{u}^0 - \mathbf{u}$) is unsatisfactory, since amplitude is influenced non-linearly by seismic anomalies, in particular by local anomalies near the receiver. A small variation in seismic velocity, producing a minor time shift of the waveform, can therefore induce a large instantaneous amplitude misfit even if the total energy arriving at the receiver remains almost constant; moreover, source inversions are often not accurate enough for the needs of an amplitude tomography.

A better choice is the use of the phase difference between synthetic and observed seismograms. This measure, akin to a measure of instantaneous time delay but performed in a time–frequency domain, is more linearly related to seismic anomalies and less degraded than amplitude by interference of different waves. Hence we disregard amplitudes and use phase differences to quantify the misfit between synthetic and observed waveforms: given an observed seismogram $u_i^0(t)$, where the index i runs over the three components, and the corresponding synthetic seismogram $u_i(t)$, we map the seismograms into the time–frequency domain using the windowed Fourier transform

$$\tilde{v}(t, \omega) = F_h[v](t, \omega) := \frac{1}{\sqrt{2\pi}} \int_{-\infty}^{+\infty} v(\tau)h(\tau-t)e^{-i\omega\tau} d\tau, \quad (2)$$

with $h(t) = (\pi\sigma)^{-1/4}e^{-t^2/2\sigma^2}$ and σ set approximately equal to the dominant period of the considered waveform – in our present study, we used a value of 100 s. We then write the transformed observed and synthetic seismograms in exponential form, making explicit their phase and magnitude

$$\tilde{u}_i^0(t, \omega) = |\tilde{u}_i^0(t, \omega)|e^{i\phi_i^0(t, \omega)}, \quad \tilde{u}_i(t, \omega) = |\tilde{u}_i(t, \omega)|e^{i\phi_i(t, \omega)}, \quad (3)$$

and define a phase misfit E as the weighted L_2 norm of the phase difference $\phi_i^0(t, \omega) - \phi_i(t, \omega)$:

$$E^2(u_i^0, u_i) := \int_{\mathbb{R}^2} W^2(t, \omega) [\phi_i^0(t, \omega) - \phi_i(t, \omega)]^2 dt d\omega. \quad (4)$$

$W(t, \omega)$ is a positively defined weighting function that allows us to select and weigh the various waveforms both time- and frequency-wise, excluding phase jumps and reducing the influence of seismic noise, and thus enhancing convergence. In practice it consists of the sum of various time windows that select the usable portion of each waveform and decay to zero outside this region. Each time window is multiplied by a constant between 0 and 100 that upweighs waveforms with a better signal-to-noise ratio and less frequent station–event combinations (e.g., north–south trending over east–west trending). $W(t, \omega)$ is constant in frequency between 1/300 and 1/120 Hz and decays exponentially outside this interval.

A complication of the phase misfit is given by the possibly discontinuous nature of the phases $\phi_i^0(t, \omega)$ and $\phi_i(t, \omega)$, which implies discontinuities up to $\pm 2\pi$ for the phase difference $\Delta\phi_i = \phi_i^0(t, \omega) - \phi_i(t, \omega)$. Some of these phase jumps are contingent and can be removed by calculating the phase difference via the Fourier transform of the correlation function (Fichtner et al., 2008). In other cases, when data and synthetics are too dissimilar and out of phase, discontinuities are fundamental in nature and cannot be removed: they are symptomatic of cycle skips between synthetics and real data, and they signal a point where the misfit function is no longer physically meaningful. These jumps must be excluded by tapering in the time–frequency domain via a proper choice of $W(t, \omega)$.

The total misfit χ is computed as a sum of each individual phase misfit over all the seismograms and all the events.

2.5. Sensitivity kernels

Applying the above methodology to each individual event we obtain the total derivative of the misfit function with respect to the model parameters (see Eqs. (1) and (A.11)) for that event, also called misfit sensitivity kernel, an example of which is given in Fig. 4. The complex kernel structure arises from the sum of different concomitant factors: first and foremost the complexity of each single-frequency source–receiver kernel, then their interfering superposition both frequency- and receiver-wise. Due to finite-frequency effects a kernel obtained using a single frequency of a single seismogram already has a fully developed 3-D structure: the region with erroneous elastic parameters that cause the discrepancy between the observed and the synthetic seismogram may lie well outside the theoretical 1-D raypath. Moreover, waves travelling with different frequencies are characterized by Fresnel zones of different widths, and thus grant different spatial resolutions. In addition it is well known that higher frequency surface waves are more sensitive to shallower anomalies, resulting in a natural overall variation with s depth of the kernel's resolution. When adding the contribution of all the receivers, the single kernels will interfere constructively in the regions that need to be corrected, and they will interfere destructively in those regions that are already well characterized. This trend is reinforced and enhanced when the kernels obtained from all events are summed, giving the direction \mathbf{d} of the total derivative of our chosen misfit function with respect to the model parameters.

2.6. Inversion procedure

The inversion procedure consists thus of the following steps: (1) the propagation of the full wavefield in the current n -th model, defined by the set of parameters \mathbf{p}_n , is computed; (2) the difference between synthetic and observed seismograms is quantified using the phase misfit, obtaining the source term for the adjoint equation; (3) the adjoint equation is solved and the total derivative of the misfit function is calculated; (4) an optimal step length is determined using a parabolic line search: assuming the misfit function $\chi(\mathbf{u}, \mathbf{p})$ to be quadratic in \mathbf{p} near the best model \mathbf{p}_{min} , we fit a quadratic polynomial in the trial step length s through the values of misfit for the current n -th model \mathbf{p}_n and the two trial models $\mathbf{p}_n + s_1\mathbf{d}$ and $\mathbf{p}_n + s_2\mathbf{d}$. The values

10 2. Full waveform tomography of the upper mantle in the South Atlantic

30

L. Colli et al. / Tectonophysics 604 (2013) 26–40

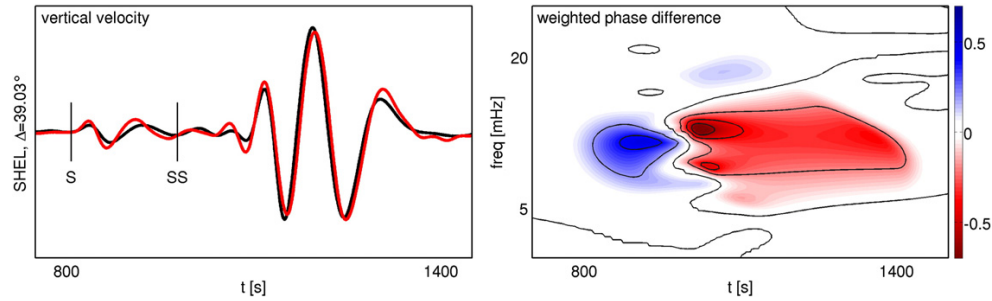


Fig. 3. Left-hand panel: vertical-component velocity seismograms from an event in Tanzania recorded at the station SHEL on Saint Helena. The recorded seismogram is plotted as a thick black line while the synthetic is plotted as a thick red line. Right-hand panel: weighted phase difference $W(t, \omega)\Delta\phi(t, \omega)$ corresponding to the seismogram on the left-hand side. Contour lines are plotted at multiples of 20% of the maximum value. Both S and SS modelled body waves arrive early relative to the observed phases and show a positive phase difference, while the Rayleigh wave is slightly late and shows an overall negative phase difference. Notice however the frequency dependence of the phase difference: the time of maximum phase delay at medium frequencies is a time of maximum phase advance at higher frequencies.

of the trial step lengths s_1 and s_2 are assigned arbitrarily on the base of physical intuition, direct experience with the inversion and rough quantitative analysis of the misfits. In practice they are such that the maximum resulting correction is between a fraction of a percent and a few percent in wavespeed. Their values tend to decrease with further iterations, as the model gets better and smaller corrections are needed. Finally, (5) a new $n + 1$ -th model is obtained by applying the computed correction to the current n -th model. These steps are repeated iteratively until the differences between synthetic and observed seismograms become sufficiently small.

3. Data

We selected 68 events occurring between 2007 and 2011 for a total of 3916 seismograms, mainly vertical-component (Fig. 5). About 95% of the data comes from permanent networks operated by IRIS, GEOSCOPE, USGS, AfricaArray, University of Sao Paulo and Universidad de Chile, while the remaining 5% comes from the Chile RAMP and Sierras Pampeanas temporary networks.

In order to neglect finite-source effects we accepted only events whose magnitude is smaller than M_s 6.9. Moreover, we discarded events with less than 20 high-quality recordings in our region of

interest: the adjoint method is maximally efficient when there is a large seismogram-to-event ratio, and our computational resources are limited.

The majority of the waveforms consist of fundamental-mode surface waves, which have the best signal-to-noise ratio. The remaining waveforms are higher-mode surface waves and S body waves. We individually upweigh less frequent waveforms in order to keep the model unbiased toward a particular seismic phase, and to improve the resolution at depth. We used surface waves recorded at epicentral distances between 5° and 125° , while we used only direct body waves recorded at distances of no more than 40° because beyond that distance the synthetic body wave is influenced by the unphysical domain boundary of our mesh at 1440 km depth. For this reason we don't have a good resolution in the lower mantle.

Hypocentre coordinates and moment tensor components for all 68 events were taken from the Centroid Moment Tensor catalogue (<http://www.globalcmt.org>). We decided against inverting for source parameters for two main reasons: on the one hand, we use rather long-period waves, so our inversion is not affected much by errors in them; on the other hand for our inversion we would be able to use waves coming only from limited values of azimuths, since the overwhelming majority of the events is close to the border of our

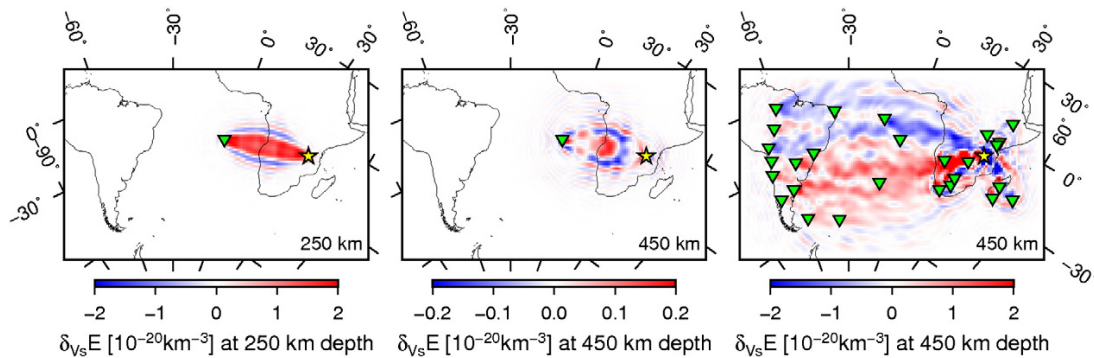


Fig. 4. Left-hand panel: horizontal slice at 250 km depth through the sensitivity kernel calculated with the adjoint source derived from the waveforms shown in Fig. 3. The position of the epicentre is marked by a yellow star while the station SHEL is denoted by a green triangle. The regions in blue are those that can possibly be generating the mismatch between the synthetic and the observed seismogram because of a too high s-wave speed, while those in red have a possibly too slow s-wave speed. This relatively shallow depth is mainly illuminated by the surface wave, that was characterized by a phase delay. The kernel thus points to an increase of the s-wave speed in the region between the station and the receiver that is crossed by the main wave, with alternating rings of slow and fast scatterers surrounding this region. Central panel: horizontal slice at 450 km depth through the same sensitivity kernel of the left-hand panel. This portion of the model is illuminated by both the surface and the body waves, causing a more complex pattern of slow and fast regions. Right-hand panel: horizontal slice at 450 km depth through the sensitivity kernel calculated for the same event but using all available waveforms. Oblique Mercator projection.

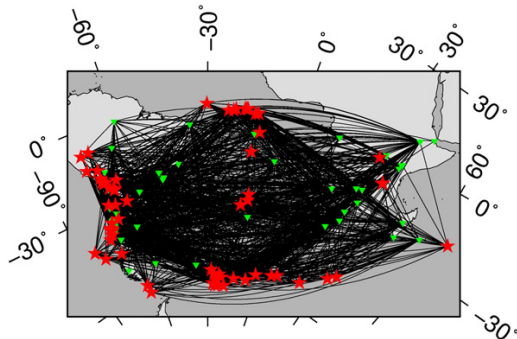


Fig. 5. Ray coverage for the 3916 seismograms used in this study. Epicentres are marked by red stars while stations are denoted by green triangles. Oblique Mercator projection.

computational domain. Inverting for hypocentre coordinates and moment tensor components would result in a misfit reduction without implying a real improvement of the model.

4. Results

4.1. 3-D S-wave speed model

Using the method described in Section 2 we inverted the data presented in the last section for isotropic upper mantle seismic structure in the South Atlantic region. The resulting isotropic model after five iterations is presented in Figs. 6–10.

At a depth of 100 km (Fig. 6) the model is mainly influenced by the lithosphere's compositional and structural variations, both under the continents and under the ocean. In continental regions cratons stand out as fast anomalies surrounded by relatively slower regions. Moving into the oceanic regions, the thick and relatively fast oceanic lithosphere near the continents gives way to slower mantle material towards the mid-oceanic ridges. The main exception is given by the two slow anomalies extending from the Mid-Atlantic Ridge towards South America on one side and towards Africa on the other.

Deeper down in the mantle (Figs. 6, 7 and 10) the fast anomalies related to the continental cratons become smaller and fainter, while

slow velocities are overall dominant, in particular in the sub-oceanic mantle where the slow velocity anomalies are mainly elongated at an angle with the strike of the Mid-Atlantic Ridge. Between 200 and 300 km depths some slow regions protrude under the continents, prolongations of the slow anomalies under the Rio Grande Rise and the Walvis Ridge. Under Africa a slow anomaly weaves its way between the fast velocity anomalies of the Kalahari and the Congo cratons, connecting the slow region around Afar with the slow anomalies under the Atlantic Ocean. Under South America the slow velocity anomaly splits into two branches, one protruding northwards under central Brazil while the other extending westward under central Argentina and Chile. Below 300 km depth (Fig. 8) slow anomalies are no longer dominant, with also a distinct change in their shape from elongated to rounded.

4.2. South America and Africa

Two very fast velocity anomalies in the South American lithosphere between 100 and 150 km (Fig. 6) depths are located under the Amazonia and São Francisco cratons in the northern part of the continent (see profile A–A' in Fig. 10), while a moderately fast and shallower anomaly is found under the Rio de Plata craton (see profiles B–B' and C–C'). The southern part of the continent including the continental platform is instead underlain by moderately fast seismic anomalies and is divided from the northern faster regions by a slower east–west anomaly around 40° S (see profile D–D'). Deeper in the mantle the fast cratonic anomalies weaken and reduce in size, giving space to an anomaly starting from the coast off southern Brazil and extending more and more northwards under the continent with increasing depth. This slow anomaly branches off westward under Bolivia, reaching towards the border between Chile and Peru. A slow anomaly appears with depth also under the coast of Uruguay and Argentina, connecting the slow anomaly off the coast of southern Brazil with the slow anomaly around 40°S under Argentina. An isolated slow anomaly appears also near the eastern tip of Brazil, possibly due to the Fernando de Noronha hotspot. The Nazca slab appears as a set of discontinuous moderately fast regions under Peru, Chile and Argentina.

The lithosphere under Africa is also characterized by two large and fast anomalies corresponding to the Congo (see profiles A–A' and E–E') and Kalahari (see profiles C–C') cratons, while the Tanzania craton is underlain by a moderately fast anomaly only at shallow depths (see profiles B–B'). The centre of the fast anomaly corresponding to the

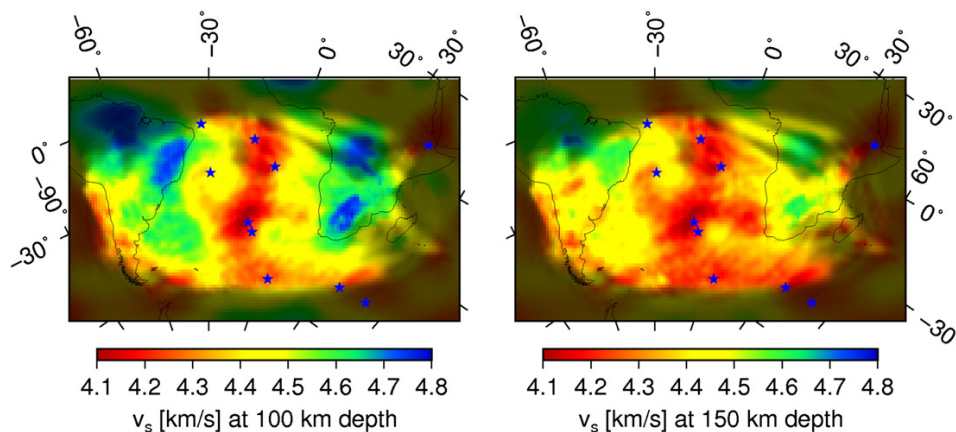


Fig. 6. Horizontal slices through the final tomographic model at 100 km depth (left) and 150 km depth (right). Oblique Mercator projection. At these depths continental cratons stand out as fast anomalies surrounded by relatively slower regions, while variations of seismic velocity in the oceanic realm are mainly due to the thermal cooling of the lithosphere, with fast anomalies near the continents varying smoothly into slower ones towards the mid-oceanic ridges. The main exception is given by the two slow anomalies extending from the Mid-Atlantic Ridge towards South America on one side and towards Africa on the other.

12 2. Full waveform tomography of the upper mantle in the South Atlantic

32

L. Colli et al. / Tectonophysics 604 (2013) 26–40

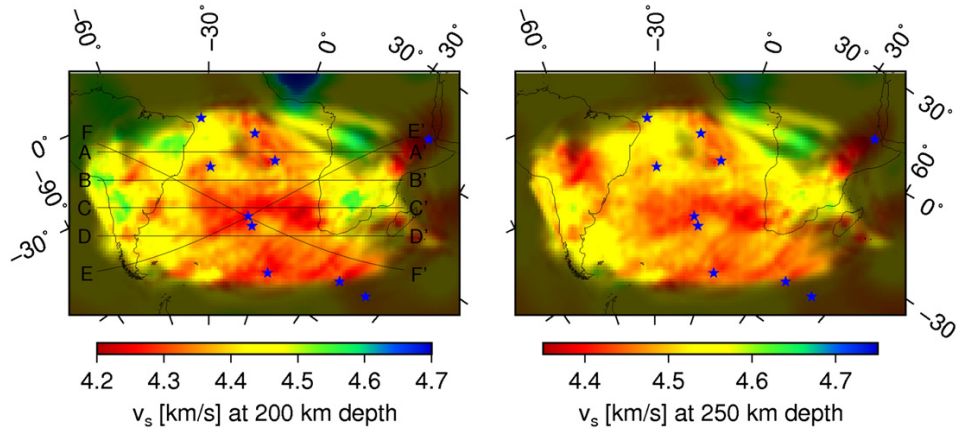


Fig. 7. Horizontal slices through the final tomographic model at 200 km depth (left) and 250 km depth (right). Black lines on the 200 km depth slice indicate the locations for the cross sections shown in Fig. 9. Oblique Mercator projection. The fast anomalies corresponding to continental cratons are less pronounced than at shallower depths, while slow velocities are overall dominant, in particular in the sub-oceanic mantle but protruding also significantly under the continents, winding between the cratons.

Kalahari craton shifts with depth towards the north-east, becoming less pronounced and disappearing completely below 250 km depth. The fast anomaly corresponding to the Congo craton instead is more stable and remains clearly visible even at 250 km and deeper. Below 300 km depth two other prominent slow anomalies are particularly noticeable, one under the Angola basin and the other under the gulf of Guinea extending all the way north under the West African craton.

4.3. South Atlantic Ocean

The seismic anomalies in the oceanic regions at 100 and 150 km depths are mainly correlated with the thermal cooling of the ageing lithosphere: the slowest material is at the mid-oceanic ridge and gets faster towards the continents. Two anomalously slow regions branch out from the Mid-Atlantic ridge heading north-east towards southern Africa and north-west towards Brazil. Interestingly, these anomalies are spatially quite well correlated with the Rio Grande Rise and the Walvis Ridge. The slow anomaly on the African side then bends then southwards all along Namibia and South Africa, connecting with a slow anomaly corresponding to the Cape Rise and the paleo-location of the Mid-Atlantic Ridge off the coast of South Africa at the time of the initial South Atlantic opening.

Below 150 km depth the lithospheric signature disappears and the north–south trending slow anomaly corresponding to the mid-oceanic ridge is replaced by an overall slow mantle streaked with an east–west slow anomaly extending from the Rio Grande Rise to the coast of Namibia. The slow velocity anomaly off the coast of Namibia becomes more pronounced, together with the slow anomaly under Bouvet island and the Atlantic–Antarctica ridge triple junction. The Argentine basin (see profiles E–E') and some parts of the Brazil basin (see profiles A–A') are instead characterized by relatively faster velocities throughout the upper 400 km of the mantle.

4.4. Waveform fit

In Figs. 11–14 we show some examples of the increased waveform fit for some representative source–receiver configurations. During the first iteration we were able to use only a limited number of waveforms: the initial model was too fast under the ocean, and the synthetic waveforms for paths crossing the Atlantic were frequently too out of phase with the observed data, causing phase jumps in the misfit function and making the resulting adjoint source unusable. As the model was getting better, with further iterations, and the synthetics were becoming more similar to the observed data, we were able to exploit more seismograms and

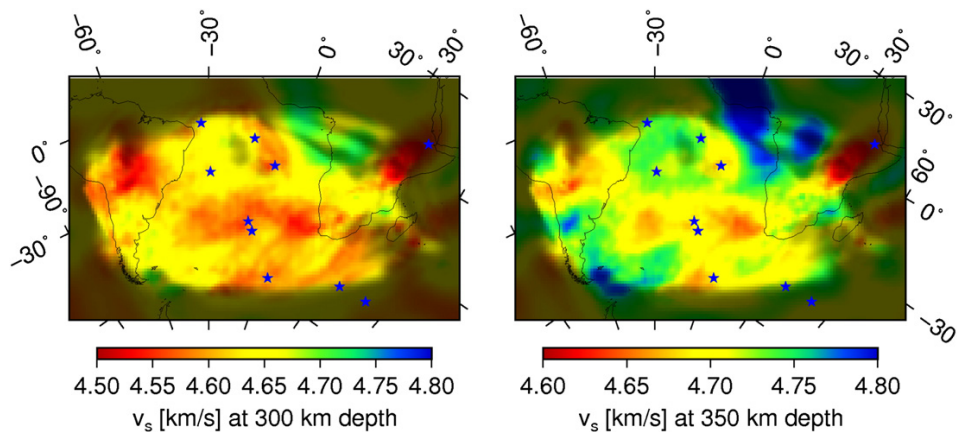


Fig. 8. Horizontal slices through the final tomographic model at 300 km depth (left) and 350 km depth (right). Oblique Mercator projection. At these depths the pattern of slow velocity anomalies starts to change into round shaped slow regions in an overall fast mantle.

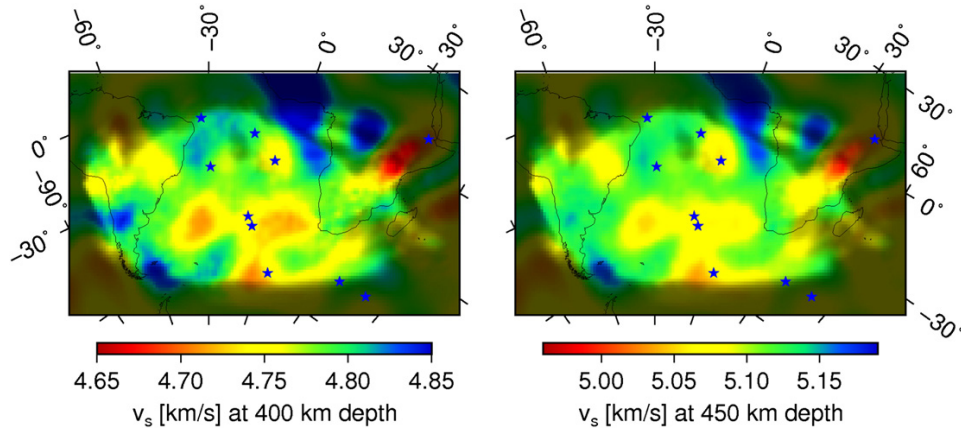


Fig. 9. Horizontal slices through the final tomographic model at 400 km depth (left) and 450 km depth (right). Oblique Mercator projection. Slow velocity anomalies are more rounded and embedded in an overall faster mantle.

to expand the time window, that is the function $W(t,\omega)$ in Eq. (4), to include longer portions of the waveforms. As a result, the total time window length of the fitted portions has increased by a factor of 2, with a 50% misfit reduction over the original time windows.

4.5. Point spread functions

A point spread function (PSF) (Fichtner and Trampert, 2011) represents the sensitivity of a single adjoint iteration to a small localized

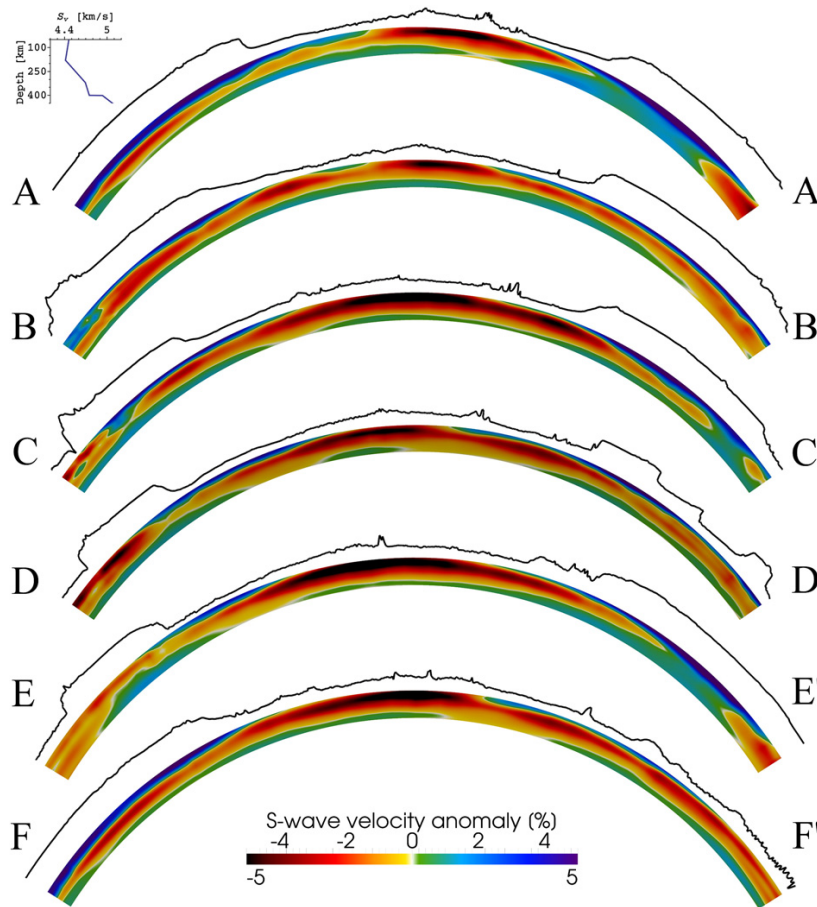


Fig. 10. Vertical profiles through the final tomographic model between 50 and 450 km depth. The upper 50 km have been removed since we are using a long wavelength equivalent crustal model. The thick black line on top of each profile is the (50× exaggerated) surface topography. The locations of the profiles are indicated in Fig. 7. Velocity variations are expressed as percent anomalies with respect to the 1-D S-wave velocity profile shown in the inset in the upper-left corner.

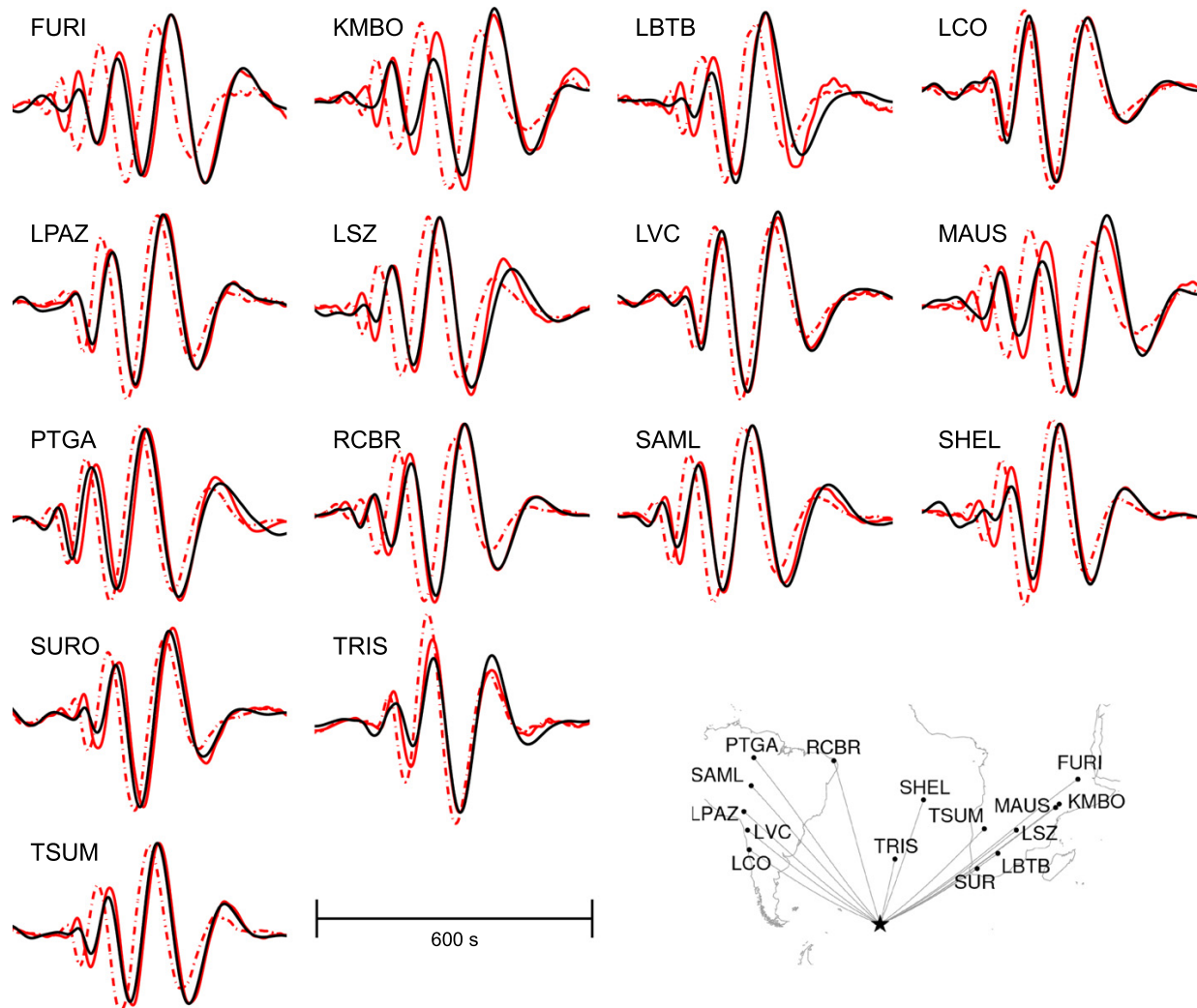


Fig. 11. Waveform comparison. Data are plotted as thick black lines, synthetics calculated with the final model as thick red lines, synthetics calculated with the initial model as dash-dotted red lines. Seismograms for an M_f 6.8 event occurred on January 5th, 2010 east of the South Sandwich islands (58°S , 15°W).

anomaly, and it can thus be used to assess the local resolution of the model and the eventual trade-offs with structures elsewhere in the model. In order to compute a PSF, a small anomaly is added to the current tomographic model and a single adjoint iteration is performed, obtaining the total derivative of the misfit function for this perturbed model. The PSF is then obtained by subtracting the total derivative of the unperturbed model from the total derivative of the perturbed model. Fig. 15 shows the three localized slow velocity anomalies used as input and the resulting PSF. The geometry of each anomaly is reconstructed reasonably well, although there is a consistent trade-off between negative sensitivity at the anomaly and positive sensitivity around it. The sensitivity decreases from 150 km depth to 305 km depth by about a factor of five.

5. Discussion

We have inverted a wide collection of broadband seismograms for isotropic seismic structure in the South Atlantic region. The full solution of the equations of motion for a realistic three dimensional

heterogeneous model through a numerical spectral-element technique ensures that differences between synthetic and recorded seismograms arise only from yet undiscovered Earth structure or errors in source parameters. The advantages of the full waveform method are particularly relevant in strongly heterogeneous portions of the Earth, such as the prominent ocean–continent–transitions of the South Atlantic region.

The number of events used in our inversion was limited by the available computational resources. The comparatively small number of seismograms is in part compensated by extracting as much waveform information as possible, e.g., through the application of the time frequency (TF) misfits. TF misfits as defined by Fichtner et al. (2008) and reviewed in Fichtner et al. (2009) offer several advantages: (1) they separate phase and envelope information, (2) apply to any type of seismic wave, (3) yield a quasi-linear relation to Earth structure and, most importantly, (4) exploit the complete waveform information. However, the phase misfit is meaningful only when observed and synthetic waveforms are sufficiently close to avoid phase jumps. We have picked and weighted the time windows manually to ensure that no phase jumps occur. An alternative

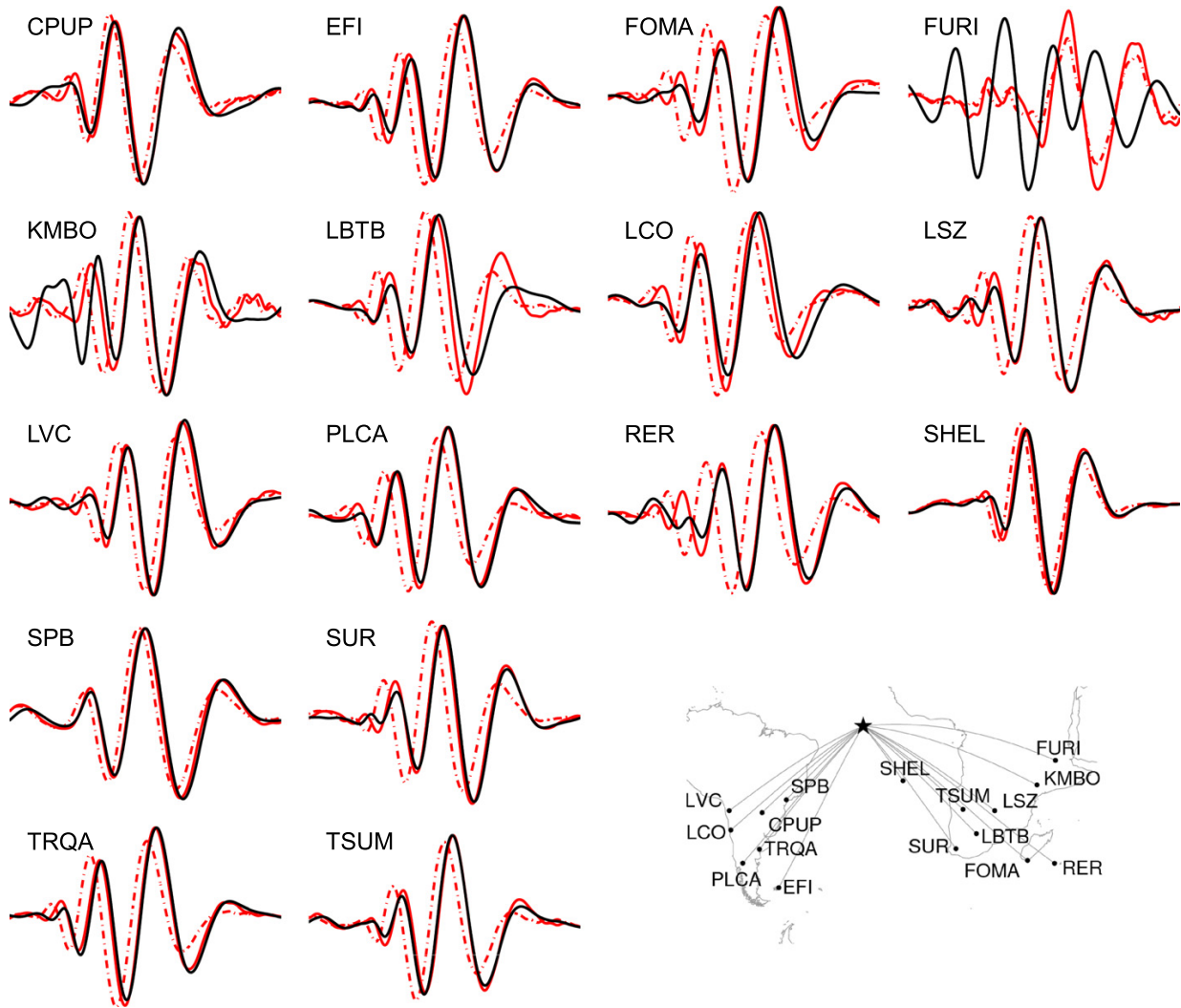


Fig. 12. Waveform comparison. Data are plotted as thick black lines, synthetics calculated with the final model as thick red lines, synthetics calculated with the initial model as dash-dotted red lines. Seismograms for an M_s 6.4 event occurred on December 9th, 2009 at the Central Mid-Atlantic Ridge (1°S , 21°W). Notice the complete difference between the observed and the modelled waveform for station FURI, that prevented the computation of a meaningful misfit and the improvement of the fit. Around 3% of the seismograms are not fitted well.

to manual selection has recently been proposed by Maggi et al. (2009).

An expected result is that the low velocity anomalies mapped in our inversion are spatially more extended and significantly slower than in the starting model, since their influence on wave propagation relative to raypath tomography is more pronounced when finite frequency effects, like waveform healing, are taken into account (Zhou et al., 2005).

The fast anomaly corresponding to the Congo craton is imaged down to great depth (see profiles A–A' and E–E' in Fig. 10). It is likely that amplitude and spatial extent of this feature are overestimated: the paucity of waves crossing the area (see Fig. 5) and the strong difference between synthetic and observed waveforms (see Fig. 12) prevented us from extracting robust structural information for this region, so that the initial model remains uncorrected in the inversion. Neighbouring stations are too few and too distant to build up significant sensitivity in this region. This is true both at shallower depth,

above 150 km, where the sensitivity of surface waves is restricted to a narrower Fresnel zone, and deeper, below 300 km, where increased width of the Fresnel zone is mitigated by lower overall sensitivity of the wavefield. A comparison with other seismic studies of the region (Begg et al., 2009; Reusch et al., 2010; Sebai et al., 2006) shows that the anomaly is probably due to a depthwise smearing towards the ocean of the overlying fast regions. Support for this interpretation comes from the fact that the waveform fit for seismograms crossing two unfavourable, outlying regions – north Central Africa and the Gulf of Guinea – improved only marginally (see e.g., Fig. 12, station FURI).

5.1. Comparison with previous tomographic studies

In the well-resolved parts of our computational domain, our model shows excellent agreement with previous regional tomographic studies for the South American (Feng et al., 2007; Heintz et al., 2005) and the

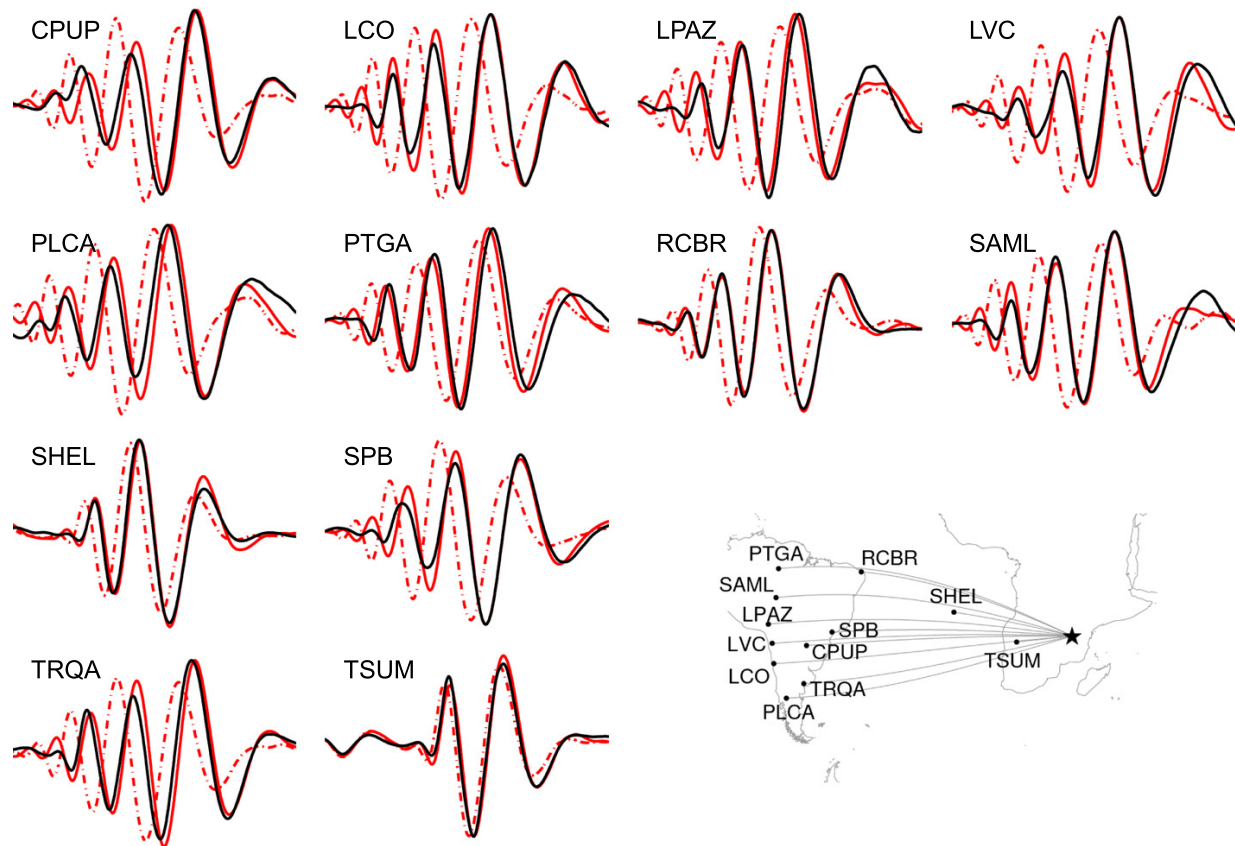


Fig. 13. Waveform comparison. Data are plotted as thick black lines, synthetics calculated with the final model as thick red lines, synthetics calculated with the initial model as dash-dotted red lines. Seismograms for an M_s 5.9 event occurred on December 8th, 2009 in Tanzania (10°S , 34°E).

African region (Begg et al., 2009; Chevrot and Zhao, 2007; Fishwick, 2010; Sebai et al., 2006). Discrepancies at smaller length scales are probably caused by differences in methodology and number and types of seismic waveform used. Since there are no regional studies of the oceanic region, we can compare our model only to global S wave tomography models (Grand et al., 1997; Lekić and Romanowicz, 2011; Masters et al., 1999; Mégnin and Romanowicz, 1999). We find a good agreement with our results in the upper 250 km, while deeper down only the model SEMum by Lekić and Romanowicz (2011) presents features similar to those of our model. In particular, model SAW24B16 by Mégnin and Romanowicz (1999) is characterized by a fast velocity anomaly halfway between South America and Africa at 350 km depth that is absent in our model.

The initial starting model for our iterative inversion is taken from Ritsema's s20rts (Ritsema and van Heijst, 2004) global seismic study, as mentioned before. The same working group recently published a new global tomography model, s40rts (Ritsema et al., 2011). While based on data types and inversion method similar to s20rts, it takes advantage of an extended data set to obtain a higher resolution. There is a good correlation in the upper 250 km, although our model presents broader slow velocity anomalies.

5.2. Geodynamic implications

Since this is a preliminary model obtained using only long period waves the model resolution is low, and the predominance of east-

west trending paths is likely to cause some artefacts in the shape of the anomalies. For this reason we give here a possible interpretation for its broadest and best constrained features only.

The 3-D heterogeneity model for the South Atlantic region is characterized by a strong radial change in the seismic anomaly pattern (see Figs. 6–10): down to 150 km depth the imaged anomalies reflect the continental and oceanic lithospheric structure; between ≈ 150 and ≈ 300 km depth the only lithospheric features are given by the fast anomalies associated with cratonic roots, while the mantle is occupied by seismically slower material assuming horizontally elongated forms; deeper than ≈ 350 km the mantle is characterized by vertically oriented, round-shaped slow anomalies embedded in a faster mantle. This variation in heterogeneity may reflect a depthwise change in the convective planform, with hot buoyant mantle material supplied from a greater depth dominating horizontal upper mantle advection in a narrow channel reminiscent of the asthenosphere. A variety of evidence from seismology (Dziewonski and Anderson, 1981), rock mechanics (Karato and Wu, 1993), the geoid (Hager and Richards, 1989), convective planform studies (Bunge et al., 1996; Busse et al., 2006) and post-glacial rebound (Mitrovica, 1996) strongly argues for the existence of a mechanically weak upper mantle layer. But inherent trade-offs between layer thickness and viscosity reduction make it difficult to constrain the depth extent of such a layer on the ground of geodynamic observations alone (Paulson et al., 2007; Schaber et al., 2009). Although our model doesn't have enough resolution at depth to pinpoint the thickness

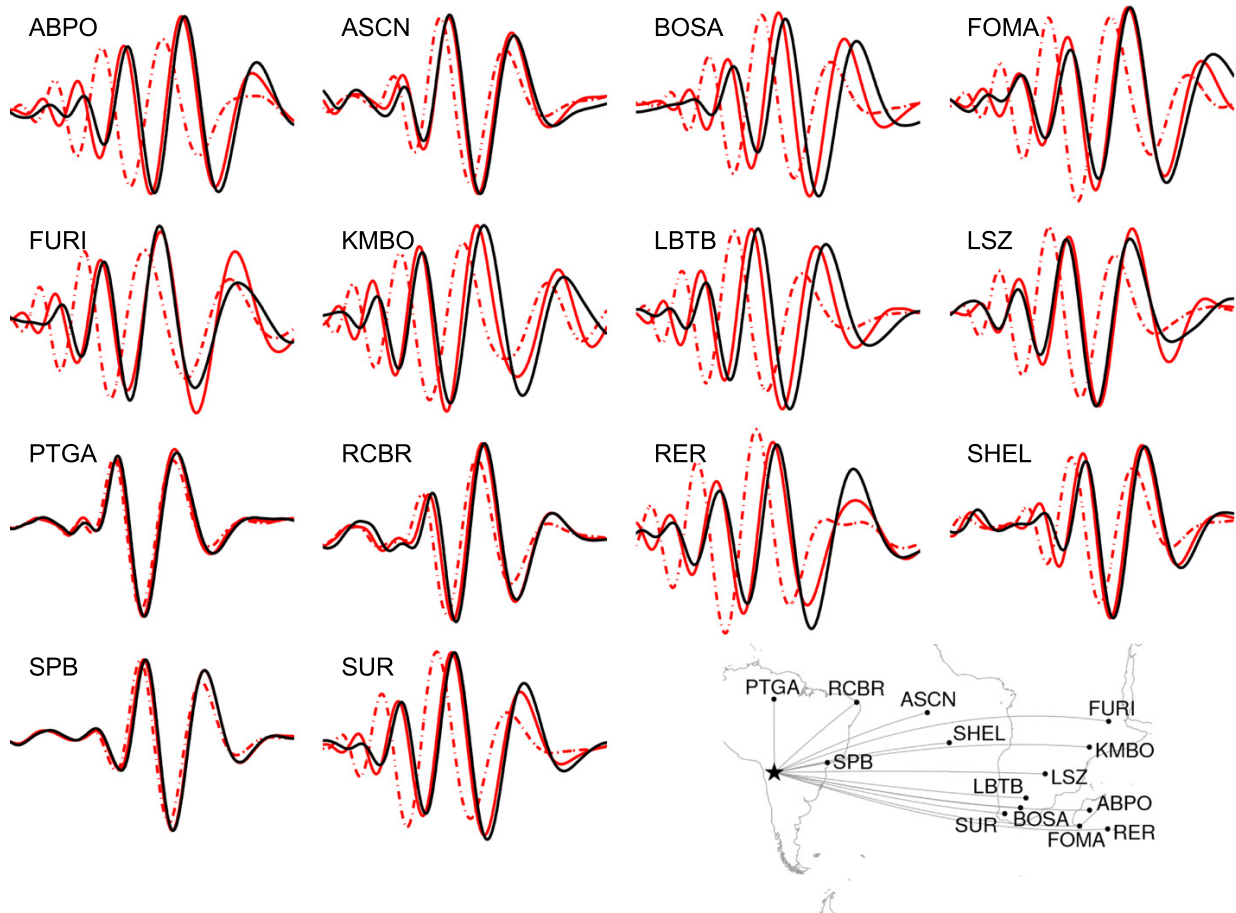


Fig. 14. Waveform comparison. Data are plotted as thick black lines, synthetics calculated with the final model as thick red lines, synthetics calculated with the initial model as dash-dotted red lines. Seismograms for an M_s 6.2 event occurred on November 14th, 2009 in Jujuy, Argentina (23°S , 67°W).

of the layer of low seismic speed nor how sharply it ends, it favours a relatively small (i.e., between 150 and 300 km) rather than a large (i.e., 400 km or more) thickness. Our results are compatible with a limited depth of the asthenosphere for the South Atlantic region.

A thin asthenosphere requires a stronger viscosity reduction with respect to the lower mantle to fit post-glacial rebound data (Mitrovica, 1996). This is bound to have a strong impact on upper mantle dynamics. In particular, it implies a greater mobility for material in the asthenosphere: hot buoyant material rising from the lower mantle can spread horizontally at a much faster rate than the overlying plate, keeping the asthenospheric layer relatively hot and homogeneous, and thus generating the type of seismic structure that we see in our model.

Likely sources of hot buoyant material to supply the South Atlantic upper mantle are a number of primary hotspots in the region (Courtillot et al., 2003). These hotspots are located within an area of elevated topography known as the African superswell (Nyblade and Robinson, 1994). The superswell is characterized by a dynamically supported topography of up to ≈ 1 km, which contrasts sharply with a significant negative dynamic topography of up to ≈ 1 km inferred for the conjugate South American margin (e.g., Winterbourne et al., 2009). The pronounced dynamic topography gradient across

the South Atlantic region implies substantial westward directed channel flow as suggested by Behn et al. (2004) and advocated by Phipps Morgan et al. (1995) from a variety of geodynamic and geochemical considerations. We note that significant basal shear tractions arising from westward fluxing sub-Atlantic asthenosphere would help to balance the budget of driving and resisting forces acting on the South American plate by balancing the gravitational load associated with the Andes (Husson et al., 2012; Iaffaldano and Bunge, 2009).

We assess the dynamical feasibility of westward fluxing asthenosphere across the South Atlantic region from a simple fluid dynamic model for pressure-driven flow in a low viscosity channel, where the asthenosphere channel is approximated as a viscous fluid confined between two fixed, horizontal infinite planes separated by distance h . The excess velocity due to the horizontal pressure gradient $d p/d x$ that arises in the channel varies parabolically with depth (Landau and Lifshitz, 1987) such that the mean fluid velocity is:

$$\bar{v} = -\frac{h^2}{12\eta} \frac{dp}{dx}, \quad (5)$$

where η is the viscosity. An estimate of the pressure gradient across the South Atlantic can be obtained from the oceanic residual topography

18 2. Full waveform tomography of the upper mantle in the South Atlantic

38

L. Colli et al. / Tectonophysics 604 (2013) 26–40

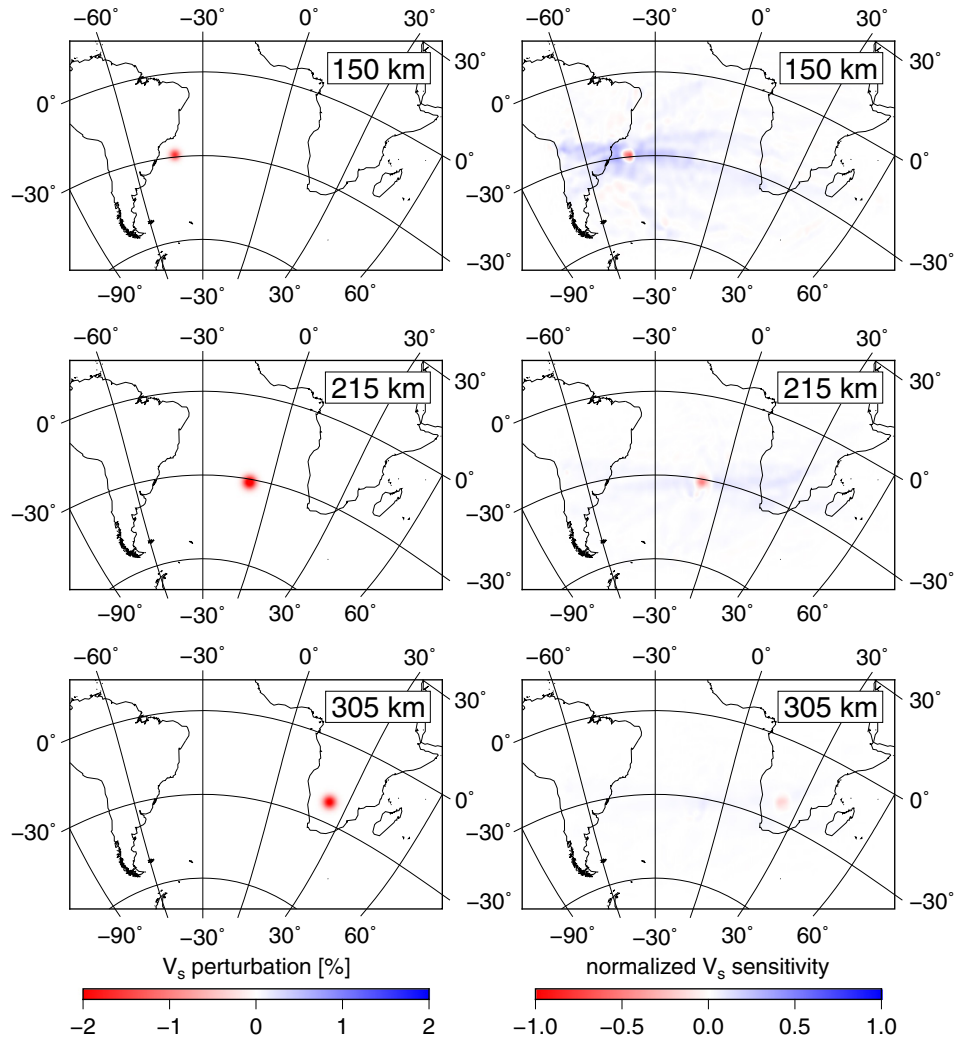


Fig. 15. Horizontal slices showing the input S-wave velocity anomaly (left column) and the computed PSF sensitivity (right column) for three small anomalies localized at 150 km depth off the coast of Brazil (top row), at 215 km depth below Tristan da Cunha (middle row) and at 305 km depth below southern Africa (bottom row).

(Fig. 1) difference of up to ≈ 2 km between the Argentine Basin and that of the Cape Basin, from which we infer a dynamically maintained pressure difference of ≈ 60 MPa over a distance of ≈ 5000 km. This yields a velocity of ≈ 12.5 cm/yr for an asthenosphere of a viscosity of 10^{19} Pa \cdot s and a channel thickness h of 200 km. A thicker layer ($h = 500$ km) would instead be characterized by a higher viscosity ($\eta = 3 \cdot 10^{20}$ Pa \cdot s) and the mean fluid velocity would thus be much smaller (≈ 2.6 cm/yr).

The pressure gradient across the South Atlantic Ocean can thus produce a significant excess velocity in a thin and low-viscosity asthenosphere with respect to both the overlying plate and the underlying mantle. Hot buoyant material rising to the upper mantle under southern Africa can thus spread westward at a fast rate, keeping the asthenosphere relatively homogeneous and considerably warmer than the ambient mantle. This would in turn result in a layer characterized by widespread slow seismic velocities. It is thus possible for the layer of slow seismic velocity imaged by our seismic tomography to be primarily thermal in nature and due to fast horizontal advection of hot material rising from deeper in the mantle.

6. Conclusions

We have successfully obtained a full waveform tomography for isotropic upper-mantle structure of a large and sparsely sampled region. This result has been achieved thanks to an accurate numerical solution of the elastic wave equation for 3-D heterogeneous media, together with a careful choice of the misfit function and the use of the adjoint method. We have thus been able to avoid the artefacts generated by common simplifying approximations and to extract the maximum amount of information from each seismogram, thus compensating for the paucity of data.

The resulting tomographic image shows a broad region in the shallow upper mantle characterized by particularly low velocities that may reflect the dynamics of a thin and very mobile asthenosphere. In order to better assess the spatial extension of this region and its geodynamical significance we plan to extend the frequency window up to 33 mHz (30 s period). This will allow us not only to use seismic waves characterized by a different spatial sensitivity, but also to exploit a larger number of seismograms, thanks to the more favourable signal-to-noise ratio at these higher frequencies.

Acknowledgments

This study is funded by the German Research Foundation (DFG) within the priority program SPP 1375 - SAMPLE. We would like to thank Brian Kennett for many useful discussions and insightful advices.

Appendix A. The adjoint equation

We present here only a brief summary of the theory of the adjoint method applied to seismology; those interested in more details are referred to Fichtner et al. (2006, 2008, 2009).

Let us assume we are confident that the recorded elastic displacement \mathbf{u}^0 can be described as the solution of the wave equation, which we will denote via the shorthand \mathbf{L} , in a model Earth described by the set of parameters \mathbf{p} in the presence of an external forcing \mathbf{g}_0 :

$$\mathbf{L}(\mathbf{u}, \mathbf{p}) = \rho(\mathbf{x}) \partial_t^2 \mathbf{u}(\mathbf{x}, t) - \nabla \cdot \int_{-\infty}^t \mathbf{C}(\mathbf{x}, t - \tau) : \nabla \mathbf{u}(\mathbf{x}, \tau) \, d\tau = \mathbf{g}_0(\mathbf{x}, t). \quad (\text{A.1})$$

The left hand side contains the physics of the system, while the right hand side \mathbf{g}_0 is the particular earthquake that gave rise to that particular seismogram, \mathbf{u}^0 . The model parameters \mathbf{p} comprise the mass density ρ and the elastic parameters contained in the relaxation tensor \mathbf{C} . Solving the inverse problem means to find the particular value of the parameters \mathbf{p}_{\min} for which the solution \mathbf{u}_{\min} of the differential equation is closest to the observable \mathbf{u}^0 .

We start from an initial guess for the model parameters that produce an initial mismatched solution, and we then iteratively correct the model parameters by descending the gradient of the misfit function χ . The adjoint method provides an elegant way of computing the gradient and is particularly efficient when the parameter space is very large. Assuming that the misfit function χ can be expressed as a bilinear form, i.e.,

$$\chi(\mathbf{u}, \mathbf{p}) = \langle \mathbf{1}, f(\mathbf{u}, \mathbf{p}) \rangle, \quad (\text{A.2})$$

we can rewrite Eq. (1) as

$$D_p \chi(\mathbf{u}, \mathbf{p})(\mathbf{d}) = \langle \mathbf{d}, \partial_p f(\mathbf{u}, \mathbf{p}) \rangle + \langle \mathbf{v}, \partial_u f(\mathbf{u}, \mathbf{p}) \rangle, \quad (\text{A.3})$$

where $\mathbf{v} = D_p \mathbf{u}(\mathbf{d})$. Differentiating (A.1) with respect to \mathbf{p} yields

$$D_p \mathbf{L}(\mathbf{u}; \mathbf{p})(\mathbf{d}) = \partial_u \mathbf{L}(\mathbf{u}; \mathbf{p})(\mathbf{v}) + \partial_p \mathbf{L}(\mathbf{u}; \mathbf{p})(\mathbf{d}) = 0, \quad (\text{A.4})$$

since the r.h.s. of Eq. (A.1) doesn't depend on the model parameters. Taking the scalar product with an arbitrary but sufficiently regular test function ψ , we find that

$$\langle \partial_u \mathbf{L}(\mathbf{u}; \mathbf{p})(\mathbf{v}), \psi \rangle + \langle \partial_p \mathbf{L}(\mathbf{u}; \mathbf{p})(\mathbf{d}), \psi \rangle = 0. \quad (\text{A.5})$$

Assuming that there exist two transposed operators $\partial_u \mathbf{L}^*(\mathbf{u}; \mathbf{p})$ and $\partial_p \mathbf{L}^*(\mathbf{u}; \mathbf{p})$ such that

$$\langle \partial_u \mathbf{L}(\mathbf{u}; \mathbf{p})(\mathbf{v}), \psi \rangle = \langle \mathbf{v}, \partial_u \mathbf{L}^*(\mathbf{u}; \mathbf{p})(\psi) \rangle, \quad (\text{A.6})$$

$$\langle \partial_p \mathbf{L}(\mathbf{u}; \mathbf{p})(\mathbf{d}), \psi \rangle = \langle \mathbf{d}, \partial_p \mathbf{L}^*(\mathbf{u}; \mathbf{p})(\psi) \rangle, \quad (\text{A.7})$$

then Eq. (A.5) can be rewritten as

$$\langle \mathbf{v}, \partial_u \mathbf{L}^*(\mathbf{u}; \mathbf{p})(\psi) \rangle + \langle \mathbf{d}, \partial_p \mathbf{L}^*(\mathbf{u}; \mathbf{p})(\psi) \rangle = 0. \quad (\text{A.8})$$

Finding an explicit expression for the transpose operators can be difficult, and may require some conditions on the test function ψ . In case of the wave equation, its adjoint equation is again of the wave

type but reversed in time, and the test function ψ is subject to boundary conditions that are dual with respect to the boundary conditions on \mathbf{u} , and to terminal conditions instead of initial conditions.

Adding together Eqs. (A.3) and (A.8) yields

$$D_p \chi(\mathbf{u}, \mathbf{p})(\mathbf{d}) = \langle \mathbf{d}, \partial_p f(\mathbf{u}, \mathbf{p}) + \partial_p \mathbf{L}^* \mathbf{L}(\mathbf{u}; \mathbf{p})(\psi) \rangle + \langle \mathbf{v}, \partial_u f(\mathbf{u}, \mathbf{p}) + \partial_u \mathbf{L}^*(\mathbf{u}; \mathbf{p})(\psi) \rangle. \quad (\text{A.9})$$

The term $\mathbf{v} = D_p \mathbf{u}(\mathbf{d})$ may now be eliminated by choosing that particular test function ψ that satisfies

$$\partial_u f(\mathbf{u}, \mathbf{p}) + \partial_u \mathbf{L}^*(\mathbf{u}; \mathbf{p})(\psi) = 0, \quad (\text{A.10})$$

which is called the adjoint equation; therefore the total derivative of the objective function with respect to the model parameters takes the form

$$D_p \chi(\mathbf{u}, \mathbf{p})(\mathbf{d}) = \langle \mathbf{d}, \partial_p f(\mathbf{u}, \mathbf{p}) + \partial_p \mathbf{L}^* \mathbf{L}(\mathbf{u}; \mathbf{p})(\psi) \rangle. \quad (\text{A.11})$$

The adjoint method consists thus in obtaining the transpose operators for the physical problem at hand. One then finds a solution of the adjoint problem, that is a solution of the adjoint equation plus the corollary conditions on the test function, and finally calculates the total derivative of the objective function relative to the model parameters.

Appendix B. Supplementary data

Supplementary data to this article can be found online at <http://dx.doi.org/10.1016/j.tecto.2013.06.015>.

References

- Amante, C., Eakins, B.W., 2009. ETOPO1 1 arc-minute global relief model: procedures, data sources and analysis. NOAA Technical Memorandum NESDIS NGDC-24.
- Anderson, D.L., 1982. Hotspots, polar wander, Mesozoic convection and the geoid. *Nature* 297, 391–393.
- Begg, G.C., Griffin, W.L., Natapov, L.M., O'Reilly, S.Y., Grand, S.P., O'Neill, C.J., Hronsky, J.M.A., Djomani, Y.P., Swain, C.J., Deen, T., Bowden, P., 2009. The lithospheric architecture of Africa: seismic tomography, mantle petrology, and tectonic evolution. *Geosphere* 5, 23–50.
- Behn, M.D., Conrad, C.P., Silver, P.G., 2004. Detection of upper mantle flow associated with the African Superplume. *Earth and Planetary Science Letters* 224, 259–274.
- Bunge, H.P., Richards, M.A., Baumgardner, J.R., 1996. Effect of depth-dependent viscosity on the planform of mantle convection. *Nature* 379, 436–438.
- Bunge, H.P., Hagelberg, C.R., Travis, B.J., 2003. Mantle circulation models with variational data assimilation: inferring past mantle flow and structure from plate motion histories and seismic tomography. *Geophysical Journal International* 152, 280–301.
- Burke, K., Gunnell, Y., 2008. The African erosion surface: a continental-scale synthesis of geomorphology, tectonics, and environmental change over the past 180 million years. *Memoir (Geological Society of America)*. Geological Society of America 201, 1–66.
- Busse, F.H., Richards, M.A., Lenardic, A., 2006. A simple model of high Prandtl and high Rayleigh number convection bounded by thin low-viscosity layers. *Geophysical Journal International* 164, 160–167.
- Chen, P., Zhao, L., Jordan, T.H., 2007. Full 3D tomography for the crustal structure of the Los Angeles region. *Bulletin of the Seismological Society of America* 97, 1094–1120.
- Chevrot, S., Zhao, L., 2007. Multiscale finite-frequency Rayleigh wave tomography of the Kaapvaal craton. *Geophysical Journal International* 169, 201–215.
- Courtillot, V., Davaille, A., Besse, J., Stock, J., 2003. Three distinct types of hotspots in the Earth's mantle. *Earth and Planetary Science Letters* 205, 295–308.
- Crosby, A.G., McKenzie, D., Sclater, J.G., 2006. The relationship between depth, age and gravity in the oceans. *Geophysical Journal International* 166, 553–573.
- Debayle, E., Kennett, B., Priestley, K., 2005. Global azimuthal seismic anisotropy and the unique plate-motion deformation of Australia. *Nature* 433, 509–512.
- Dziewonski, A.M., Anderson, D.L., 1981. Preliminary reference Earth model. *Physics of the Earth and Planetary Interiors* 25, 297–356.
- Feng, M., van der Lee, S., Assumpção, M., 2007. Upper mantle structure of South America from joint inversion of waveforms and fundamental mode group velocities of Rayleigh waves. *Journal of Geophysical Research* 112.
- Fichtner, A., Igel, H., 2008. Efficient numerical surface wave propagation through the optimization of discrete crustal models – a technique based on non-linear dispersion curve matching (DCM). *Geophysical Journal International* 173, 519–533.
- Fichtner, A., Trampert, J., 2011. Resolution analysis in full waveform inversion. *Geophysical Journal International* 187, 1604–1624.

20 2. Full waveform tomography of the upper mantle in the South Atlantic

40

L. Colli et al. / *Tectonophysics* 604 (2013) 26–40

- Fichtner, A., Bunge, H.P., Igel, H., 2006. The adjoint method in seismology I. Theory. *Physics of the Earth and Planetary Interiors* 157, 86–104.
- Fichtner, A., Kennett, B.L.N., Igel, H., Bunge, H.P., 2008. Theoretical background for continental- and global-scale full-waveform inversion in the time–frequency domain. *Geophysical Journal International* 175, 665–685.
- Fichtner, A., Kennett, B.L.N., Igel, H., Bunge, H.P., 2009. Full seismic waveform tomography for upper-mantle structure in the australasian region using adjoint methods. *Geophysical Journal International* 179, 1703–1725.
- Fishwick, S., 2010. Surface wave tomography: Imaging of the lithosphere–asthenosphere boundary beneath central and southern Africa? *Lithos* 120, 63–73.
- Forte, A.M., Quéré, S., Moucha, R., Simmons, N.A., Grand, S.P., Mitrovica, J.X., Rowley, D.B., 2010. Joint seismic–geodynamic–mineral physical modelling of African geodynamics: a reconciliation of deep-mantle convection with surface geophysical constraints. *Earth and Planetary Science Letters* 295, 329–341.
- Fournier, A., Hulot, G., Jault, D., Kuang, W., Tangborn, A., Gillet, N., Canet, E., Aubert, J., Lhuillier, F., 2010. An introduction to data assimilation and predictability in geomagnetism. *Space Science Reviews* 155, 247–291.
- Freybourger, M., Gaherty, J.B., Jordan, T.H., Kaapvaal Seismic Grp., 2001. Structure of the Kaapvaal craton from surface waves. *Geophysical Research Letters* 28, 2489–2492.
- Grand, S.P., 2002. Mantle shear-wave tomography and the fate of subducted slabs. *Philosophical Transactions of the Royal Society A* 360, 2475–2491.
- Grand, S.P., van der Hilst, R.D., Widiyantoro, S., 1997. Global seismic tomography: a snapshot of convection in the earth. *GSA Today* 7, 1–7.
- Gurnis, M., Mitrovica, J.X., Ritsema, J., van Heijst, H.J., 2000. Constraining mantle density structure using geological evidence of surface uplift rates: the case of the African superplume. *Geochemistry, Geophysics, Geosystems* 1.
- Hager, B.H., Richards, M.A., 1989. Long-wavelength variations in Earth's geoid: physical models and dynamical implications. *Philosophical Transactions of the Royal Society A* 328, 309–327.
- Heintz, M., Debayle, E., Vauchez, A., 2005. Upper mantle structure of the South American continent and neighboring oceans from surface wave tomography. *Tectonophysics* 406, 115–139.
- Husson, L., Conrad, C.P., Faccenna, C., 2012. Plate motions, Andean orogeny, and volcanism above the South Atlantic convection cell. *Earth and Planetary Science Letters* 317–318, 126–135.
- Iaffaldano, G., Bunge, H.P., 2009. Relating rapid plate-motion variations to plate-boundary forces in global coupled models of the mantle/lithosphere system: effects of topography and friction. *Tectonophysics* 474, 393–404.
- Iaffaldano, G., Bunge, H.P., Bucker, M., 2007. Mountain belt growth inferred from histories of past plate convergence: a new tectonic inverse problem. *Earth and Planetary Science Letters* 260, 516–523.
- Karato, S.I., Wu, P., 1993. Rheology of the upper mantle: a synthesis. *Science* 260, 771–778.
- Landau, L.D., Lifshitz, E.M., 1987. *Fluid Mechanics*, Second edition. *Course of Theoretical Physics*, 6. Butterworth-Heinemann.
- Lekić, V., Romanowicz, B., 2011. Inferring upper-mantle structure by full waveform tomography with the spectral element method. *Geophysical Journal International* 185, 799–831.
- Lithgow-Bertelloni, C., Silver, P.G., 1998. Dynamic topography, plate driving forces and the African superswell. *Nature* 395, 269–272.
- Maggi, A., Tape, C., Chen, M., Chao, D., Tromp, J., 2009. An automated time-window selection algorithm for seismic tomography. *Geophysical Journal International* 178, 257–281.
- Masters, G., Bolton, H., Laske, G., 1999. Joint seismic tomography for p and s velocities: how pervasive are chemical anomalies in the mantle? *Eos, Transactions, American Geophysical Union* 80.
- Mégnin, C., Romanowicz, B., 1999. The effects of the theoretical formalism and data selection on mantle models derived from waveform tomography. *Geophysical Journal International* 138, 366–380.
- Meier, U., Curtis, A., Trampert, J., 2007. Fully nonlinear inversion of fundamental mode surface waves for a global crustal model. *Geophysical Research Letters* 34.
- Mitrovica, J.X., 1996. Haskell [1935] revisited. *Journal of Geophysical Research* 101, 555–569.
- Moucha, R., Forte, A.M., 2011. Changes in African topography driven by mantle convection. *Nature Geoscience* 4, 707–712.
- Müller, R.D., Sdrolias, M., Gaina, C., Roest, W.R., 2008. Age, spreading rates, and spreading asymmetry of the world's ocean crust. *Geochemistry, Geophysics, Geosystems* 9.
- Nyblade, A.A., Robinson, S.W., 1994. The African superswell. *Geophysical Research Letters* 21, 765–768.
- Oeser, J., Bunge, H.P., Mohr, M., 2006. Cluster design in the Earth sciences: TETHYS. In: Gerndt, M., Kranzlmüller, D. (Eds.), *High Performance Computing and Communications – Second International Conference, HPCC 2006*. Springer, Munich, Germany, pp. 31–40.
- Pasyanos, M.E., Nyblade, A.A., 2007. A top to bottom lithospheric study of Africa and Arabia. *Tectonophysics* 444, 27–44.
- Paulson, A., Zhong, S., Wahr, J., 2007. Limitations on the inversion for mantle viscosity from postglacial rebound. *Geophysical Journal International* 168, 1195–1209.
- Phipps Morgan, J., Morgan, W.J., Zhang, Y.S., Smith, W.H.F., 1995. Observational hints for a plume-fed, suboceanic asthenosphere and its role in mantle convection. *Journal of Geophysical Research* 100, 12753–12767.
- Priestley, K., McKenzie, D., Debayle, E., 2006. The state of the upper mantle beneath southern Africa. *Tectonophysics* 416, 101–112.
- Priestley, K., McKenzie, D., Debayle, E., Pilidou, S., 2008. The African upper mantle and its relationship to tectonics and surface geology. *Geophysical Journal International* 175, 1108–1126.
- Reusch, A.M., Nyblade, A.A., Wiens, D.A., Shore, P.J., Ateba, B., Tabod, C.T., Nnange, J.M., 2010. Upper mantle structure beneath Cameroon from body wave tomography and the origin of the Cameroon volcanic line. *Geochemistry, Geophysics, Geosystems* 11.
- Ritsema, J., van Heijst, H.J., 2000. New seismic model of the upper mantle beneath Africa. *Geology* 28, 63–66.
- Ritsema, J., van Heijst, H.J., 2004. Global transition zone tomography. *Journal of Geophysical Research* 109.
- Ritsema, J., van Heijst, H.J., Woodhouse, J.H., 1999. Complex shear wave velocity structure imaged beneath Africa and Iceland. *Science* 286, 1925–1928.
- Ritsema, J., Deuss, A., van Heijst, H.J., Woodhouse, J.H., 2011. S40RTS: a degree–40 shear-velocity model for the mantle from new Rayleigh wave dispersion, teleseismic traveltimes and normal-mode splitting function measurements. *Geophysical Journal International* 3, 1223–1236.
- Schaber, K., Bunge, H.P., Schuberth, B., Malservisi, R., Horbach, A., 2009. Stability of the rotation axis in high-resolution mantle circulation models: weak polar wander despite strong core heating. *Geochemistry, Geophysics, Geosystems* 10.
- Schuberth, B.S.A., Bunge, H.P., Ritsema, J., 2009a. Tomographic filtering of high-resolution mantle circulation models: can seismic heterogeneity be explained by temperature alone? *Geochemistry, Geophysics, Geosystems* 10.
- Schuberth, B.S.A., Bunge, H.P., Steinle-Neumann, G., Moder, C., Oeser, J., 2009b. Thermal versus elastic heterogeneity in high-resolution mantle circulation models with pyrolytic composition: high plume excess temperatures in the lowermost mantle. *Geochemistry, Geophysics, Geosystems* 10.
- Sebai, A., Stutzmann, E., Montagner, J.P., Sicilia, D., Beucler, E., 2006. Anisotropic structure of the African upper mantle from Rayleigh and Love wave tomography. *Physics of the Earth and Planetary Interiors* 155, 48–62.
- Simmons, N.A., Forte, A.M., Grand, S.P., 2007. Thermochemical structure and dynamics of the African superplume. *Geophysical Research Letters* 34.
- Tape, C., Liu, Q., Maggi, A., Tromp, J., 2009. Adjoint tomography of the Southern California crust. *Science* 325, 988–992.
- Tarantola, A., 1988. Theoretical background for the inversion of seismic waveforms, including elasticity and attenuation. *Pure and Applied Geophysics* 128, 365–399.
- Teixeira, F.L., Chew, W.C., 1997. Systematic derivation of anisotropic PML absorbing media in cylindrical and spherical coordinates. *IEEE Microwave and Guided Wave Letters* 7, 371–373.
- Tromp, J., Tape, C., Liu, Q., 2005. Seismic tomography, adjoint methods, time reversal and banana doughnut kernels. *Geophysical Journal International* 160, 195–216.
- Winterbourne, J., Crosby, A., White, N., 2009. Depth, age and dynamic topography of oceanic lithosphere beneath heavily sedimented Atlantic margins. *Earth and Planetary Science Letters* 287, 137–151.
- Zheng, Y., Huang, X., 1997. Anisotropic perfectly matched layers for elastic waves in Cartesian and curvilinear coordinates. Consortium Report.MIT Earth Resources Laboratory.
- Zhou, Y., Dahlen, F.A., Nolet, G., Laske, G., 2005. Finite-frequency effects in global surface-wave tomography. *Geophysical Journal International* 163, 1087–1111.

Chapter 3

Rapid South Atlantic spreading changes and coeval vertical motion in surrounding continents: Evidence for temporal changes of pressure-driven upper mantle flow

This chapter was published in the Journal “Tectonics” in 2014. It describes and discusses how a number of features of the South Atlantic region and of its recent tectonic history can be linked by assuming a thin and low-viscosity asthenosphere.



Tectonics

RESEARCH ARTICLE

10.1002/2014TC003612

Key Points:

- The South Atlantic shows fast spreading rate changes
- They can be explained by temporal changes of pressure-driven asthenospheric flux
- This implies a correlation of horizontal and vertical motions

Correspondence to:

L. Colli,
lorenzo.colli@geophysik.uni-muenchen.de

Citation:

Colli, L., I. Stotz, H.-P. Bunge, M. Smethurst, S. Clark, G. Iaffaldano, A. Tassara, F. Guillocheau, and M. C. Bianchi (2014), Rapid South Atlantic spreading changes and coeval vertical motion in surrounding continents: Evidence for temporal changes of pressure-driven upper mantle flow, *Tectonics*, 32, 1304–1321, doi:10.1002/2014TC003612.

Received 17 APR 2014

Accepted 9 JUN 2014

Accepted article online 18 JUN 2014

Published online 8 JUL 2014

Rapid South Atlantic spreading changes and coeval vertical motion in surrounding continents: Evidence for temporal changes of pressure-driven upper mantle flow

L. Colli¹, I. Stotz^{1,2,3}, H.-P. Bunge¹, M. Smethurst^{4,5}, S. Clark⁵, G. Iaffaldano³, A. Tassara², F. Guillocheau⁶, and M. C. Bianchi¹

¹Department of Earth and Environmental Sciences, Ludwig Maximilian University, Munich, Germany, ²Department of Earth Sciences, Universidad de Concepción, Concepción, Chile, ³Research School of Earth Sciences, Australian National University, Canberra, ACT, Australia, ⁴Avalonia Geophysics, University of Exeter, Exeter, UK, ⁵Computational Geoscience Department, Simula Research Laboratory, Fornebu, Norway, ⁶UMR CNRS 6118 Géosciences Rennes, Université de Rennes 1, Rennes, France

Abstract The South Atlantic region displays (1) a topographic gradient across the basin, with Africa elevated relative to South America, (2) a bimodal spreading history with fast spreading rates in Late Cretaceous and Eo-Oligocene, and (3) episodic regional uplift events in the adjacent continents concentrated in Late Cretaceous and Oligocene. Here we show that these observations can be linked by dynamic processes within Earth's mantle, through temporal changes in asthenosphere flow beneath the region. The topographic gradient implies westward, pressure-driven mantle flow beneath the basin, while the rapid spreading rate changes, on order 10 million years, require significant decoupling of regional plate motion from the large-scale mantle buoyancy distribution through a mechanically weak asthenosphere. Andean topographic growth in late Miocene can explain the most recent South Atlantic spreading velocity reduction, arising from increased plate boundary forcing associated with the newly elevated topography. But this mechanism is unlikely to explain the Late Cretaceous/Tertiary spreading variations, as changes in Andean paleoelevation at the time are small. We propose an unsteady pressure-driven flow component in the asthenosphere beneath the South Atlantic region to explain the Late Cretaceous/Tertiary spreading rate variations. Temporal changes in mantle flow due to temporal changes in regional mantle pressure gradients imply a correlation of horizontal and vertical motions: we find that this prediction from our models agrees with geologic and geophysical observations of the South Atlantic region, including episodes of passive margin uplift, regional basin reactivation, and magmatic activity.

1. Introduction

The South Atlantic holds a prominent place in the history of plate tectonics since *Bullard et al.*'s [1965] fit of South America and Africa showed how both continents were once joined. The region preserves an exceptional archive of past plate motion (Figure 1a) so its spreading history is well known [*Cande et al.*, 1988; *Nürnberg and Müller*, 1991].

Figure 1b shows spreading half rates of the South Atlantic by *Müller et al.* [2008] based on marine magnetic anomaly identifications, following the techniques outlined by *Müller et al.* [1997]. The compilation reveals rapid changes over periods of a few million years (Myr). While it is accepted that buoyancy forces associated with subduction of cold, dense lithosphere provide significant driving forces for plate motion [*Lithgow-Bertelloni and Richards*, 1995], the short duration of the South Atlantic spreading rate changes makes it difficult to attribute them to variations of the large-scale mantle buoyancy distribution, which should evolve on longer timescales on the order of 50 to 100 Myr as suggested by mantle circulation modeling [*Bunge et al.*, 1998].

Some South Atlantic spreading rate changes likely reflect temporal variations in plate boundary forcing, in particular along the western margin of South America. The most significant tectonic change there over the past 25 Myr is the growth of the high Andes, especially the rise of the Altiplano and Puna Plateaus some 10 Myr ago [*Charrier*, 2007; *Garzione et al.*, 2006; *Oncken et al.*, 2006]. Estimated tectonic forces associated with the current Andean topography amount to $\approx 8 \times 10^{12}$ N/m on average, comparable to the driving forces

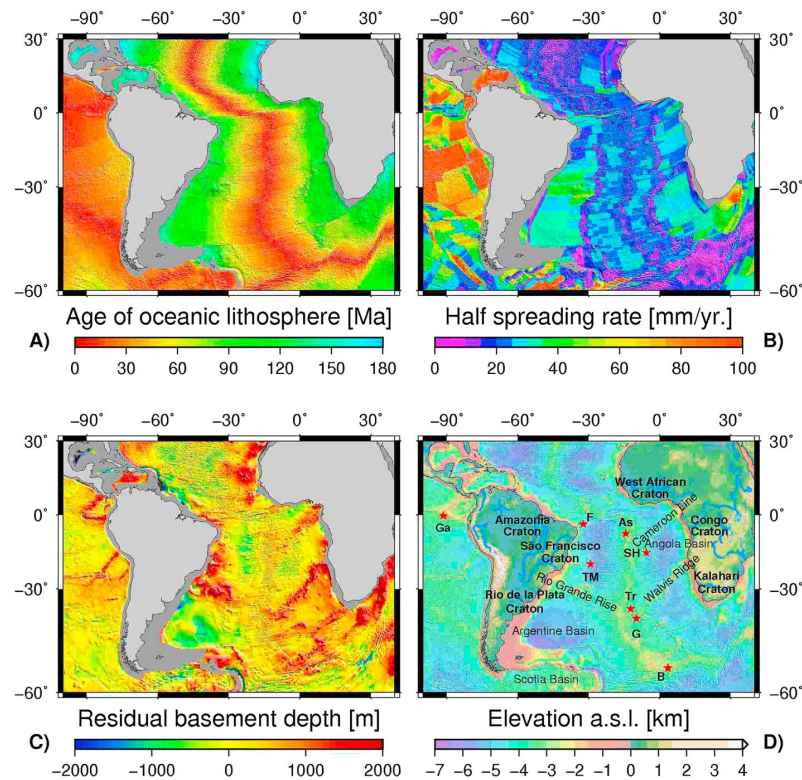


Figure 1. (a) Age-area distribution and (b) half-spreading rates of ocean floor in the South Atlantic region from Müller *et al.* [2008]. (c) Residual basement depth computed by calculating difference between predicted and sediment unloaded basement depth. Predicted basement depth obtained by applying Crosby *et al.*'s [2006] North Pacific thermal boundary layer model to age-area distribution from Müller *et al.* [2008]. (d) Topographic map of the South Atlantic region from the global relief model ETOPO1 [Amante and Eakins, 2009], annotated with major structural elements. Craton names are boldface, while stars denote prominent hot spots (Ga: Galapagos; F: Fernando de Noronha; As: Ascension; SH: Saint Helena; TM: Trindade and Martim Vaz; Tr: Tristan da Cunha; G: Gough Island; and B: Bouvet Island).

in plate tectonics [Husson and Ricard, 2004; Iaffaldano *et al.*, 2006]. The temporal correlation between recent Andean uplift and plate kinematic changes around South America supports the notion that the load of this newly elevated topography affects plate motions. For instance, the 30% convergence reduction across the Nazca/South America margin in the late Miocene, commonly attributed to growth of the high Andes [e.g., Norabuena *et al.*, 1999], has been linked to a corresponding reduction of South Atlantic spreading rates in a global model of the coupled mantle/lithosphere system [Iaffaldano and Bunge, 2009]. Far-field effects are thus an important influence on South Atlantic spreading. Husson *et al.* [2012], moreover, attributed the most recent South Atlantic spreading rate reduction to the formation of an optimal aspect ratio mantle circulation cell beneath the South Atlantic.

The South Atlantic is also an area of anomalous topography [Winterbourne *et al.*, 2009] with a pronounced bathymetric asymmetry (Figure 1c). The mantle beneath Africa has long been shielded from subduction by the former supercontinent Pangea [Anderson, 1982] and harbors a major low seismic velocity body near the base of the mantle [e.g., Grand, 2002; Ritsema *et al.*, 2011; Romanowicz and Gung, 2002; Simmons *et al.*, 2007]. Much of the low seismic velocity is due to elevated temperature [Davies *et al.*, 2012; Schubert *et al.*, 2012, 2009a, 2009b]. Thermal upwellings may thus play a prominent role in the South Atlantic, consistent with observations of numerous plume-related volcanic centers (Figure 1d), elevated heat flow in the mobile belts of Southern Africa [Nyblade and Robinson, 1994], and inferences that Africa experienced greater uplift than other continents in the Tertiary [e.g., Bond, 1978; Burke and Gunnell, 2008]. This view is supported by geodynamic studies suggesting that active thermal upwellings in the mantle general circulation account

for as much as 30% (10 TW) of the mantle heat loss [e.g., Bunge *et al.*, 2001; Bunge, 2005; Labrosse, 2002; Mittelstaedt and Tackley, 2006; Zhong and Leng, 2006].

Rapid spreading rate changes imply some decoupling of plate motion from the large-scale mantle buoyancy distribution, as noted before, presumably through a mechanically weak asthenosphere [Barrell, 1914]. An asthenosphere was advocated early on in the history of plate tectonics to lubricate plate motion [Chase, 1979] and is supported by rock mechanics arguments [Karato and Wu, 1993; Weertman and Weertman, 1975]. Evidence for an asthenosphere comes from various observations, including global [e.g., Richards and Hager, 1984] and regional [Harig *et al.*, 2010] geoid studies, glacial rebound [e.g., Mitrovica, 1996], oceanic intraplate seismicity [Wiens and Stein, 1985], ocean ridge bathymetry [Buck *et al.*, 2009], seismic anisotropy [e.g., Debayle *et al.*, 2005], and electromagnetic sounding [e.g., Jones, 1982]. Low mechanical strength could arise from weakening associated with partial melt [e.g., Anderson and Sammis, 1970] and/or water [e.g., Karato and Jung, 1998]. A consequence would include the concentration of upper mantle flow into a thin channel of greatly enhanced material mobility. Fluid dynamic studies based on numerical and analytic models [e.g., Bunge *et al.*, 1996; Busse *et al.*, 2006; Tackley, 1996] indicate that high material mobility in the asthenosphere is essential to promote the long-wavelength pattern of mantle flow observed on Earth.

Phipps Morgan and Smith [1992] and Phipps Morgan *et al.* [1995] argued that a plume-fed asthenosphere explains various observations related to ocean bathymetry, heat flow, and mantle geochemistry. A series of papers by Höink and Lenardic [2008, 2010] and Höink *et al.* [2011] support the idea that flow in the asthenosphere is caused by lateral pressure gradients (Poiseuille flow) and that the resulting basal shear is the predominant force driving South Atlantic plate motion [Höink *et al.*, 2011]. The concept of asthenosphere flow driven by high- and low-pressure regions relates temporal changes in horizontal motion, i.e., spreading rate changes driven by evolving basal shear forces, explicitly to nonisostatic vertical motion. The latter, known as dynamic topography (see Braun [2010] for a review), can be tested with independent data. For instance, Japsen *et al.* [2012a, and references therein] recently drew attention to episodic burial and exhumation of passive continental margins. Such events are well documented along the Brazilian coast [Cogne *et al.*, 2011; Japsen *et al.*, 2012b] and presumably reflect temporal changes in regional dynamic topography.

The focus of this paper is linking horizontal and vertical motion in the South Atlantic region explicitly by evolving upper mantle flow. First, we review the regional tectonics in terms of spreading history, topographic evolution of the Andes, and upper mantle structure constrained from a new tomographic study. We then use simple torque balance models of the South American plate to separate the influence of basal shear forces from plate boundary forces. We demonstrate that the rapid spreading reduction between 80 and 60 Myr followed by renewed and vigorous spreading after 45 Myr is unlikely to result from plate boundary forcing associated with the Andes, as topography along South America's western margin is low at the time. We then turn our attention to Poiseuille flow and show that the current basin-wide dynamic topography gradient may reflect significant pressure-induced upper mantle flow across the South Atlantic region. The magnitude of the Poiseuille flow velocities is comparable to those suggested from basal shear. We test the hypothesis of time-evolving upper mantle flow caused by time-evolving pressure gradients with geologic observations and find that fast spreading periods in the Late Cretaceous and Eocene coincide with regional topographic uplift events in the African and South American continents. We conclude with considerations on rheology and the general style of mantle convection.

2. Tectonic Setting in the South Atlantic Region

2.1. South Atlantic Spreading History

A number of plate motion models are available for the South Atlantic. We compare six models: Earthbyte [Müller *et al.*, 2008], UTIG [Coffin *et al.*, 1998], NGU [Labails *et al.*, 2009; Torsvik *et al.*, 2009], Moulin [Moulin *et al.*, 2010], and two commercial models, A and B. The models differ in the positions of Euler poles, angular velocities, and the locations of plate boundaries, reflecting different interpretations of paleomagnetic and geologic data. Because each model applies its own geologic timescale, we make the models comparable by using a single timescale: Channell *et al.* [1995] from the opening of the M0 anomaly, and Gradstein *et al.* [2004] from M0 to the present. Taking a point presently located in the Salado subplate of South America (57.2°W, 36°S), we calculate the total spreading rate (with respect to Africa) of each of these models. The resulting rates are reported in Figure 2 from 150 Myr to the present.

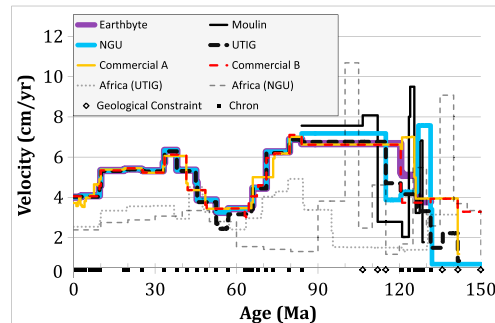


Figure 2. South Atlantic spreading rate for different plate reconstruction models from 150 Myr to the present for a point currently located at 57.2°W, 36°S in a reference frame that keeps Africa fixed. Chrons (squares) and geological constraints dated by particular boundaries (diamonds) used by one or more of the models are shown along the horizontal axis. All models record a spreading rate minimum at around 60 Myr. The curves Africa (NGU) and Africa (UTIG) show the absolute velocities of Africa in a mantle reference frame for an approximately conjugate point in the Orange Basin, at 15°E, 27.5°S.

The curves are similar from C34 (84 Myr) to the present because the rotations are based on similar models. The NGU, Earthbyte, and UTIG models are based on Müller *et al.*'s [1999] reconstruction; Commercial B is based on Cande *et al.* [1988]; and Commercial A is based on a combination of Cande *et al.* [1988] from C4A (8.8 Myr) until the present and Shaw and Cande [1990] from C34 (84 Myr) until C4A. In the early rifting the models vary, although a number of them use Nürnberg and Müller [1991] for the M4 (124.5 Myr) and the M0 (120.6 Myr) anomalies. All models reveal a similar spreading history after around 100 Myr, with a pronounced minimum at the Cretaceous/Tertiary boundary. Spreading is fastest in the Late Cretaceous, drops by a factor of 2 from around 6 to 3 cm/yr between 80 and 70 Myr, stays constant for 10–20 million years before rising back

to almost 6 cm/yr in the middle Eocene, only to decrease again to the current value of about 3.5 cm/yr. Because these rates are reconstructed over intervals of at least 5 Myr, we are confident that the bias of finite-rotation noise [e.g., Iaffaldano *et al.*, 2012] arising from the challenge of precisely identifying the magnetization pattern of the ocean floor and the uncertainty on the geomagnetic polarity timescale is negligible in these models.

It has been proposed [e.g., Silver *et al.*, 1998] that the South Atlantic spreading changes reflect motion of Africa in a mantle reference frame. Thus, Figure 2 also shows the reconstructed absolute motion of Africa according to two different models. The Africa (NGU) curve combines O'Neill *et al.*'s [2005] moving hot spot frame for 100 Myr and younger with Steinberger and Torsvik's [2008] true polar wander frame between 100 Myr and 150 Myr. The Africa (UTIG) curve is based on the fixed hot spot frame of Duncan and Richards [1991] until the middle of their C13–C6 stage (28.5 Myr) and then Müller *et al.*'s [1993] fixed hot spot frame until 130 Myr. While some part of the South Atlantic spreading changes may be ascribed to African absolute motion from C34 to C25 (84 Myr to 56.7 Myr) in the Africa (UTIG) curve, neither the bulk of the spreading variations cannot be explained this way nor can the magnitude of the changes. The spreading rate changes must arise from other forces.

2.2. Topographic Evolution of the Andes

Gansser [1973] divided the Andean chain into a Northern (~12°N to ~5°S), Central (~5°S to ~37°S), and Southern unit (~37°S to ~55°S). The Central unit is characterized by the Altiplano and Puna Plateaus, a magmatic arc (e.g., Western Cordillera) to the west, and a tectonically shortened Eastern Cordillera and foreland to the east [Sempere *et al.*, 2008]. Most models of the orogenic history of the Andes have three main phases [Steinmann *et al.*, 1929]: Peruvian during Late Cretaceous, Incaic in middle Eocene (or Oligocene, according to Sempere *et al.* [1990]), and Quechua since late Miocene. The Northern Central Andes were probably tectonically active during Late Cretaceous [Jaillard, 1994; Sempere *et al.*, 1997]. In latest Cretaceous and early Paleocene, a time also referred to as the KT Orogeny [Charrier, 2007], tectonic activity also took place in the Central Orocline [Charrier, 2007; Cornejo, 2003; Mpodozis *et al.*, 2005] and South Central Andes [Orts and Ramos, 2006; Sempere *et al.*, 1994]. Although no clear evidence exists for Andean paleoelevation in latest Cretaceous and early Paleocene, the scarcity of compressional structures and the small amounts of estimated crustal shortening indicate that elevation presumably was low.

Most studies agree that prominent uplift of the mountain chain started in middle Eocene, reaching a peak in the Oligocene, with a second uplift period in late Miocene [Sempere *et al.*, 1990, 2008]. Middle Eocene and early Oligocene exhumation occurs in the Central Andes [Barnes *et al.*, 2006; Ege *et al.*, 2007; Gillis *et al.*, 2006] with coactivity in the North Central Andes [Hoorn *et al.*, 2010; Jaillard and Soler, 1996; Sebrier *et al.*,

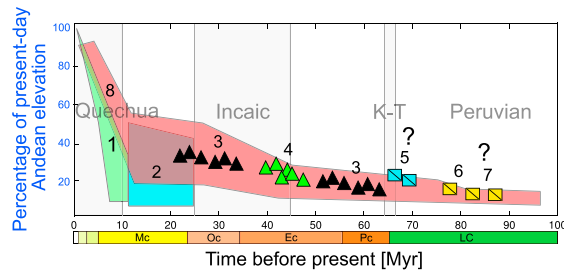


Figure 3. Inferred Andean topographic evolution since Late Cretaceous, plotted relative to today, from a variety of proxies: (1) oxygen isotopes [Garzzone *et al.*, 2006; Ghosh *et al.*, 2006], (2) leaf morphology [Gregory-Wodzicki, 2000], (3) apatite fission track (AFT) in the North Central Andes and Central Orocline [Hoorn *et al.*, 2010], (4) AFT in the Central Orocline [Gillis *et al.*, 2006], (5) unconformities in the Central Orocline [Cornejo, 2003], (6) tectonic activity related to uplift in the Central Orocline [Sempere *et al.*, 1997], and (7) tectonic activity related to uplift in the Northern Central Andes [Jaillard, 1994]. Pink region encompasses the average elevation and uncertainties, with question marks signaling times when elevation is poorly constrained but presumably low. Mc, Oc, Ec, Pc, and LC denote Miocene, Oligocene, Eocene, Paleocene, and Late Cretaceous, respectively.

1988). Significant topographic uplift is inferred since late Miocene from paleosol carbonates [Barke and Lamb, 2006; Ghosh *et al.*, 2006; Schildgen *et al.*, 2007; Thouret *et al.*, 2007] and paleomagnetic data [Rousse *et al.*, 2003]. Gregory-Wodzicki [2000] reached similar conclusions, although leaf morphology studies appear to underestimate paleoelevations [Sempere *et al.*, 2008]. Figure 3 summarizes the tectonic and topographic evolution of the Andes. Notice how the paleoelevation of the mountain chain was likely significantly lower in the Late Cretaceous and Paleocene compared to today, with prominent uplift starting in middle Eocene.

2.3. Regional Upper Mantle Seismic Structure

Upper mantle structure in the South Atlantic region is not well known. Sparsity of seismic stations and the

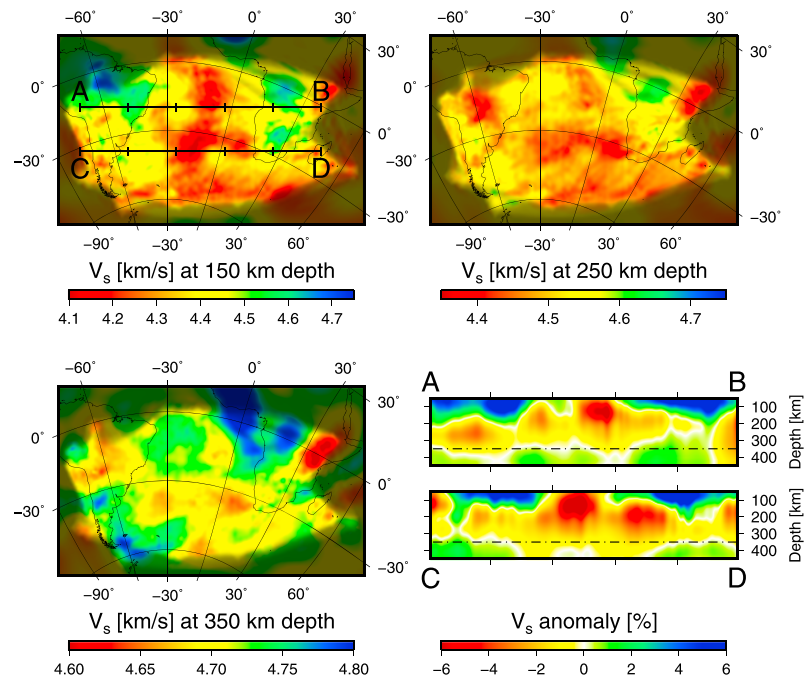


Figure 4. Horizontal slices of upper mantle seismic structure for the South Atlantic region in oblique Mercator projection, together with two vertical transects [Colli *et al.*, 2013]. Shaded regions mark insufficient model resolution. Lines AB and CD on the 150 km depth slice (top left) show location of the two vertical transects (bottom right). The mantle is overall slow, except for fast continental roots, with slow anomalies elongated in a generally east-west direction. The pronounced slow seismic anomalies cease below about 350 km depth, where the structure transitions into a pattern dominated by vertically oriented, columnar slow anomalies embedded in an overall faster mantle.

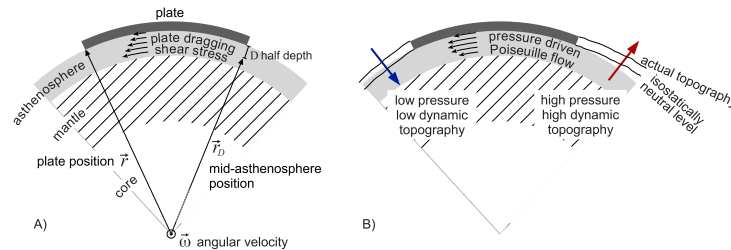


Figure 5. Diagram illustrating geometry and main features of (a) the tectonic force balance model and (b) the fluid dynamic scaling analysis. The tectonic model assumes a rigid plate overlying an isoviscous asthenosphere of constant thickness, allowing us to estimate the excess velocity in the asthenosphere needed to balance all other tectonic forces through basal drag (see equation (2)). The fluid dynamic scaling analysis ascribes the excess velocity explicitly to a pressure-driven Poiseuille flow, whose implications for spatial variations of dynamic topography are shown.

existence of large aseismic areas on the African and South American plates make it difficult to image seismic heterogeneity especially beneath the ocean.

The oceanic upper mantle is imaged primarily by global tomographic studies [e.g., *Houser et al.*, 2008; *Kustowski et al.*, 2008; *Panning and Romanowicz*, 2006; *Ritsema et al.*, 2011; *Shapiro and Ritzwoller*, 2002; *Simmons et al.*, 2006]. These reveal overall lower than average seismic velocities, although details differ for scales less than ~ 2000 km [*Becker and Boschi*, 2002; *Dziewonski*, 2005]. Some differences may originate from different data sets and model parameterization, whereas others may reflect the approximations associated with raypath tomography [*Spetzler et al.*, 2002; *Wang and Dahlen*, 1995; *Zhou et al.*, 2005].

Here we take the recent regional tomographic study of *Colli et al.* [2013], based on long-period surface and body waves inverted with a full-waveform methodology, providing a good resolution of the upper South Atlantic mantle above 400 km depth. Figure 4 shows horizontal slices through the model and two vertical transects. While the mantle in the South Atlantic region is overall slow, except for fast continental roots, the vertical transects show a pattern of pronounced slow seismic anomalies that is quite shallow and ceases below about 350 km. At greater depth the horizontal slow seismic velocity anomalies give way to vertically oriented, columnar slow seismic anomalies embedded in a faster mantle. Similar slow velocity anomalies, elongated in the general direction of plate motion, were reported recently for other oceanic basins [e.g., *French et al.*, 2013; *Lekić and Romanowicz*, 2011; *Rickers et al.*, 2013].

3. Torque Balance Estimates for the South American Plate

To explore possible causes of the velocity changes in the South Atlantic spreading history, we estimate the tectonic torques acting upon the South American plate from 1-D torque balance models. Such models have a long history [e.g., *Forsyth and Uyeda*, 1975] and, although highly simplified and conceptual, have the advantage of keeping the various tectonic torques separate and identifiable. Combined with geological and geophysical considerations, this allows us to disregard those forces that, due to their known slow temporal variation, cannot produce the rapid variations in the spreading rate.

We start by separating the total tectonic torque into net pull (\vec{M}_{sp}) exerted on the trailing plate by lithospheric slabs descending into Earth's mantle, gravitational spreading of large topographic features such as continental plateaus (\vec{M}_{mb}) or thermally subsiding oceanic lithosphere (the latter is known as the *ridge push*, which we denote here as \vec{M}_{rp}), viscous stresses associated with basal drag at the base of the lithosphere (\vec{M}_{bd}) arising from mantle convective motions, and frictional torques along the uppermost, brittle zone of plate margins (\vec{M}_{fr}). Basal drag is often assumed to resist plate motions but may as well drive it. No slab is currently attached to South America or has one been since at least the Mesozoic. The motion of South America is then governed by a balance of the following torques:

$$\vec{M}_{fr} + \vec{M}_{mb} + \vec{M}_{rp} + \vec{M}_{bd} = 0. \quad (1)$$

For present-day conditions, each torque may be estimated with reasonable confidence. *Molnar and Stock* [2009] quantified gravitational spreading of continental plateaus through energy balance arguments.

Table 1. Flow Velocities at Present Day Within the Asthenosphere Beneath the South American Plate Required by the Torque Balance (See Equation (2)) to Sustain Current Andean Elevation for a Variety of Asthenosphere Thickness and Viscosity Combinations^a

Viscosity	Asthenosphere Channel Thickness				
	100 km	200 km	300 km	400 km	500 km
1×10^{18} Pa s	81.2	154.5	226.7	298.5	370.0
5×10^{18} Pa s	17.5	32.2	46.6	61.0	75.3
1×10^{19} Pa s	9.5	16.9	24.1	31.3	38.4
5×10^{19} Pa s	3.2	4.6	6.1	7.5	8.9
1×10^{20} Pa s	2.4	3.1	3.8	4.5	5.3

^aUnits are cm/yr. Flow velocities are reported for the middepth of the asthenosphere, where the Poiseuille flow component is close to maximum. Preferred thickness-viscosity combination is marked in boldface.

Ridge push is estimated from the isostatic balance of oceanic lithosphere [e.g., Fowler, 1990], while torques associated with frictional sliding along western South America may be assessed from the effective friction coefficient along plate margins, which we assume depends primarily on the sediment intake [e.g., Iaffaldano, 2012] and tends to be low relative to a Byerlee estimate [Carena and Moder, 2009; Iaffaldano et al., 2006; Suppe, 2007]. For basal drag from a Newtonian viscous mantle, we write

$$\vec{M}_{bd} = \int_A \left[\vec{r} \times \mu \frac{d\vec{v}}{dr} \right] dA, \quad (2)$$

where the shear stress on the plate base at position \vec{r} is the product of viscosity (μ) and radial velocity gradient, while A is the basal plate area (see Figure 5a for a sketch of model geometry). To clarify the dependence of the numerical results on model parameters, one may approximate the velocity gradient by assuming a linear increase with depth:

$$\vec{M}_{bd} = \int_A \left[\vec{r} \times \mu_D \frac{\vec{v}_a - \vec{v}_p}{D} \right] dA,$$

where \vec{v}_p is the plate velocity, \vec{v}_a is the flow at depth D within the asthenosphere, which we choose to be the midpoint of the asthenospheric layer, and μ_D is the viscosity averaged from the plate base to depth D . Plates can be approximated as rigid bodies whose motions are described by Euler vectors ($\vec{\omega}_p$). The mantle, in contrast, behaves as a viscous fluid. For clarity we assume nevertheless that asthenosphere flow beneath the South Atlantic realm may be approximated crudely using a time-dependent Euler vector ($\vec{\omega}_a$), with $|\vec{r}_D| = (r - D)$, and obtain

$$\begin{aligned} \vec{M}_{bd} &= \int_A \left[\vec{r} \times \mu_D \frac{(\vec{\omega}_a \times \vec{r}_D) - (\vec{\omega}_p \times \vec{r})}{D} \right] dA \\ &= \int_A \left[\vec{r} \times \mu_D \frac{\vec{\omega}_a \times \vec{r}_D}{D} \right] dA - \int_A \left[\vec{r} \times \mu_D \frac{\vec{\omega}_p \times \vec{r}}{D} \right] dA. \end{aligned} \quad (3)$$

Equation (3) shows that this torque has two parts [Höink et al., 2011]. The first integral is the Poiseuille component of mantle flow, while the second provides an estimate of the Couette counterpart associated with plate motions. The unknowns are $\vec{\omega}_a$, D , and μ_D , whereas the area and Euler vector of the plate may be inferred from the geologic record. Substituting (3) into (1) allows us to solve for $\vec{\omega}_a$ and the associated basal drag M_{bd} needed to balance the current Andean elevation. We consider a number of combinations of D and μ_D in Table 1, showing that mantle flow velocities scale with D/μ_D , as expected.

The South Atlantic spreading record allows us to extend our scaling to earlier times. To this end, we assume steady mantle flow, constant frictional forces, and constant ridge push since the latest Mesozoic. These assumptions, although simplifying, are motivated by the fact that all these three force components are expected to vary smoothly and over longer timescales with respect to the observed spreading rate variations. For instance, mantle flow changes significantly over time intervals of the order of the transit time (100 Myr), which is the time necessary to cross the mantle by advection. Ridge push increases linearly with plate age for a half-space cooling model or to an asymptote assuming a plate cooling model. In this case, equation (1) allows us to relate the South American velocity record to temporal variations in the torques associated with the Andes. In other words, we equate spreading changes ($\Delta\vec{\omega}_p$) exclusively with changes in the orogenic load

$$\Delta\vec{M}_{mb} = \int_A \left[\vec{r} \times \mu_D \frac{\Delta\vec{\omega}_p \times \vec{r}}{D} \right] dA. \quad (4)$$

Our scaling makes an explicit prediction—relative to today—for the evolution of Andean elevation.

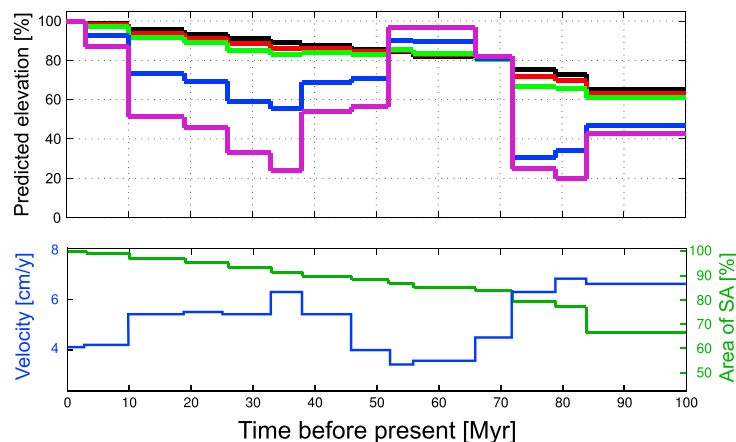


Figure 6. (top) Predicted evolution of Andean paleoelevation, in percent of present elevation, required to balance temporal variations in South American plate velocity and size since mid-Cretaceous, for a variety of asthenosphere viscosities. Black, red, green, blue, and purple lines correspond to 1×10^{18} Pa s, 5×10^{18} Pa s, 1×10^{19} Pa s, 5×10^{19} Pa s, and 1×10^{20} Pa s, respectively. (bottom) Reconstructed South American plate area (green curve) and spreading rate (blue curve) according to the Earthbyte model. Note that for low viscosities (green, black, and red curves in Figure 6, top), estimated Andean paleoelevation scales with South American plate area, while it scales inversely with the plate velocity for higher viscosities (blue and purple curves). Comparison with Figure 3 shows that high- and low-viscosity end-members are both incompatible with geologic inferences of Andean topographic evolution.

Figure 6 shows our results for a range of mantle viscosities, assuming a 300 km thick asthenosphere channel, as suggested by our tomographic results (Figure 4). Two end-member regimes are apparent. For low asthenosphere viscosities and correspondingly high flow velocities, the plate velocity changes imply minor changes in the effective basal drag. In other words, the recorded spreading changes are small relative to the assumed upper mantle flow velocities (Table 1). In this case, inferred elevation changes scale directly with the plate size (compare black, red, and green curves with plate size in Figure 3), and we predict that the mountain chain would remain high throughout the Cenozoic to balance the effective torques. Assuming larger asthenosphere viscosities and correspondingly lower mantle flow velocities instead, the recorded South American plate motion history implies significant basal drag changes. Correspondingly, large temporal changes in the height of the Andes are required to balance the evolving shear stress. Inferred Andean elevation in this case scales inversely with the spreading history (compare blue and purple curves to Figure 2).

Both end-members are incompatible with the inferred topographic evolution of the Andes (Figure 3), and we find that the early Tertiary South Atlantic spreading variations cannot be attributed to Andean elevation changes. All combinations of model parameters yield estimates for the average Andean elevation in Late Cretaceous and early Paleocene that are too large (50% or higher from ~ 70 to ~ 40 Myr) compared to geologic constraints. Hence, we deduce that our assumptions of steady Poiseuille flow and steady basal drag are unrealistic. It seems logical then to consider an unsteady flow component that evolves on shorter timescales than the pattern of large-scale mantle circulation driven by temporal pressure variations in the asthenosphere beneath the South Atlantic region.

4. Asthenosphere Flow

Rapid spreading rate changes in the South Atlantic imply decoupling of plate motion from the large-scale mantle buoyancy distribution, presumably through a mechanically “weak” (i.e., low viscosity) asthenosphere. Postglacial rebound (PGR) provides one of our most direct constraints on mantle rheology. Since the pioneering work of *Haskell* [1935], where he calculated the viscosity of the upper part of the mantle to be $\sim 10^{21}$ Pa s (known as Haskell constraint), PGR studies focused on resolving the radial mantle viscosity distribution. A general consensus exists that the average viscosity of the sublithospheric upper mantle is smaller than that of the deeper mantle, even if the amount of viscosity contrast and the thickness of the

Table 2. Calculated Poiseuille Mantle Flow Velocities in cm/yr in an Asthenosphere Channel Beneath the South Atlantic Region for a Pressure Gradient of 300 Bar Across the Basin and a Variety of Channel Widths and Asthenosphere Viscosities (See Text)^a

Viscosity	Asthenosphere Channel Thickness				
	100 km	200 km	300 km	400 km	500 km
1×10^{18} Pa s	16.9	67.6	152.0	270.3	422.3
5×10^{18} Pa s	3.4	13.5	30.4	54.1	84.5
1×10^{19} Pa s	1.7	6.7	15.2	27.0	42.2
5×10^{19} Pa s	0.3	1.3	3.0	5.4	8.4
1×10^{20} Pa s	0.2	0.7	1.5	2.7	4.2

^aFlow velocities are reported for the middepth of the asthenosphere, where the Poiseuille flow component is close to maximum. Preferred thickness-viscosity combination is marked in boldface.

ity reduction. The trade-off exists also in modeling the geoid [Schaber *et al.*, 2009] and arises because the decay time τ varies linearly with viscosity μ and inversely with h^3 [Cathles, 1975], in the limit of a small-layer thickness h relative to the loading wavelength:

$$\tau \propto \frac{\mu}{h^3}.$$

Equivalently, in the long-wavelength limit, the load may be accommodated by horizontal (Poiseuille) flow in the low-viscosity layer. The significant parameter here is the volumetric flow rate [Davies, 1999], dependent on μ and h^3 , where P' is a pressure gradient:

$$Q = \frac{P'h^3}{12\mu},$$

Assuming the low seismic velocity layer imaged in Figure 4 indicates a low-viscosity channel, a channel thickness of about 300 km, and the Haskell constraint yields an effective viscosity of $\sim 10^{19}$ Pa s.

In addition to spreading rate changes, the South Atlantic sustains a topography gradient which is likely of dynamic origin (see Figures 1c and 5b). On the eastern side, elevated topography, termed the *African superswell* [Nyblade and Robinson, 1994], consists of uplifted portions of the African continent and areas of abnormally high bathymetry in the southeastern Atlantic, whereas much of the southwestern Atlantic, especially in the Argentine Basin, is abnormally deep. The basin-wide dynamic topography gradient in excess of ~ 1 km implies lateral pressure differences in excess of ~ 300 bar. Significant pressure-driven (Poiseuille) flow is thus expected in the sublithospheric mantle. Supporting evidence for westward fluxing upper mantle comes from seismically imaged flow-like structures [French *et al.*, 2013] and geodynamic investigations of upper mantle flow around the southern tip of South America [Nerlich *et al.*, 2013]. The magnitude of Poiseuille flow is readily calculated

$$V_m = \frac{h^2 \Delta P}{8\eta \Delta x}, \quad (5)$$

where ΔP is the pressure difference and Δx is the length scale across the basin. The computed flow velocities depend on the assumed viscosity (η) and thickness (h) of the channel (Table 2). A channel thickness of 300 km, together with an assumed asthenosphere viscosity of 10^{19} Pa s yields good agreement between velocities predicted from pressure-driven flow and those required to sustain the current Andean load through basal shear (Table 1).

5. Spreading Rate Changes and Coeval Epeirogenic Motion in the South Atlantic Region

It seems likely that temporal variations in upper mantle flow associated with temporal changes of pressure gradients should be linked to changes in dynamic topography. This linkage between changes in horizontal and vertical motion can be tested with geologic data. As noted earlier, the South Atlantic has a bimodal spreading history (Figure 2) with high spreading rates in Late Cretaceous and Eo-Oligocene. Thus, it is reasonable to explore the consequences for regional dynamic topography from attributing these changes to unsteady upper mantle flow induced by temporal variations of the pressure gradients in the asthenosphere.

low-viscosity layer remain debated. *Mitrovica* [1996] noted the Haskell constraint applies effectively to mantle depths of ~ 1000 – 1200 km, while *Paulson and Richards* [2009] drew attention to the trade-off between radial viscosity contrast and layer thickness: models favoring a coarse subdivision of the mantle into two layers separated at the 670 km phase transition will naturally obtain modest viscosity contrasts, while providing an equally good fit to the data as models with a thin layer and strong viscos-

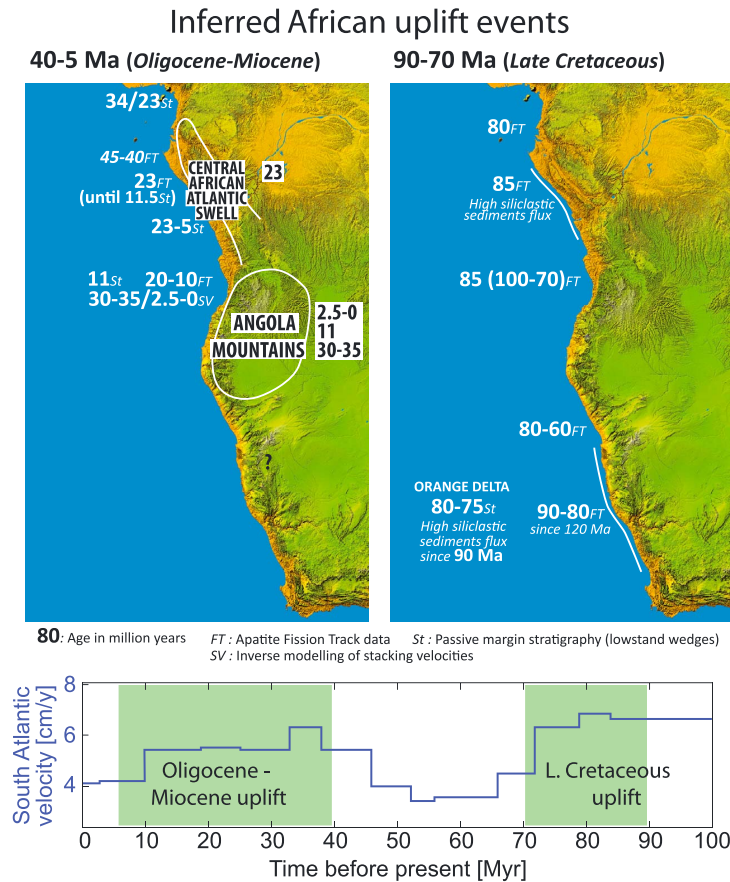


Figure 7. Main uplift events in Oligocene-Miocene (5–40 Myr) and Late Cretaceous (70–90 Myr) time along Africa’s South Atlantic margin as inferred from a variety of techniques: thermochronology (FT), sequence stratigraphy (St), and inverse modeling of stacking velocities from seismic lines (SV). The bottom panel shows that times of widespread uplift (shaded intervals) correlate with times of faster spreading.

Topography in the South Atlantic realm has changed over time. *Japsen et al.* [2012a] and *Cogne et al.* [2011] document Late Cretaceous and Eocene uplift events along the Brazilian coast. *MacGregor* [2012] summarizes margin uplifts for South America and Africa in Late Cretaceous and Oligocene. Since the seminal work by *King* [1955] a consensus exists [e.g., *Partridge and Maud*, 1987] that Southern Africa’s topography had experienced successive phases of planation by scarp retreat that produced low-relief pediplain that could be correlated across the continent (e.g., the Gondwana and the African surface). *King* [1955] proposed that episodic regional uplift caused these events.

The African side of the South Atlantic has three main relief elements: South African Plateau, Angola Mountains, and Congo-Cameroon Atlantic Swell. The uplift ages of these structures have been debated with three main scenarios. (1) Inheritance from Atlantic rifting [e.g., *Gilchrist et al.*, 1994], (2) Late Cretaceous [e.g., *de Wit*, 2007], and (3) Oligo-Miocene [e.g., *Burke and Gunnell*, 2008]. Geologic data (Figure 7) now suggest two main uplift periods, Late Cretaceous and Oligo-Miocene, with different amplitudes from South Africa to Cameroon. Late Cretaceous uplifts are documented by apatite fission track (AFT) data in Gabon [*Walgenwitz et al.*, 1992], South Africa-Namibia [*Gallagher and Brown*, 1999a, 1999b; *Kounov et al.*, 2009; *Raab et al.*, 2002, 2005; *Stanley et al.*, 2013], and Equatorial Guinea [*Turner et al.*, 2008]. Significant vertical displacement is also confirmed by numerous lowstand wedges along the margins [*Hartwig et al.*, 2012; *Hirsch et al.*, 2010;

McMillan, 2003; Paton *et al.*, 2008]. Supporting evidence comes from siliciclastic flux measurements. While these record continental denudation, not necessarily uplift, they are consistent with a major Late Cretaceous denudation event [Anka *et al.*, 2010; Guillocheau *et al.*, 2012; Leturmy *et al.*, 2003; MacGregor, 2012; Seranne and Anka, 2005].

The Oligo-Miocene uplift is also documented on AFT data along the Congo-Cameroon Atlantic Swell [Walgenwitz *et al.*, 1992] and the Angola Mountains [Jackson *et al.*, 2005], confirming the pioneering work of Lunde *et al.* [1992]. On the Angola margin, inverse modeling of stacking velocities along offshore seismic lines [Al-Hajri *et al.*, 2009; Walford and White, 2005] finds two major uplifts in early Oligocene and Pleistocene. Lowstand wedges and incised canyons were preserved along the Congo Delta [Anka *et al.*, 2009], and the Cameroon-Gabon margins, with canyon incision around the Eo-Oligocene boundary in Cameroon and major lowstand wedges in early Miocene [Manga, 2008; Rasmussen, 1996]. Along the Congo margin, paleowater depth reconstructions [Lavie *et al.*, 2001] and modeling of vertical movements [Lucazeau *et al.*, 2003] show similar uplift timing. Sedimentary flux analysis confirms the second denudation period [MacGregor, 2012; Seranne and Anka, 2005], with a strong increase along the Congo-Ogooué (Gabon) deltaic system [Anka *et al.*, 2009; Lavie *et al.*, 2001; Leturmy *et al.*, 2003].

These two major uplift events correlate with pulses in regional basin reactivation [Janssen *et al.*, 1995] and magmatic activity [Jelsma *et al.*, 2009; O'Connor *et al.*, 2012].

6. Discussion

Our results suggest that topographic variations of the Andes alone cannot fully account for the South Atlantic spreading changes. The most recent South Atlantic spreading reduction correlates with late Miocene Andean uplift. However, the elevation of the Andes was small in Late Cretaceous and Early Paleocene, relative to the present day, and presumably did not vary much in time. Thus, the pronounced early Tertiary spreading rate variations in the South Atlantic are not easily linked to elevation changes in the Andes.

At the same time, substantial evidence suggests that the bimodal spreading history of the South Atlantic is matched by a bimodal history of uplift on the South American and African sides of the South Atlantic [MacGregor, 2012]. A linkage between changes in horizontal and vertical motion is expected if temporal variations in upper mantle flow arise from temporal variations of pressure gradients in the asthenosphere. In this case, the evolving flow field would be associated with evolving basal shear forces and nonisostatic vertical motion that is dynamic topography.

6.1. Unmodeled Effects

We must emphasize that our force balance models and our fluid dynamic analysis of upper mantle flow are highly simplified. We have assumed a rigid plate overlying an incompressible Newtonian asthenosphere of constant thickness, disregarding among others the complex 3-D structure of the asthenosphere in the South Atlantic region that is imaged, for instance, by our tomographic study [Colli *et al.*, 2013]. Furthermore, we did not account for the complex rheological behavior of mantle material, and we considered the momentum equation alone, without coupling it to the heat and mass conservation equations in a self-consistent and time-dependent model. At this stage, however, we believe it is prudent to explore simple models of the South Atlantic region, aimed at providing physical insight, before moving to complex computational simulations that carry their own limitations. For example, a fully time-dependent geodynamic model of the plate tectonic evolution of the South Atlantic region would require the choice of an appropriate initial condition. While fluid dynamic inverse theory of mantle convection has been developed during the last decade [Bunge *et al.*, 2003; Ismail-Zadeh *et al.*, 2004], its application to the initial condition problem with real geophysical data remains challenging.

In our analysis of South Atlantic spreading variations, we did not account for changes in plate geometry offshore of the western margin of South America, which acquired its current shape since the Neogene as evidenced by paleomagnetic and geodetic studies [e.g., Allmendinger *et al.*, 2005, and references therein]. Paleoplate configurations recently published by Müller *et al.* [2008] and Seton *et al.* [2012], see Figure 8, suggest that plate motion was oblique along the central and northern Chilean margin before the Eocene, when the current subduction geometry was established. While it is not obvious how this plate geometry change would induce a deceleration and subsequent acceleration in South Atlantic spreading rates around the

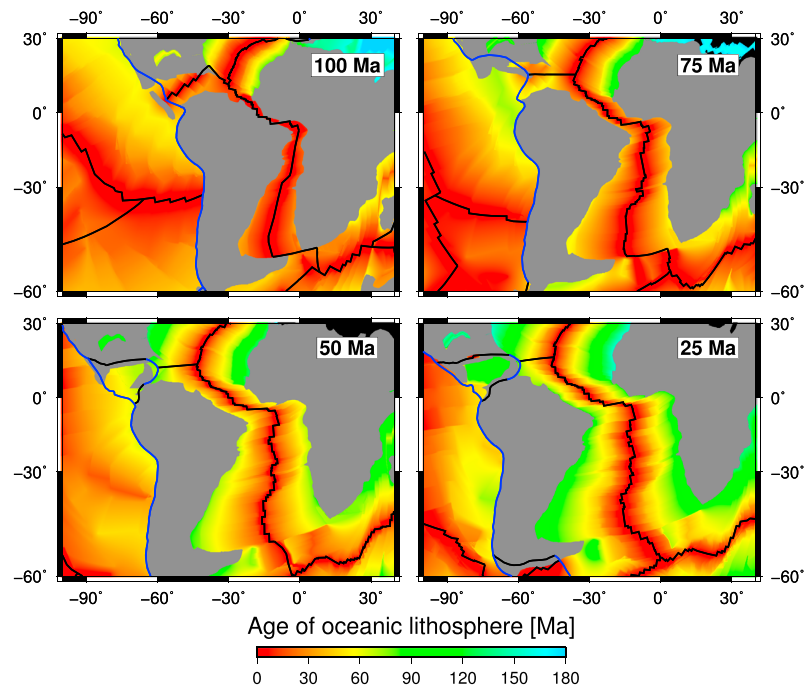


Figure 8. Plate configurations and ocean floor age in the South Atlantic region for four time periods (100 to 25 Myr) from Müller *et al.* [2008]. Note that oblique subduction off western South America is inferred to have changed into the current trench-perpendicular subduction from the Eocene (≈ 50 Myr) on, with a corresponding change from trench-parallel to trench-perpendicular motion.

Cretaceous/Tertiary boundary, or how this would explain the recent Eo-Oligocene uplift events recorded on the African continent, its influence should be investigated further.

We also assumed a constant friction coefficient of the South American plate boundaries, including the Andean margin, for the Cenozoic. The friction coefficient of megathrusts and marine plate margins could be regulated by the amount of sediments delivered to the margin—with the highest coefficient associated with sediment-starved margins, such as the present-day Chilean trench offshore the Altiplano-Puna Plateaus [Lamb, 2006; Seno, 2009]. Although semiarid climatic conditions prevailed during most of the Paleocene along the northernmost Chilean fore arc, Hartley [2003] proposed increased local aridity since the Oligocene as a dominant control on the rise of the Andean Plateau. This calls for a reduction of the amount of sediments transported from the fore arc into the trench and a subsequent increase of the interplate friction coefficient [Lamb and Davis, 2003; Oncken *et al.*, 2006]. However, variations of the effective friction coefficient along plate margins are unlikely to exceed 0.06 [Iaffaldano, 2012]. Moreover, any such variations along the Andean margin would have been restricted to a relatively minor portion of the total South American plate boundary. It is thus reasonable to expect no significant impact upon the torque balance and kinematics of the South American plate [e.g., Iaffaldano and Bunge, 2008].

6.2. Implications

Our results suggest it is possible to exploit the oceanic spreading record to quantify some of the forces involved in driving and resisting plate motion. Plate tectonics explains the piecewise constant nature of surface velocities on our planet [DeMets *et al.*, 1994], but the nature and magnitude of the driving and resisting forces remain obscure. The difficulty stems from three sources. First, the mantle buoyancy forces are not well known, although combining mantle convection simulations with mantle mineralogy models [Piazzoni *et al.*, 2007] may shed light on how to interpret mantle seismic structure in terms of density anomalies [Forte *et al.*, 2010; Schuberth *et al.*, 2009a, 2009b, 2012]. Second, we lack robust descriptions of the mantle

deformation behavior in the regime of low strain rates, high temperature, and high pressure that characterizes the deep Earth. Theoretical progress from multiscale material modeling [Castelnaud *et al.*, 2010] may allow one to augment experimental work to better understand from first principle the deformation of mantle minerals [Ammann *et al.*, 2010; Cordier *et al.*, 2012]. The third challenge reflects the fact that the inertia of moving plates is negligible so that tectonic forces balance everywhere on Earth. Our ability to consider past and present plate velocities is thus essential to quantify the forces, because plate motion changes are necessarily driven by changes in the driving or resisting forces.

7. Conclusions

We have investigated the South Atlantic region in terms of spreading history, Andean topographic evolution, and upper mantle seismic structure, focusing on prominent short-term spreading velocity changes recorded in the basin. The far-field effects of the Andes on the South Atlantic spreading record are relatively straightforward. Rapid Andean topographic growth in the Miocene correlates with a recent reduction in South Atlantic spreading velocity, likely due to increased plate boundary forcing associated with the newly elevated topography. The twofold reduction in South Atlantic spreading velocity and subsequent renewed vigorous spreading at the Cretaceous/Tertiary boundary, in contrast, lack such correlation, as Andean paleoelevation at the time presumably was low. Torque balance models demonstrate that the Late Cretaceous/Tertiary spreading changes could arise from variations in basal drag associated with unsteady asthenosphere flow. The magnitude of the pressure-induced mantle flow velocities compares well with those required from independent considerations to maintain South American plate motion through basal shear. Predictions from our models for temporal changes in regional topography, due to temporal changes in pressure gradients and upper mantle flow, appear to agree with geologic and geophysical observations, including episodes of passive margin uplift, regional basin reactivation, and magmatic activity.

Acknowledgments

No new data were produced during this work. All data used come from the sources referenced in the text. We would like to thank Seth Stein, Adrian Lenardic, and an anonymous reviewer for their thoughtful and constructive reviews, and Peter Japsen for helpful discussions. The work of Lorenzo Colli, Hans-Peter Bunge, and Maria Chiara Bianchi was funded by the German Research Foundation (DFG) within the priority program SPP 1375—SAMPLE. Stuart Clark and Mark Smethurst conducted the work as part of a research grant from Statoil. Giampiero laffaldano acknowledges support from the Ringwood Fellowship at the Australian National University. François Guillocheau would like to thank the Agence Nationale de la Recherche (ANR-French Research National Agency) for funding the TopoAfrica project. The work of Lorenzo Colli was partially supported by COST Action ES0701.

References

- Al-Hajri, Y., N. White, and S. Fishwick (2009), Scales of transient convective support beneath Africa, *Geology*, 37(10), 883–886, doi:10.1130/G25703A.1.
- Allmendinger, R., R. Smalley, M. Bevis, H. Caprio, and B. Brooks (2005), Bending the Bolivian orocline in real time, *Geology*, 33(11), 905–908, doi:10.1130/G21779.1.
- Amante, C., and B. W. Eakins (2009), *ETOPO1 1 Arc-Minute Global Relief Model: Procedures, Data Sources and Analysis*, NOAA Technical Memorandum NESDIS NGDC-24, U.S. Dept. of Commerce, National Oceanic and Atmospheric Administration, National Environmental Satellite, Data, and Information Service, National Geophysical Data Center, Marine Geology and Geophysics Division, Boulder, Colo.
- Ammann, M. W., J. P. Brodtholt, J. Wookey, and D. P. Dobson (2010), First-principles constraints on diffusion in lower-mantle minerals and a weak D" layer, *Nature*, 465(7297), 462–465, doi:10.1038/nature09052.
- Anderson, D. L. (1982), Hotspots, polar wander, Mesozoic convection and the geoid, *Nature*, 297, 391–393.
- Anderson, D. L., and C. Sammis (1970), Partial melting in the upper mantle, *Phys. Earth Planet. Inter.*, 3, 41–50, doi:10.1016/0031-9201(70)90042-7.
- Anka, Z., M. Seranne, M. Lopez, M. Scheck-Wenderoth, and B. Savoye (2009), The long-term evolution of the Congo deep-sea fan: A basin-wide view of the interaction between a giant submarine fan and a mature passive margin (ZaiAngo project), *Tectonophysics*, 470(1–2), 42–56, doi:10.1016/j.tecto.2008.04.009.
- Anka, Z., M. Seranne, and R. di Primio (2010), Evidence of a large upper-Cretaceous depocentre across the Continent-Ocean boundary of the Congo-Angola basin. Implications for palaeo-drainage and potential ultra-deep source rocks, *Mar. Pet. Geol.*, 27(3), 601–611, doi:10.1016/j.marpetgeo.2009.08.015.
- Barke, R., and S. Lamb (2006), Late Cenozoic uplift of the Eastern Cordillera, Bolivian Andes, *Earth Planet. Sci. Lett.*, 249(3–4), 350–367, doi:10.1016/j.epsl.2006.07.012.
- Barnes, J., T. Ehlers, N. McQuarrie, P. O'Sullivan, and J. Pelletier (2006), Eocene to recent variations in erosion across the central Andean fold-thrust belt, northern Bolivia: Implications for plateau evolution, *Earth Planet. Sci. Lett.*, 248(1–2), 118–133, doi:10.1016/j.epsl.2006.05.018.
- Barrell, J. (1914), The strength of the Earth's crust part VI Relations of isostatic movements to a sphere of weakness—The asthenosphere, *J. Geol.*, 22(7), 655–683.
- Becker, T. W., and L. Boschi (2002), A comparison of tomographic and geodynamic mantle models, *Geochem. Geophys. Geosyst.*, 3(1), 1003, doi:10.1029/2001GC000168.
- Bond, G. (1978), Evidence for late tertiary uplift of Africa relative to North-America, South-America, Australia and Europe, *J. Geol.*, 86(1), 47–65.
- Braun, J. (2010), The many surface expressions of mantle dynamics, *Nat. Geosci.*, 3(12), 825–833, doi:10.1038/NNGEO1020.
- Buck, W. R., C. Small, and W. B. F. Ryan (2009), Constraints on asthenospheric flow from the depths of oceanic spreading centers: The East Pacific Rise and the Australian-Antarctic discordance, *Geochem. Geophys. Geosyst.*, 10, Q09007, doi:10.1029/2009GC002373.
- Bullard, E., J. Everett, and A. Smith (1965), The fit of the continents around the Atlantic, *Philos. Trans. R. Soc. London, Ser. A*, 258(1088), 41–51, doi:10.1098/rsta.1965.0020.
- Bunge, H.-P. (2005), Low plume excess temperature and high core heat flux inferred from non-adiabatic geotherms in internally heated mantle circulation models, *Phys. Earth Planet. Inter.*, 153(1–3), 3–10, doi:10.1016/j.pepi.2005.03.017.
- Bunge, H.-P., M. A. Richards, and J. R. Baumgardner (1996), Effect of depth-dependent viscosity on the planform of mantle convection, *Nature*, 379, 436–438.

- Bunge, H.-P., M. A. Richards, C. Lithgow-Bertelloni, J. R. Baumgardner, S. P. Grand, and B. A. Romanowicz (1998), Time scales and heterogeneous structure in geodynamic Earth models, *Science*, 280(5360), 91–95, doi:10.1126/science.280.5360.91.
- Bunge, H.-P., Y. Ricard, and J. Matas (2001), Non-adiabaticity in mantle convection, *Geophys. Res. Lett.*, 28(5), 879–882.
- Bunge, H.-P., C. R. Hagelberg, and B. J. Travis (2003), Mantle circulation models with variational data assimilation: Inferring past mantle flow and structure from plate motion histories and seismic tomography, *Geophys. J. Int.*, 152(2), 280–301, doi:10.1046/j.1365-246X.2003.01823.x.
- Burke, K., and Y. Gunnell (2008), *The African Erosion Surface: A Continental-Scale Synthesis of Geomorphology, Tectonics, and Environmental Change Over the Past 180 Million Years*, Geol. Soc. Am., Boulder, Colo.
- Busse, F. H., M. A. Richards, and A. Lenardic (2006), A simple model of high Prandtl and high Rayleigh number convection bounded by thin low-viscosity layers, *Geophys. J. Int.*, 164, 160–167, doi:10.1111/j.1365-246X.2005.02836.x.
- Cande, S. C., J. L. LaBrecque, and W. F. Haxby (1988), Plate kinematics of the South Atlantic: Chron C34 to present, *J. Geophys. Res.*, 93(B11), 12,479–13,492.
- Carena, S., and C. Moder (2009), The strength of faults in the crust in the western United States, *Earth Planet. Sci. Lett.*, 287(3–4), 373–384, doi:10.1016/j.epsl.2009.08.021.
- Castelnaud, O., P. Cordier, R. A. Lebensohn, S. Merkel, and P. Raterron (2010), Microstructures and rheology of the Earth's upper mantle inferred from a multiscale approach, *C.R. Phys.*, 11(3), 304–315, doi:10.1016/j.crhy.2010.07.011.
- Cathles, L. (1975), *The Viscosity of the Earth's Mantle*, Princeton Univ. Press, New Jersey.
- Channell, J. E. T., E. Erba, M. Nakanishi, and K. Tamaki (1995), Late Jurassic-Early Cretaceous time scales and oceanic magnetic anomaly block models, in *Geochronology, Time Scales and Global Stratigraphic Correlation*, vol. 54, edited by W. A. Breggin et al., pp. 51–63, SEPM (Society for Sedimentary Geology) Spec. Publ., Tulsa, Okla.
- Charrier, R. (2007), Tectonostratigraphic evolution of the Andean orogen in Chile, in *The Geology of Chile*, edited by T. Moreno and W. Gibbons, *Geol. Soc. London Spec. Publ.*, 21–114.
- Chase, C. G. (1979), Asthenospheric counterflow—A kinematic model, *Geophys. J. R. Astron. Soc.*, 56(1), 1–18, doi:10.1111/j.1365-246X.1979.tb04764.x.
- Coffin, M. F., L. M. Gahagan, and L. A. Lawver (1998), Present-day plate boundary digital data compilation, *Tech. Rep. 174*, Univ. of Tex. Inst. for Geophysics, Austin.
- Cogne, N., K. Gallagher, and P. R. Cobbold (2011), Post-rift reactivation of the onshore margin of southeast Brazil: Evidence from apatite (U-Th)/He and fission-track data, *Earth Planet. Sci. Lett.*, 309(1–2), 118–130, doi:10.1016/j.epsl.2011.06.025.
- Colli, L., A. Fichtner, and H.-P. Bunge (2013), Full waveform tomography of the upper mantle in the South Atlantic region: Evidence for pressure-driven westward flow in a shallow asthenosphere, *Tectonophysics*, 604, 26–40.
- Cordier, P., J. Amodeo, and P. Carrez (2012), Modelling the rheology of MgO under Earth's mantle pressure, temperature and strain rates, *Nature*, 481(7380), 177–180, doi:10.1038/nature10687.
- Cornejo, P. (2003), The K-T compressive deformation event in northern Chile 24–27°S, in *10th Geological Congress*, Actas, CD-Rom, Sesión Temática 1, Concepcion Chile.
- Crosby, A. G., D. McKenzie, and J. G. Sclater (2006), The relationship between depth, age and gravity in the oceans, *Geophys. J. Int.*, 166(2), 553–573.
- Davies, D. R., S. Goes, J. H. Davies, B. S. A. Schuberth, H.-P. Bunge, and J. Ritsema (2012), Reconciling dynamic and seismic models of Earth's lower mantle: The dominant role of thermal heterogeneity, *Earth Planet. Sci. Lett.*, 353–354, 253–269, doi:10.1016/j.epsl.2012.08.016.
- Davies, G. (1999), *Dynamic Earth: Plates, Plumes and Mantle Convection*, Cambridge Univ. Press, New York.
- de Wit, M. (2007), The Kalahari epeirogeny and climate change: Differentiating cause and effect from core to space, *S. Afr. J. Geol.*, 110(2–3), 367–392, doi:10.2113/gssajg.110.2-3.367.
- Debayle, E., B. Kennett, and K. Priestley (2005), Global azimuthal seismic anisotropy and the unique plate-motion deformation of Australia, *Nature*, 433, 509–512, doi:10.1038/nature03247.
- DeMets, C., R. Gordon, D. Argus, and S. Stein (1994), Effect of recent revisions to the geomagnetic reversal time-scale on estimates of current plate motions, *Geophys. Res. Lett.*, 21(20), 2191–2194, doi:10.1029/94GL02118.
- Duncan, R. A., and M. A. Richards (1991), Hotspots, mantle plumes, flood basalts, and true polar wander, *Rev. Geophys.*, 29(1), 31–50, doi:10.1029/90RG02372.
- Dziewonski, A. M. (2005), The robust aspects of global seismic tomography, *Geol. Soc. Am. Spec. Pap.*, 388, 147–154, doi:10.1130/0-8137-2388-4.147.
- Ege, H., E. R. Sobel, E. Scheuber, and V. Jacobshagen (2007), Exhumation history of the southern Altiplano Plateau (southern Bolivia) constrained by apatite fission track thermochronology, *Tectonics*, 26(1), TC1004, doi:10.1029/2005TC001869.
- Forsyth, D., and S. Uyeda (1975), Relative importance of driving forces of plate motion, *Geophys. J. R. Astron. Soc.*, 43(1), 163–200, doi:10.1111/j.1365-246X.1975.tb00631.x.
- Forté, A. M., S. Quere, R. Moucha, N. A. Simmons, S. P. Grand, J. X. Mitrovica, and D. B. Rowley (2010), Joint seismic-geodynamic-mineral physical modelling of African geodynamics: A reconciliation of deep-mantle convection with surface geophysical constraints, *Earth Planet. Sci. Lett.*, 295(3–4), 329–341, doi:10.1016/j.epsl.2010.03.017.
- Fowler, C. (1990), *The Solid Earth: An Introduction to Global Geophysics*, Cambridge Univ. Press, Cambridge.
- French, S., V. Lekic, and B. Romanowicz (2013), Waveform tomography reveals channeled flow at the base of the oceanic asthenosphere, *Science*, 342, 227–330, doi:10.1126/science.1241514.
- Gallagher, K., and R. Brown (1999a), Denudation and uplift at passive margins: The record on the Atlantic Margin of Southern Africa, *Philos. T. Roy. Soc. A*, 357(1753), 835–857.
- Gallagher, K., and R. Brown (1999b), The Mesozoic denudation history of the Atlantic margins of Southern Africa and southeast Brazil and the relationship to offshore sedimentation, in *The Oil and Gas Habitats of the South Atlantic*, edited by N. R. Cameron, and R. H. Bate, and V. S. Clure, *Geol. Soc. London Spec. Publ.*, 153, 41–53.
- Gansser, A. (1973), Facts and theories on the Andes, *J. Geol. Soc. London*, 129, 93–131.
- Garzzone, C. N., P. Molnar, J. C. Libarkin, and B. J. MacFadden (2006), Rapid late Miocene rise of the Bolivian Altiplano: Evidence for removal of mantle lithosphere, *Earth Planet. Sci. Lett.*, 241(3–4), 543–556, doi:10.1016/j.epsl.2005.11.026.
- Ghosh, P., C. N. Garzzone, and J. M. Eiler (2006), Rapid uplift of the Altiplano revealed through C-13-O-18 bonds in paleosol carbonates, *Science*, 311(5760), 511–515, doi:10.1126/science.1119365.
- Gilchrist, A., H. Kooi, and C. Beaumont (1994), Post-Gondwana geomorphic evolution of southwestern Africa—Implications for the controls on landscape development from observations and numerical experiments, *J. Geophys. Res.*, 99(B6), 12,211–12,228, doi:10.1029/94JB00046.

- Gillis, R. J., B. K. Horton, and M. Grove (2006), Thermochronology, geochronology, and upper crustal structure of the Cordillera Real: Implications for Cenozoic exhumation of the central Andean Plateau, *Tectonics*, 25(6), TC6007, doi:10.1029/2005TC001887.
- Gradstein, F. M., J. G. Ogg, A. G. Smith, W. Bleeker, and L. J. Lourens (2004), A new geologic time scale, with special reference to Precambrian and Neogene, *Episodes*, 27(2), 83–100.
- Grand, S. P. (2002), Mantle shear-wave tomography and the fate of subducted slabs, *Philos. Trans. R. Soc. London, Ser. A*, 360(1800), 2475–2491.
- Gregory-Wodzicki, K. (2000), Uplift history of the Central and Northern Andes: A review, *Geol. Soc. Am. Bull.*, 112(7), 1091–1105, doi:10.1130/0016-7606(2000)112<1091:UHOTCA>2.3.CO;2.
- Guillocheau, F., D. Rouby, C. Robin, C. Helm, N. Rolland, C. L. C. de Veslud, and J. Braun (2012), Quantification and causes of the terrigenous sediment budget at the scale of a continental margin: A new method applied to the Namibia-South Africa margin, *Basin Res.*, 24(1), 3–30, doi:10.1111/j.1365-2117.2011.00511.x.
- Harig, C., S. Zhong, and F. J. Simons (2010), Constraints on upper mantle viscosity from the flow-induced pressure gradient across the Australian continental keel, *Geochem. Geophys. Geosyst.*, 11, Q06004, doi:10.1029/2010GC003038.
- Hartley, A. (2003), Andean uplift and climate change, *J. Geol. Soc. London*, 160(1), 7–10, doi:10.1144/0016-764902-083.
- Hartwig, A., Z. Anka, and R. di Primio (2012), Evidence of a widespread paleo-pockmarked field in the Orange Basin: An indication of an early Eocene massive fluid escape event offshore South Africa, *Mar. Geol.*, 332, 222–234, doi:10.1016/j.margeo.2012.07.012.
- Haskell, N. A. (1935), The motion of a viscous fluid under a surface load, *J. Appl. Phys.*, 6(1), 265–269, doi:10.1063/1.1745329.
- Hirsch, K. K., M. Scheck-Wenderoth, J.-D. van Wees, G. Kuhlmann, and D. A. Paton (2010), Tectonic subsidence history and thermal evolution of the Orange Basin, *Mar. Pet. Geol.*, 27(3), 565–584, doi:10.1016/j.marpetgeo.2009.06.009.
- Höink, T., and A. Lenardic (2008), Three-dimensional mantle convection simulations with a low-viscosity asthenosphere and the relationship between heat flow and the horizontal length scale of convection, *Geophys. Res. Lett.*, 35, L10304, doi:10.1029/2008GL033854.
- Höink, T., and A. Lenardic (2010), Long wavelength convection, Poiseuille-Couette flow in the low-viscosity asthenosphere and the strength of plate margins, *Geophys. J. Int.*, 180(1), 23–33, doi:10.1111/j.1365-246X.2009.04404.x.
- Höink, T., A. M. Jellinek, and A. Lenardic (2011), Viscous coupling at the lithosphere-asthenosphere boundary, *Geochem. Geophys. Geosyst.*, 12, Q0AK02, doi:10.1029/2011GC003698.
- Hoorn, C., et al. (2010), Amazonia through time: Andean uplift, climate change, landscape evolution, and biodiversity, *Science*, 330(6006), 927–931, doi:10.1126/science.1194585.
- Houser, C., G. Masters, P. Shearer, and G. Laske (2008), Shear and compressional velocity models of the mantle from cluster analysis of long-period waveforms, *Geophys. J. Int.*, 174(1), 195–212, doi:10.1111/j.1365-246X.2008.03763.x.
- Husson, L., and Y. Ricard (2004), Stress balance above subduction: Application to the Andes, *Earth Planet. Sci. Lett.*, 222(3–4), 1037–1050, doi:10.1016/j.epsl.2004.03.041.
- Husson, L., C. P. Conrad, and C. Faccenna (2012), Plate motions, Andean orogeny, and volcanism above the South Atlantic convection cell, *Earth Planet. Sci. Lett.*, 317, 126–135, doi:10.1016/j.epsl.2011.11.040.
- Iaffaldano, G. (2012), The strength of large-scale plate boundaries: Constraints from the dynamics of the Philippine Sea plate since ~5Ma, *Earth Planet. Sci. Lett.*, 357–358, 21–30, doi:10.1016/j.epsl.2012.09.018.
- Iaffaldano, G., and H.-P. Bunge (2008), Strong plate coupling along the Nazca-South America convergent margin, *Geology*, 36(6), 443–446, doi:10.1130/G24489A.1.
- Iaffaldano, G., and H.-P. Bunge (2009), Relating rapid plate-motion variations to plate-boundary forces in global coupled models of the mantle/lithosphere system: Effects of topography and friction, *Tectonophysics*, 474(1–2), 393–404, doi:10.1016/j.tecto.2008.10.035.
- Iaffaldano, G., H.-P. Bunge, and T. H. Dixon (2006), Feedback between mountain belt growth and plate convergence, *Geology*, 34(10), 893–896, doi:10.1130/G22661.1.
- Iaffaldano, G., T. Bodin, and M. Sambridge (2012), Reconstructing plate-motion changes in the presence of finite-rotations noise, *Nat. Commun.*, 3, 1048, doi:10.1038/ncomms2051.
- Ismail-Zadeh, A., G. Schubert, I. Tsepelov, and A. Korotkii (2004), Inverse problem of thermal convection: Numerical approach and application to mantle plume restoration, *Phys. Earth Planet. Inter.*, 145(1–4), 99–114, doi:10.1016/j.pepi.2004.03.006.
- Jackson, M., M. Hudec, and K. Hegarty (2005), The great West African Tertiary coastal uplift: Fact or fiction? A perspective from the Angolan divergent margin, *Tectonics*, 24(6), TC6014, doi:10.1029/2005TC001836.
- Jaillard, E. (1994), Kimmeridgian to Paleocene tectonic and geodynamic evolution of the Peruvian (and Ecuadorian) margin, in *Cretaceous Tectonics of the Andes*, edited by J. A. Salfity, pp. 101–167, Earth Evol. Sci., Vieweg, Braunschweig, Germany.
- Jaillard, E., and P. Soler (1996), Cretaceous to early Paleogene tectonic evolution of the northern Central Andes (0–18 degrees S) and its relations to geodynamics, *Tectonophysics*, 259(1–3), 41–53, doi:10.1016/0040-1951(95)00107-7.
- Janssen, M. E., R. A. Stephenson, and S. Cloetingh (1995), Temporal and spatial correlations between changes in plate motions and the evolution of rifted basins in Africa, *Geol. Soc. Am. Bull.*, 107(11), 1317–1332.
- Japsen, P., J. A. Chalmers, P. F. Green, and J. M. Bonow (2012a), Elevated, passive continental margins: Not rift shoulders, but expressions of episodic, post-rift burial and exhumation, *Global Planet. Change*, 90–91, 73–86, doi:10.1016/j.gloplacha.2011.05.004.
- Japsen, P., J. M. Bonow, P. F. Green, P. R. Cobbold, D. Chiossi, R. Lilletveit, L. P. Magnavita, and A. Pedreira (2012b), Episodic burial and exhumation in NE Brazil after opening of the South Atlantic, *Geol. Soc. Am. Bull.*, 124(5–6), 800–816, doi:10.1130/B30515.1.
- Jelsma, H., W. Barnett, S. Richards, and G. Lister (2009), Tectonic setting of kimberlites, *Lithos*, 112, 155–165, doi:10.1016/j.lithos.2009.06.030.
- Jones, A. G. (1982), Observations of the electrical asthenosphere beneath Scandinavia, *Tectonophysics*, 90(1–2), 37–55, doi:10.1016/0040-1951(82)90252-9.
- Karato, S., and H. Jung (1998), Water, partial melting and the origin of the seismic low velocity and high attenuation zone in the upper mantle, *Earth Planet. Sci. Lett.*, 157(3–4), 193–207, doi:10.1016/S0012-821X(98)00034-X.
- Karato, S.-I., and P. Wu (1993), Rheology of the upper mantle: A synthesis, *Science*, 260, 771–778.
- King, L. C. (1955), Pediplanation and isostasy: An example from South Africa, *Q. J. Geol. Soc. London*, 111, 353–359.
- Kounov, A., G. Viola, M. de Wit, and M. Andreoli (2009), Denudation along the Atlantic passive margin: New insights from apatite fission-track analysis on the western coast of South Africa, in *Thermochronological Methods: From Palaeotemperature Constraints to Landscape Evolution Models*, edited by F. Lisker, and B. Ventura, and U. A. Glasmacher, *Geol. Soc. London Spec. Publ.*, 324, 1–20.
- Kustowski, B., G. Ekstrom, and A. M. Dziewonski (2008), Anisotropic shear-wave velocity structure of the Earth's mantle: A global model, *J. Geophys. Res.*, 113, B06306, doi:10.1029/2007JB005169.
- Labails, C., T. H. Torsvik, C. Gaina, and R. M. Cocks (2009), Global plate polygons 2009. SPlates Model (version 2.0), *Tech. Rep. 2009.047*, NGU, Postboks 6315 Sluppen, 7491 Trondheim. [Available at <http://www.ngu.no/en-gb/>]

- Labrosse, S. (2002), Hotspots, mantle plumes and core heat loss, *Earth Planet. Sci. Lett.*, 199(1–2), 147–156, doi:10.1016/S0012-821X(02)00537-X.
- Lamb, S. (2006), Shear stresses on megathrusts: Implications for mountain building behind subduction zones, *J. Geophys. Res.*, 111(B7), B07401, doi:10.1029/2005JB003916.
- Lamb, S., and P. Davis (2003), Cenozoic climate change as a possible cause for the rise of the Andes, *Nature*, 425(6960), 792–797, doi:10.1038/nature02049.
- Lavier, L., M. Steckler, and F. Brigaud (2001), Climatic and tectonic control on the Cenozoic evolution of the West African margin, *Mar. Geol.*, 178(1–4), 63–80, doi:10.1016/S0025-3227(01)00175-X.
- Lekić, V., and B. Romanowicz (2011), Inferring upper-mantle structure by full waveform tomography with the spectral element method, *Geophys. J. Int.*, 185, 799–831, doi:10.1111/j.1365-246X.2011.04969.x.
- Leturmy, P., F. Lucazeau, and F. Brigaud (2003), Dynamic interactions between the Gulf of Guinea passive margin and the Congo River drainage basin: 1. Morphology and mass balance, *J. Geophys. Res.*, 108(B8), 2383, doi:10.1029/2002JB001927.
- Lithgow-Bertelloni, C., and M. A. Richards (1995), Cenozoic plate driving forces, *Geophys. Res. Lett.*, 22(11), 1317–1320, doi:10.1029/95GL01325.
- Lucazeau, F., F. Brigaud, and P. Leturmy (2003), Dynamic interactions between the Gulf of Guinea passive margin and the Congo River drainage basin: 2. Isostasy and uplift, *J. Geophys. Res.*, 108(B8), 2384, doi:10.1029/2002JB001928.
- Lunde, G., K. Aubert, O. Lauritzen, and E. Lorange (1992), Tertiary uplift of the Kwanza Basin in Angola, in *Géologie Africaine: Coll. Géol. Libreville, Recueil des Communications, 6–8 May 1991*, edited by R. Curnelle, pp. 99–117, Elf-Aquitaine, Boussens, France.
- MacGregor, D. S. (2012), Late Cretaceous–Cenozoic sediment and turbidite reservoir supply to South Atlantic margins, in *Conjugate Divergent Margins*, edited by W. U. Mohriak et al., *Geol. Soc. London Spec. Publ.*, 369, 20.
- Manga, C. S. (2008), Stratigraphy, structure and prospectivity of the Southern onshore Douala Basin, Cameroon, Central Africa, in *Cameroon and Neighboring Basins in the Gulf of Guinea (Petroleum Geology Tectonics Geophysics Paleontology and Hydrogeology)*, *Africa Geosci. Rev. Spec. Publ.*, edited by M. J. Ntamak-Nida, G. E. Ekodeck, and M. Guiraud, pp. 13–37, Malakoff, France.
- McMillan, I. (2003), Foraminiferally defined biostratigraphic episodes and sedimentation pattern of the Cretaceous drift succession (Early Barremian to Late Maastrichtian) in seven basins on the South African and southern Namibian continental margin, *S. Afr. J. Sci.*, 99(11–12), 537–576.
- Mitrovica, J. X. (1996), Haskell [1935] revisited, *J. Geophys. Res.*, 101(B1), 555–569, doi:10.1029/95JB03208.
- Mittelstaedt, E., and P. J. Tackley (2006), Plume heat flow is much lower than CMB heat flow, *Earth Planet. Sci. Lett.*, 241(1–2), 202–210, doi:10.1016/j.epsl.2005.10.012.
- Molnar, P., and J. M. Stock (2009), Slowing of India's convergence with Eurasia since 20 Ma and its implications for Tibetan mantle dynamics, *Tectonics*, 28, TC3001, doi:10.1029/2008TC002271.
- Moulin, M., D. Aslanian, and P. Unternehr (2010), A new starting point for the South and Equatorial Atlantic Ocean, *Earth Sci. Rev.*, 98(1–2), 1–37.
- Mpodozis, C., C. Arriagada, M. Basso, P. Roperch, P. Cobbold, and M. Reich (2005), Late Mesozoic to paleogene stratigraphy of the Salar de Atacama Basin, Antofagasta, Northern Chile: Implications for the tectonic evolution of the Central Andes, *Tectonophysics*, 399(1–4), 125–154, doi:10.1016/j.tecto.2004.12.019.
- Müller, R. D., J.-Y. Royer, and L. A. Lawver (1993), Revised plate motions relative to the hotspots from combined Atlantic and Indian Ocean hotspot tracks, *Geology*, 21(3), 275, doi:10.1130/0091-7613(1993)021<0275:RPMRTT>2.3.CO;2.
- Müller, R. D., W. R. Roest, J. Y. Royer, L. M. Gahagan, and J. G. Sclater (1997), Digital isochrons of the world's ocean floor, *J. Geophys. Res.*, 102, 3211–3214.
- Müller, R. D., J.-Y. Royer, S. C. Cande, W. R. Roest, and S. Maschenkov (1999), New constraints on the late Cretaceous/Tertiary plate tectonic evolution of the Caribbean, in *Caribbean Basins, Sedimentary Basins of the World*, vol. 4, edited by P. Mann, pp. 33–59, Elsevier, Amsterdam, doi:10.1016/S1874-5997(99)80036-7.
- Müller, R. D., M. Sdrolias, C. Gaina, and W. R. Roest (2008), Age, spreading rates, and spreading asymmetry of the world's ocean crust, *Geochem. Geophys. Geosyst.*, 9(4), Q04006, doi:10.1029/2007GC001743.
- Nerlich, R., S. R. Clark, and H.-P. Bunge (2013), The Scotia Sea gateway: No outlet for Pacific mantle, *Tectonophysics*, 604, 41–50, doi:10.1016/j.tecto.2012.08.023.
- Norabuena, E. O., T. H. Dixon, S. Stein, and C. G. A. Harrison (1999), Decelerating Nazca–South America and Nazca–Pacific Plate motions, *Geophys. Res. Lett.*, 26(22), 3405–3408, doi:10.1029/1999GL005394.
- Nürnberg, D., and R. D. Müller (1991), The tectonic evolution of the South Atlantic from Late Jurassic to present, *Tectonophysics*, 191(1), 21–53.
- Nyblade, A. A., and S. W. Robinson (1994), The African superswell, *Geophys. Res. Lett.*, 21(9), 765–768.
- O'Connor, J. M., W. Jokat, A. P. le Roex, C. Class, J. R. Wijbrans, S. Kessling, K. F. Kuiper, and O. Nebel (2012), Hotspot trails in the South Atlantic controlled by plume and plate tectonic processes, *Nat. Geosci.*, 5(10), 735–738, doi:10.1038/NGEO1583.
- Oncken, O., G. Chong, G. Franz, P. Giese, H.-J. Götze, V. A. Ramos, M. R. Strecker, and P. Wigger (2006), *The Andes: Active Subduction Orogeny*, Frontiers in Earth Sciences, Springer, Berlin Heidelberg, New York.
- O'Neill, C., D. Müller, and B. Steinberger (2005), On the uncertainties in hot spot reconstructions and the significance of moving hot spot reference frames, *Geochem. Geophys. Geosyst.*, 6(4), Q04003, doi:10.1029/2004GC000784.
- Orts, S., and V. A. Ramos (2006), *Evidence of Middle to Late Cretaceous Compressive Deformation in the High Andes of Mendoza, Argentina*, 65, Backbone of the Americas, Abstracts With Programs, Patagonia to Alaska, GSA Special Meetings-AGA Publicaciones Especiales No. 5, Mendoza.
- Panning, M., and B. Romanowicz (2006), A three-dimensional radially anisotropic model of shear velocity in the whole mantle, *Geophys. J. Int.*, 167(1), 361–379, doi:10.1111/j.1365-246X.2006.03100.x.
- Partridge, T. C., and R. R. Maud (1987), Geomorphic evolution of Southern Africa since the Mesozoic, *S. Afr. J. Geol.*, 90(2), 179–208.
- Paton, D. A., D. van der Spuy, R. di Primio, and B. Horsfield (2008), Tectonically induced adjustment of passive-margin accommodation space; influence on the hydrocarbon potential of the Orange Basin, South Africa, *AAPG Bull.*, 92(5), 589–609, doi:10.1306/12280707023.
- Paulson, A., and M. A. Richards (2009), On the resolution of radial viscosity structure in modelling long-wavelength postglacial rebound data, *Geophys. J. Int.*, 179(3), 1516–1526, doi:10.1111/j.1365-246X.2009.04362.x.
- Phipps Morgan, J., and W. H. F. Smith (1992), Flattening of the sea-floor depth age curve as a response to asthenospheric flow, *Nature*, 359(6395), 524–527, doi:10.1038/359524a0.
- Phipps Morgan, J., W. J. Morgan, Y.-S. Zhang, and W. H. F. Smith (1995), Observational hints for a plume-fed, suboceanic asthenosphere and its role in mantle convection, *J. Geophys. Res.*, 100(B7), 12,753–12,767.

- Piazzoni, A. S., G. Steinle-Neumann, H. P. Bunge, and D. Dolejs (2007), A mineralogical model for density and elasticity of the Earth's mantle, *Geochem. Geophys. Geosyst.*, 8, Q11010, doi:10.1029/2007GC001697.
- Raab, M., R. Brown, K. Gallagher, A. Carter, and K. Weber (2002), Late Cretaceous reactivation of major crustal shear zones in northern Namibia: Constraints from apatite fission track analysis, *Tectonophysics*, 349(1–4), 75–92, doi:10.1016/S0040-1951(02)00047-1.
- Raab, M., R. Brown, K. Gallagher, K. Weber, and A. Gleadow (2005), Denudational and thermal history of the Early Cretaceous Brandberg and Okenyenya igneous complexes on Namibia's Atlantic passive margin, *Tectonics*, 24(3), TC3006, doi:10.1029/2004TC001688.
- Rasmussen, E. (1996), Structural evolution and sequence formation offshore South Gabon during the Tertiary, *Tectonophysics*, 266(1–4), 509–523, doi:10.1016/S0040-1951(96)00236-3.
- Richards, M. A., and B. H. Hager (1984), Geoid anomalies in a dynamic Earth, *J. Geophys. Res.*, 89(B7), 5987–6002, doi:10.1029/JB089iB07p05987.
- Rickers, F., A. Fichtner, and J. Trampert (2013), The Iceland-Jan Mayen plume system and its impact on mantle dynamics in the North Atlantic region: Evidence from full-waveform inversion, *Earth Planet. Sci. Lett.*, 367, 39–51, doi:10.1016/j.epsl.2013.02.022.
- Ritsema, J., A. Deuss, H. J. van Heijst, and J. H. Woodhouse (2011), S4ORTS: A degree-40 shear-velocity model for the mantle from new Rayleigh wave dispersion, teleseismic traveltimes and normal-mode splitting function measurements, *Geophys. J. Int.*, 3(184), 1223–1236.
- Romanowicz, B., and Y. C. Gung (2002), Superplumes from the core-mantle boundary to the lithosphere: Implications for heat flux, *Science*, 296(5567), 513–516, doi:10.1126/science.1069404.
- Rousse, S., S. Gilder, D. Farber, B. McNulty, P. Patriat, V. Torres, and T. Sempere (2003), Paleomagnetic tracking of mountain building in the Peruvian Andes since 10 Ma, *Tectonics*, 22(5), 1048, doi:10.1029/2003TC001508.
- Schaber, K., H.-P. Bunge, B. S. A. Schubert, R. Malservisi, and A. Horbach (2009), Stability of the rotation axis in high-resolution mantle circulation models: Weak polar wander despite strong core heating, *Geochem. Geophys. Geosyst.*, 10, Q11W04, doi:10.1029/2009GC002541.
- Schildgen, T. F., K. V. Hodges, K. X. Whipple, P. W. Reiners, and M. S. Pringle (2007), Uplift of the western margin of the Andean Plateau revealed from canyon incision history, southern Peru, *Geology*, 35(6), 523–526, doi:10.1130/G23532A.1.
- Schubert, B. S. A., H.-P. Bunge, and J. Ritsema (2009a), Tomographic filtering of high-resolution mantle circulation models: Can seismic heterogeneity be explained by temperature alone?, *Geochem. Geophys. Geosyst.*, 10(5), Q05W03, doi:10.1029/2009GC002401.
- Schubert, B. S. A., H.-P. Bunge, G. Steinle-Neumann, C. Moder, and J. Oeser (2009b), Thermal versus elastic heterogeneity in high-resolution mantle circulation models with pyrolite composition: High plume excess temperatures in the lowermost mantle, *Geochem. Geophys. Geosyst.*, 10(1), Q01W01, doi:10.1029/2008GC002235.
- Schubert, B. S. A., C. Zanolli, and G. Nolet (2012), Synthetic seismograms for a synthetic Earth: Long-period P- and S-wave traveltime variations can be explained by temperature alone, *Geophys. J. Int.*, 188(3), 1393–1412, doi:10.1111/j.1365-246X.2011.05333.x.
- Sebrier, M., A. Lavenu, M. Fornari, and J.-P. Soulas (1988), Tectonics and uplift in the Central Andes (Peru, Bolivia and Northern Chile) from Eocene to Present, *Géodynamique*, 3, 85–106.
- Sempere, T., G. Herail, J. Oller, and M. Bonhomme (1990), Late Oligocene-early Miocene major tectonic crisis and related basins in Bolivia, *Geology*, 18(10), 946–949, doi:10.1130/0091-7613(1990)018<0946:LOEMMT>2.3.CO;2.
- Sempere, T., L. Marshall, S. Rivano, and E. Godoy (1994), Late Oligocene-early Miocene compressional tectosedimentary episode and associated land-mammal faunas in the Andes of central Chile and Adjacent Argentina (32–37°S), *Tectonophysics*, 229(3–4), 251–264, doi:10.1016/0040-1951(94)90032-9.
- Sempere, T., R. Butler, D. Richards, L. Marshall, W. Sharp, and C. Swisher (1997), Stratigraphy and chronology of Upper Cretaceous lower Paleogene strata in Bolivia and northwest Argentina, *Geol. Soc. Am. Bull.*, 109(6), 709–727, doi:10.1130/0016-7606(1997)109<0709:SACOU>2.3.CO;2.
- Sempere, T., A. Folguera, and M. Gerbault (2008), New insights into Andean evolution: An introduction to contributions from the 6th ISAG symposium (Barcelona, 2005), *Tectonophysics*, 459(1–4), 1–13, doi:10.1016/j.tecto.2008.03.011.
- Seno, T. (2009), Determination of the pore fluid pressure ratio at seismogenic megathrusts in subduction zones: Implications for strength of asperities and Andean-type mountain building, *J. Geophys. Res.*, 114, B05405, doi:10.1029/2008JB005889.
- Seranne, M., and Z. Anka (2005), South Atlantic continental margins of Africa: A comparison of the tectonic vs climate interplay on the evolution of equatorial West Africa and SW Africa margins, *J. Afr. Earth. Sci.*, 43(1–3), 283–300, doi:10.1016/j.jafrearsci.2005.07.010.
- Seton, M., et al. (2012), Global continental and ocean basin reconstructions since 200 Ma, *Earth Sci. Rev.*, 113(3–4), 212–270, doi:10.1016/j.earscirev.2012.03.002.
- Shapiro, N. M., and M. H. Ritzwoller (2002), Monte-Carlo inversion for a global shear-velocity model of the crust and upper mantle, *Geophys. J. Int.*, 151(1), 88–105, doi:10.1046/j.1365-246X.2002.01742.x.
- Shaw, P. R., and S. C. Cande (1990), High-resolution inversion for South Atlantic plate kinematics using joint altimeter and magnetic anomaly data, *J. Geophys. Res.*, 95(B3), 2625–2644.
- Silver, P., R. Russo, and C. Lithgow-Bertelloni (1998), Coupling of South American and African plate motion and plate deformation, *Science*, 279(5347), 60–63, doi:10.1126/science.279.5347.60.
- Simmons, N. A., A. M. Forte, and S. P. Grand (2006), Constraining mantle flow with seismic and geodynamic data: A joint approach, *Earth Planet. Sci. Lett.*, 246(1–2), 109–124, doi:10.1016/j.epsl.2006.04.003.
- Simmons, N. A., A. M. Forte, and S. P. Grand (2007), Thermochemical structure and dynamics of the African superplume, *Geophys. Res. Lett.*, 34(L02301), doi:10.1029/2006GL028009.
- Spetzler, J., J. Trampert, and R. Snieder (2002), The effect of scattering in surface wave tomography, *Geophys. J. Int.*, 149(3), 755–767, doi:10.1046/j.1365-246X.2002.01683.x.
- Stanley, J. R., R. M. Flowers, and D. R. Bell (2013), Kimberlite (U-Th)/He dating links surface erosion with lithospheric heating, thinning, and metasomatism in the southern African plateau, *Geology*, 41(12), 1243–1246, doi:10.1130/g34797.1.
- Steinberger, B., and T. H. Torsvik (2008), Absolute plate motions and true polar wander in the absence of hotspot tracks, *Nature*, 452(7187), 620–623, doi:10.1038/nature06824.
- Steinmann, G., C. I. Lisson, A. Sieberg, and R. Stappenbeck (1929), *Geologie von Peru*, Winters Universitätsbuchhandlung, Heidelberg.
- Suppe, J. (2007), Absolute fault and crustal strength from wedge tapers, *Geology*, 35(12), 1127–1130, doi:10.1130/G24053A.1.
- Tackley, P. J. (1996), On the ability of phase transitions and viscosity layering to induce long wavelength heterogeneity in the mantle, *Geophys. Res. Lett.*, 23(15), 1985–1988, doi:10.1029/96GL01980.
- Thouret, J.-C., G. Woerner, Y. Gunnell, B. Singer, X. Zhang, and T. Souriot (2007), Geochronologic and stratigraphic constraints on canyon incision and Miocene uplift of the Central Andes in Peru, *Earth Planet. Sci. Lett.*, 263(3–4), 151–166, doi:10.1016/j.epsl.2007.07.023.
- Torsvik, T. H., S. Rousse, C. Labails, and M. A. Smethurst (2009), A new scheme for the opening of the South Atlantic Ocean and the dissection of an Aptian salt basin, *Geophys. J. Int.*, 177(3), 1315–1333, doi:10.1111/j.1365-246X.2009.04137.x.

- Turner, J. P., P. F. Green, S. P. Holford, and S. R. Lawrence (2008), Thermal history of the Rio Muni (West Africa)-NE Brazil margins during continental breakup, *3–4*, 270, 354–367, doi:10.1016/j.epsl.2008.04.002.
- Walford, H., and N. White (2005), Constraining uplift and denudation of West African continental margin by inversion of stacking velocity data, *J. Geophys. Res.*, *110*, B04403, doi:10.1029/2003JB002893.
- Walgenwitz, F. R., J. P. Richert, and P. Charpentier (1992), Southwest African plate margin: Thermal history and geodynamical implications, in *Geologic Evolution of Atlantic Continental Rises*, edited by C. W. Poag and P. C. de Graciansky, pp. 20–45, Van Nostrand Reinhold, New York.
- Wang, Z., and F. A. Dahlen (1995), Validity of surface-wave ray theory on a laterally heterogeneous Earth, *Geophys. J. Int.*, *123*(3), 757–773, doi:10.1111/j.1365-246X.1995.tb06888.x.
- Weertman, J., and J. R. Weertman (1975), High-temperature creep of rock and mantle viscosity, *Annu. Rev. Earth Planet. Sci.*, *3*, 293–315, doi:10.1146/annurev.ea.03.050175.001453.
- Wiens, D. A., and S. Stein (1985), Implications of oceanic intraplate seismicity for plate stresses, driving forces and rheology, *Tectonophysics*, *116*(1–2), 143–162, doi:10.1016/0040-1951(85)90227-6.
- Winterbourne, J., A. Crosby, and N. White (2009), Depth, age and dynamic topography of oceanic lithosphere beneath heavily sedimented Atlantic margins, *Earth Planet. Sci. Lett.*, *287*(1–2), 137–151, doi:10.1016/j.epsl.2009.08.019.
- Zhong, S., and W. Leng (2006), Dynamics of mantle plumes and their implications for the heat budget and composition of the mantle, *Geochim. Cosmochim. Acta*, *70*(18), SA749, doi:10.1016/j.gca.2006.06.1351.
- Zhou, Y., F. A. Dahlen, G. Nolet, and G. Laske (2005), Finite-frequency effects in global surface-wave tomography, *Geophys. J. Int.*, *163*, 1087–1111, doi:10.1111/j.1365-246X.2005.02780.x.

Chapter 4

On retrodictions of global mantle flow with assimilated surface velocities

This chapter was published in the Journal “Geophysical Research Letters” in 2015. It explores the possibility of geodynamic retrodictions in the presence or absence of knowledge of the past history of surface motions.



RESEARCH LETTER

10.1002/2015GL066001

Key Points:

- Long-term retrodictions of mantle convection are hindered by chaotic drift
- Reconstructions of past plate motion provide fundamental information about mantle flow in the past
- Assimilation of past plate motion data greatly improves long-term retrodictions of mantle convection

Correspondence to:

L. Colli,
colli@geophysik.uni-muenchen.de

Citation:

Colli, L., H.-P. Bunge, and B. S. A. Schuberth (2015), On retrodictions of global mantle flow with assimilated surface velocities, *Geophys. Res. Lett.*, 42, 8341–8348, doi:10.1002/2015GL066001.

Received 31 AUG 2015

Accepted 25 SEP 2015

Accepted article online 5 OCT 2015

Published online 24 OCT 2015

On retrodictions of global mantle flow with assimilated surface velocities

Lorenzo Colli¹, Hans-Peter Bunge¹, and Bernhard S. A. Schuberth¹¹Department of Earth and Environmental Sciences, University of Munich, Munich, Germany

Abstract Modeling past states of Earth's mantle and relating them to geologic observations such as continental-scale uplift and subsidence is an effective method for testing mantle convection models. However, mantle convection is chaotic and two identical mantle models initialized with slightly different temperature fields diverge exponentially in time until they become uncorrelated, thus limiting retrodictions (i.e., reconstructions of past states of Earth's mantle obtained using present information) to the recent past. We show with 3-D spherical mantle convection models that retrodictions of mantle flow can be extended significantly if knowledge of the surface velocity field is available. Assimilating surface velocities produces in some cases negative Lyapunov times (i.e., *e*-folding times), implying that even a severely perturbed initial condition may evolve toward the reference state. A history of the surface velocity field for Earth can be obtained from past plate motion reconstructions for time periods of a mantle overturn, suggesting that mantle flow can be reconstructed over comparable times.

1. Introduction

Reconstructing the heterogeneity state of Earth's mantle in the past and predicting its future evolution are major goals in global geodynamics. From a mathematical perspective this is an initial value and boundary value Cauchy problem, where the governing equations are the conservation of mass, momentum, and energy according to the formalism of continuum mechanics (see *Jarvis and McKenzie* [1980] for a detailed derivation). An initial condition for the present day can be estimated from seismically derived global tomographic models for Earth's mantle [e.g., *Grand et al.*, 1997; *Ritsema et al.*, 2011] together with thermodynamically self-consistent models of mantle mineralogy [*Piazzoni et al.*, 2007; *Stixrude and Lithgow-Bertelloni*, 2011]. It is thus possible to initialize a model Earth and evolve it into the future in accord with the governing equations [e.g., *Trubitsyn et al.*, 2008; *Yoshida and Santosh*, 2011]. Both initial condition and model parameters, however, are not well known. The average radial viscosity profile of the bulk mantle, for example, is still affected by order-of-magnitude uncertainties [e.g., *Mitrova and Forte*, 2004; *Paulson and Richards*, 2009]. Plate boundaries are even more problematic: they are characterized by a complex visco-elasto-plastic rheology and are affected by surface processes such as sedimentation, erosion, and changes in climate [*Iaffaldano et al.*, 2011; *Iaffaldano*, 2012]. Different assumptions and approximations lead to vastly different predictions for the future of Earth. Unfortunately, as mantle convection develops over timescales of millions of years, these predictions and the assumptions they are based upon cannot be tested. Mantle convection models can be explicitly tested in time only if retrodictions of past evolution of Earth's mantle are checked against the geological record. In this case we lack suitable initial conditions for the past. But a number of techniques—from sequential data assimilation [*Bunge et al.*, 1998], to backward advection [*Steinberger and O'Connell*, 1997], and to variational methods [*Bunge et al.*, 2003; *Ismail-Zadeh et al.*, 2004]—have been proposed to overcome this impasse and to obtain estimates of past mantle heterogeneity structure.

A further complexity arises from the chaotic nature of convection at the vigorous, high Rayleigh number flow regime that characterizes Earth's mantle [*Stewart and Turcotte*, 1989; *Solheim and Peltier*, 1990]. Simply put, two arbitrarily close initial states will diverge exponentially in time until they become uncorrelated, thus limiting their predictability. Given the uncertainty with which we know the present-day thermodynamic state of Earth's mantle, *Bello et al.* [2014] estimated that the limit of predictability for mantle convection models is around 100Ma at best.

In their analysis, *Bello et al.* [2014] assumed that the only information available to set up a predictive model is the approximate initial state of the true model, thus exploring the predictability of mantle flow strictly in

its dependence upon the initial condition. This is perfectly valid for predictions of future mantle states. When reconstructing the recent geodynamic evolution of Earth, however, there is additional information available in the form of plate motion histories, as inferred from paleomagnetic observations [Gordon and Jurdy, 1986]. A *retrodiction* can thus be made, at least in principle, by assimilating the surface velocity field of Earth and comparing the evolving mantle state against independent observations from the geological record, such as continental-scale uplift and subsidence. Notice that this differs from a hindcasting in that real data is compared with model results that are obtained during the assimilation period. The process of data assimilation could not only mitigate the inadequacy of our models of plate boundary forces but possibly also influence our ability to restore past states of mantle flow by reducing the chaotic drift. In other words, injecting in global mantle convection models information about the evolving surface velocity field, and hence transferring one flow state into another, may keep the evolved states closer together, potentially locking them into very similar states.

While early reconstructions of past plate motion restricted themselves to the Cenozoic [Gordon and Jurdy, 1986] or to portions of Earth's surface [Engebretson *et al.*, 1984], the past 30 years have seen tremendous progress in the construction of global plate motion models spanning the Cenozoic and mid-Mesozoic history of Earth. Such models provide sets of plate boundaries and Euler rotation vectors for each plate, initially at discrete intervals (plate stages) [Lithgow-Bertelloni and Richards, 1998] and more recently continuously in time [Gurnis *et al.*, 2012; Seton *et al.*, 2012]. Past plate motion models are now common, and some have been extended back into the Paleozoic [Zhang *et al.*, 2010; Domeier and Torsvik, 2014], albeit with larger uncertainties, since well constrained kinematic reconstructions rely on magnetic lineaments in the oceanic crust and most of it is younger than 150Ma.

In this paper we build on the innovative work of Bello *et al.* [2014] and explore to what extent, if any, knowledge of past surface velocities may help to counteract the inherent temporal divergence of unconstrained mantle convection models and to extend global mantle flow retrodictions beyond the limits imposed by chaos.

2. Method

The study of Bello *et al.* [2014] applied the twin experiment method [Lorenz, 1965]: two models with very close initial conditions are allowed to evolve freely. By monitoring their temporal divergence, it is possible to determine the largest Lyapunov exponent λ —that is, the mean exponential growth rate of the total discrepancy [Benettin *et al.*, 1980]. A statistically steady state solution for the temperature field serves to initialize the reference twin case, while the perturbed case adds a small random perturbation to the same steady state solution. The perturbation consists of a pointwise error, uncorrelated in space and up to 1% of the average temperature in amplitude. The discrepancy between the two cases can be quantified as

$$E(t) = \int_{V_{\Omega}} \frac{|T_p(\mathbf{x}, t) - T(\mathbf{x}, t)|}{T(\mathbf{x}, t)} \frac{dV}{V_{\Omega}}, \quad (1)$$

where $T(\mathbf{x}, t)$ and $T_p(\mathbf{x}, t)$ are the temperature fields of the reference and perturbed twin, respectively. The discrepancy is thus expected to grow exponentially as $E(t) \propto \exp(t/\tau)$, where $\tau = 1/\lambda$ is the Lyapunov time. We follow the same approach, with an additional scenario: we initialize a third convection model having the same initial state as the perturbed twin, but we constrain its temporal evolution by assimilating the surface velocities of the reference twin.

Our three-dimensional (3-D) time-dependent solutions for incompressible mantle convection are computed using the code Terra [Bunge *et al.*, 1996, 1997]. For the sake of simplicity, we consider convection models having three different radial viscosity profiles: an isoviscous mantle, a two-layer case with an increase in viscosity by a factor of 40 between 800 and 1000 km depth, and a three-layer case with a 100 km thick lithosphere 80 times more viscous than the upper mantle in addition to the stiffer lower mantle. All model runs are characterized by an internal-heating Rayleigh number of 2.4×10^7 based on their volume-averaged viscosity, and the relevant model parameters are listed in Table 1. To ensure adequate numerical resolution, the computational domain is discretized with a mesh, derived from the regular icosahedron, using more than 80 million finite elements. For this mesh size, the horizontal grid point resolution is 30 km at the surface and decreases to half that value at the core-mantle boundary, while the radial grid spacing is 25 km throughout the mantle. The majority of our calculations was done on a local cluster dedicated to large-scale geophysical modeling [Oeser *et al.*, 2006], with additional simulations performed on the GCS Supercomputer SuperMUC at Leibniz Supercomputing Centre (LRZ, www.lrz.de).

Table 1. Model Parameters Employed in This Study

Parameter	Value	Units
Surface temperature	300	K
Internal heating rate	2.5×10^{-12}	Wkg^{-1}
Bottom heating rate ^a	6.6×10^{-3}	Wm^{-2}
Inner radius	3480	km
Outer radius	6370	km
Density	4500	kg
Thermal expansivity	3×10^{-5}	K^{-1}
Thermal conductivity	2.4	$\text{Wm}^{-1} \text{K}^{-1}$
Specific heat capacity	1000	$\text{Jkg}^{-1} \text{K}^{-1}$
Reference viscosity	10^{23}	Pas

^aFor models partially heated from below. Time-averaged value.

3. Results

3.1. Isoviscous Models

Figure 1 shows the results of two model runs for the isoviscous case. The first run is heated entirely from within. The second is heated partially from below. For both heating modes the perturbed twin experiment that is left to convect unconstrained diverges quickly, the Lyapunov time being around 50Ma. The discrepancy grows exponentially up to a saturation value of about 8×10^{-2} , roughly 10 times the initial perturbation, corresponding to the maximum decorrelation level for this model. Note that the perturbed twin, once all memory of the initial state is lost, is merely a different realization of the same physical system of the reference model. The characteristic temperatures of upwellings, downwellings, and ambient mantle are the same. So are their characteristic dimensions, shapes, and spacings. They are thus statistically similar, and their distance cannot grow indefinitely large.

In contrast, the twin experiment with assimilated surface velocities does not diverge. Its error actually decreases to a negligibly small value within a few transit times. We see from the inset in Figure 1 that the assimilated surface velocities is beneficial not only for regions characterized by cold downwellings. Instead, the assimilation reduces the error throughout the mantle for hot and cold regions alike.

3.2. Layered Models

Models with a two-layered viscosity profile are characterized by a distinctive change in the wavelength of temperature anomalies between the two layers. Cold downwellings cannot readily enter the more viscous lower layer; their sinking velocity in the lower layer decreases, and they thicken. Conversely, hot upwellings rise faster once in the upper layer and they become thinner. Figure 2 shows our results for this model. The discrepancy grows in two distinct phases characterized by different Lyapunov times. This is due to the

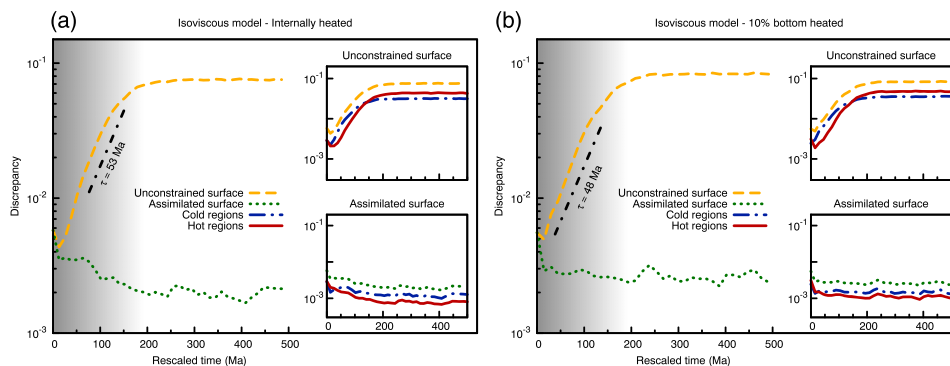


Figure 1. Evolution of the discrepancy in time for isoviscous mantle convection models. (a) Purely internally heated and (b) 10% bottom heated. Dash-dotted black lines and associated labels show the best fitting Lyapunov times. Insets show the contribution of hot and cold regions to the total discrepancy. Surface velocities for the real Earth are known only for a limited time and with increasing uncertainty, as represented by the area shaded in gray.

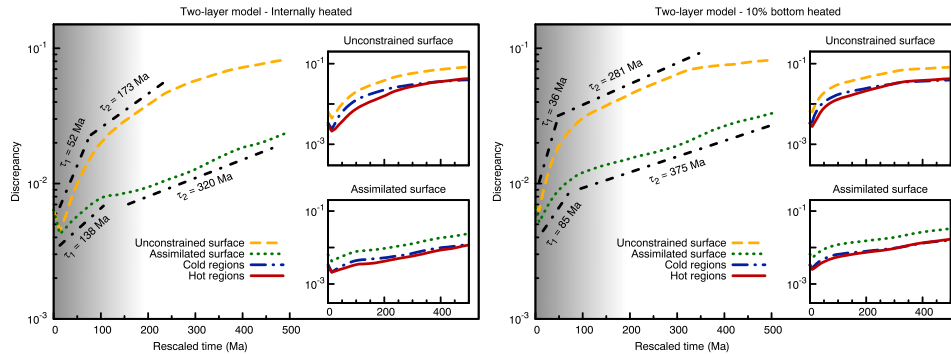


Figure 2. Same as Figure 1 but for mantle convection models characterized by a two-layer radial viscosity profile, the upper part of the mantle being 40 times less viscous than its lower part.

different length scales and timescales of convection in the two layers. All experiments diverge. However, when assimilating the surface velocities the error increases at a much smaller rate, as shown by the increase of all Lyapunov times.

Adding a strong lithosphere causes the planform to shift toward a longer-wavelength convective pattern, the distance between downwellings being now increased due to the stiffer lithosphere. Figure 3 shows for this case that the perturbed initial condition is driven toward the reference solution when surface velocities are assimilated. The convergence is slower than in the isoviscous case, and it takes some hundred million years for the effect of data assimilation to be fully exploited.

The efficiency of surface velocity assimilation in locking two convective states together is seen in Figure 4. Here we show 3-D views of the temperature distribution for the three-layer models with 10% bottom heating after 450Ma of convection. The temperature field of the twin experiment characterized by an unconstrained surface velocity has an error of 0.074 (see Figure 3) and is noticeably different from the reference calculation. The twin experiment with assimilated surface velocities, instead, has an error of 0.01, and the two temperature fields are nearly indistinguishable.

3.3. Long-Wavelength Perturbation

Our imperfect knowledge of the present-day heterogeneity state of the mantle comes from the limited resolution of seismic tomography [Schuberth *et al.*, 2009a, 2009b; Bull *et al.*, 2010]. Indeed, tomographic models of Earth correlate well at long wavelengths, but their similarity decreases rapidly at shorter wavelengths [Becker and Boschi, 2002; Debayle and Ricard, 2012]. To account for this, we consider an extra scenario for each model, where the perturbed initial condition is generated by expanding the reference temperature field in spherical harmonics and retaining only the coefficients of order and degree 20 or less, corresponding to features larger than about 1000 km at the surface. This perturbation retains the large-scale component of the flow but

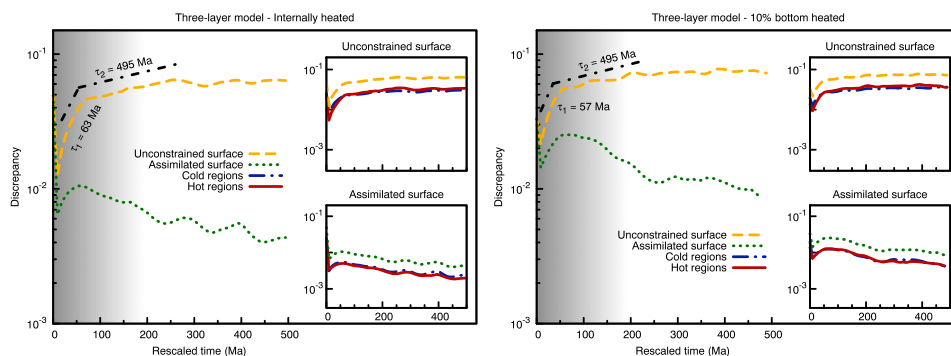


Figure 3. Same as Figure 1 but for mantle convection models characterized by a stiff lithosphere and lower mantle separated by a weak upper mantle.

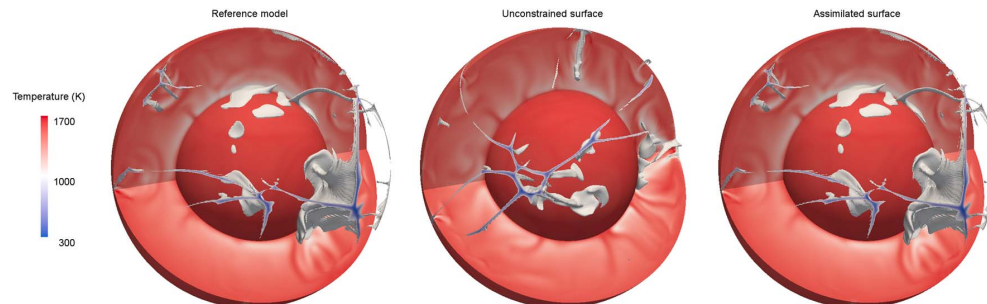


Figure 4. Three-dimensional view of the temperature field of the three-layer model with 10% bottom heating at 450Ma. The uppermost 200 km have been removed to allow views into the mantle interior. Isosurfaces of temperature are displayed for 1000°C. (left) Reference run. (middle) Twin experiment evolved with an unconstrained surface velocity field. (right) Twin experiment evolved with the assimilation of surface velocities from the reference run. The thermal fields of reference run (Figure 4, left) and twin with assimilated surface velocities (Figure 4, right) are nearly indistinguishable.

misses all its details. The results are summarized in Figure 5. In the case of the two-layer model the initial error is so large that assimilating surface velocities only prevents the error from growing. For the other two models, instead, the error decreases steadily to the same very low saturation value found before.

4. Discussion

Reconstructions of past mantle flow are needed in order to test mantle convection models. To this end an intrinsic complexity arises from the chaotic nature of mantle convection at the high Rayleigh number regime appropriate for Earth: small differences in the initial condition between two otherwise identical Earth models grow exponentially if both models are evolved unconstrained, thus preventing long-term predictability. *Bello et al.* [2014] estimated that the initial condition must be known with an accuracy of better than 0.5% in order to model 450Ma of convection history without reaching complete decorrelation. Our analysis suggests that when making a retrodiction, the problem can be overcome in part by sequential assimilation of surface velocities from the reference model: the assimilated information reduces the error growth rate in the perturbed twin and drives its model state closer to the reference state over the course of the assimilation period.

Bello et al. [2014] used a small pointwise random error in order to perturb the reference state. The approach is mathematically convenient for computing the maximum Lyapunov exponent, as it guarantees that some error is introduced in every direction of the space of possible states. However, the small white noise error so introduced is a poor representation of the uncertainties affecting our knowledge of mantle heterogeneity, being uniform in frequency and small in amplitude. It is also a poor representation for thermal heterogeneity in mantle convection models, where very small wavelength anomalies such as those generated by the highest-frequency part of the white noise perturbation are damped quickly by thermal diffusion, as can be seen by the decrease of the error in the first few million years of evolution even for the unconstrained twin, both in our models and in those of *Bello et al.* [2014]. The introduction of a long-wavelength perturbation requires larger assimilation periods. But the assimilation is sufficient to drive the perturbed model toward the reference scenario, at least in the isoviscous and three-layer models.

Other Earth science branches, such as oceanography, meteorology, and core dynamics, employ sequential assimilation techniques as well, being concerned with the chaotic circulation in the oceans, atmosphere, and core. Sequential assimilation, often in the form a Kalman filter [*Kalman*, 1960] that combines a suitably weighted average of measurements and state estimates, allows these disciplines to enhance model predictions substantially [*Wunsch*, 1996; *Talagrand*, 1997; *Fournier et al.*, 2013].

To this end, we note that our analysis relies on a perfect knowledge of the surface velocity field over the entire assimilation period, analogous to Kalman filtering with a gain of 1. Put differently, we assume the assimilated surface velocities from the reference twin to be available without measurement error. In reality our knowledge of past plate motions is not perfect. It has been shown that one may reduce measurement noise and improve the temporal resolution of relative plate motions via Bayesian analysis [*Iaffaldano et al.*, 2012]. Further assumptions, such as the choice of a reference frame, contribute to uncertainty in past plate motion models,

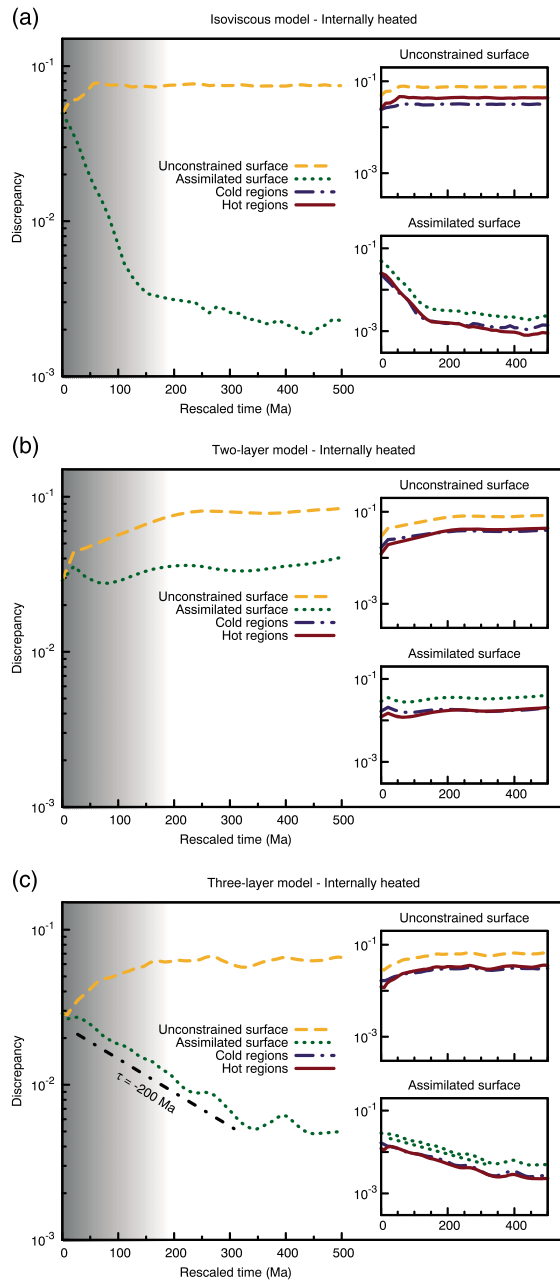


Figure 5. Temporal evolution of the discrepancy for cases where the initial perturbation is generated via a truncation of spherical harmonic expansion at degree 20 instead of a random pointwise error; see text. Assimilating surface velocities significantly reduce the error growth.

especially as one goes further back in time [Shephard *et al.*, 2012]. This would have to be accounted for in future studies.

We find that several hundred million years of plate motion history are necessary to overcome initial condition errors through sequential assimilation. The need for long assimilation periods was noted already by Bunge *et al.* [1998] and recently by Davies *et al.* [2012], when they sequentially assimilated 350Ma of plate motion history to investigate the nature of lower mantle heterogeneity. The limitation arises from the sequential character of the assimilation: each observation is used only once and influences the model state only at later times. The more sophisticated variational assimilation, instead, optimizes the whole time series of model states with respect to the data available over all the assimilation period. Variational assimilation is implemented using the adjoint method, an iterative method based on the combination of a forward and an adjoint mantle convection calculation, both of which are in principle affected by chaotic drift. Vynnytska and Bunge [2014] have shown that knowledge of the surface motion history is necessary to assure convergence of the adjoint approach in mantle convection models. Under this condition Horbach *et al.* [2014] find that the reconstructed evolution has a small null space. In both cases the authors relate their results to a theorem by Serrin [1959], which states that the evolution of a viscous fluid bounded by finitely many rigid surfaces is uniquely determined by its boundary condition.

5. Conclusion

We have employed the twin experiment method to study long-term retrodictions of mantle convection under the assumption that the history of surface motions is known. We find that the assimilation of surface velocities prevents the chaotic long-term drift of unconstrained mantle convection. Past states of mantle flow can thus be reconstructed for periods comparable to the available time span of past plate motion models.

Acknowledgments

This work was funded by the German Research Foundation (DFG) within the priority program SPP 1375-SAMPLE. The authors gratefully acknowledge the Gauss Centre for Supercomputing e.V. (www.gauss-centre.eu) for funding this project by providing computing time on the GCS Supercomputer SuperMUC at Leibniz Supercomputing Centre (LRZ, www.lrz.de). The authors would like to thank the Editor and the anonymous reviewers for the efficient and constructive reviewing process. All data and methods necessary to understand and replicate the present work are reported in the manuscript.

References

- Becker, T. W., and L. Boschi (2002), A comparison of tomographic and geodynamic mantle models, *Geochem. Geophys. Geosyst.*, 3(1), doi:10.1029/2001GC000168.
- Bello, L., N. Coltice, T. Rolf, and P. J. Tackley (2014), On the predictability limit of convection models of the Earth's mantle, *Geochem. Geophys. Geosyst.*, 15(6), 2319–2328, doi:10.1002/2014GC005254.
- Benettin, G., L. Galgani, A. Giorgilli, and J. M. Strelcyn (1980), Lyapunov characteristic exponents for smooth dynamical systems and for Hamiltonian systems; A method for computing all of them. Part 1: Theory, *Meccanica*, 15(1), 9–20, doi:10.1007/BF02128236.
- Bull, A. L., A. K. McNamara, T. W. Becker, and J. Ritsema (2010), Global scale models of the mantle flow field predicted by synthetic tomography models, *Phys. Earth Planet. Inter.*, 182(3–4), 129–138, doi:10.1016/j.pepi.2010.03.004.
- Bunge, H.-P., M. A. Richards, and J. R. Baumgardner (1996), Effect of depth-dependent viscosity on the planform of mantle convection, *Nature*, 379(6564), 436–438, doi:10.1038/379436a0.
- Bunge, H.-P., M. A. Richards, and J. R. Baumgardner (1997), A sensitivity study of three-dimensional spherical mantle convection at 10^8 Rayleigh number: Effects of depth-dependent viscosity, heating mode, and an endothermic phase change, *J. Geophys. Res.*, 102(B6), 11,991–12,007, doi:10.1029/96JB03806.
- Bunge, H.-P., M. A. Richards, C. Lithgow-Bertelloni, J. R. Baumgardner, S. P. Grand, and B. Romanowicz (1998), Time scales and heterogeneous structure in geodynamic earth models, *Science*, 280(5360), 91–96, doi:10.1126/science.280.5360.91.
- Bunge, H.-P., C. R. Hagelberg, and B. J. Travis (2003), Mantle circulation models with variational data assimilation: Inferring past mantle flow and structure from plate motion histories and seismic tomography, *Geophys. J. Int.*, 152(2), 280–301, doi:10.1046/j.1365-246X.2003.01823.x.
- Davies, D. R., S. Goes, J. H. Davies, B. S. A. Schuberth, H.-P. Bunge, and J. Ritsema (2012), Reconciling dynamic and seismic models of Earth's lower mantle: The dominant role of thermal heterogeneity, *Earth Planet. Sci. Lett.*, 353–354, 253–269, doi:10.1016/j.epsl.2012.08.016.
- Debayle, E., and Y. Ricard (2012), A global shear velocity model of the upper mantle from fundamental and higher Rayleigh mode measurements, *J. Geophys. Res.*, 117, 1–24, doi:10.1029/2012JB009288.
- Domeier, M., and T. H. Torsvik (2014), Plate tectonics in the late Paleozoic, *Geosci. Front.*, 5(3), 303–350, doi:10.1016/j.gsf.2014.01.002.
- Engelbreton, D. C., A. Cox, and R. G. Gordon (1984), Relative motions between oceanic plates of the Pacific Basin, *J. Geophys. Res.*, 89(B12), 10,291–10,310, doi:10.1029/JB089iB12p10291.
- Fournier, A., L. Nérger, and J. Aubert (2013), An ensemble Kalman filter for the time-dependent analysis of the geomagnetic field, *Geochem. Geophys. Geosyst.*, 14, 4035–4043, doi:10.1002/ggge.20252.
- Gordon, R. G., and D. M. Jurdy (1986), Cenozoic global plate motions, *J. Geophys. Res.*, 91(B12), 12,389–12,406, doi:10.1029/JB091iB12p12389.
- Grand, S. P., R. D. van der Hilst, and S. Widiyantoro (1997), Global seismic tomography: A snapshot of convection in the Earth, *Geol. Soc. Am.*, 7, 1–7.
- Gurnis, M., M. Turner, S. Zahirovic, L. DiCaprio, S. Spasojevic, R. D. Müller, J. Boyden, M. Seton, V. C. Manea, and D. J. Bower (2012), Plate tectonic reconstructions with continuously closing plates, *Comput. Geosci.*, 38, 35–42, doi:10.1016/j.jcageo.2011.04.014.
- Horbach, A., H.-P. Bunge, and J. Oeser (2014), The adjoint method in geodynamics: Derivation from a general operator formulation and application to the initial condition problem in a high resolution mantle circulation model, *GEM - Int. J. Geomath.*, 5(2), 163–194, doi:10.1007/s13137-014-0061-5.
- Iaffaldano, G. (2012), The strength of large-scale plate boundaries: Constraints from the dynamics of the Philippine Sea plate since 5 Ma, *Earth Planet. Sci. Lett.*, 357–358, 21–30, doi:10.1016/j.epsl.2012.09.018.
- Iaffaldano, G., L. Husson, and H.-P. Bunge (2011), Monsoon speeds up Indian plate motion, *Earth Planet. Sci. Lett.*, 304(3–4), 503–510, doi:10.1016/j.epsl.2011.02.026.

- Iaffaldano, G., T. Bodin, and M. Sambridge (2012), Reconstructing plate-motion changes in the presence of finite-rotations noise, *Nat. Commun.*, *3*, 1048, doi:10.1038/ncomms2051.
- Ismail-Zadeh, A., G. Schubert, I. Tsepelev, and A. Korotkii (2004), Inverse problem of thermal convection: Numerical approach and application to mantle plume restoration, *Phys. Earth Planet. Inter.*, *145*(1–4), 99–114, doi:10.1016/j.pepi.2004.03.006.
- Jarvis, G. T., and D. P. McKenzie (1980), Convection in a compressible fluid with infinite Prandtl number, *J. Fluid Mech.*, *96*(3), 515, doi:10.1017/S002211208000225X.
- Kalman, R. E. (1960), A new approach to linear filtering and prediction problems, *J. Basic Eng.*, *82*(1), 35, doi:10.1115/1.3662552.
- Lithgow-Bertelloni, C., and M. A. Richards (1998), The dynamics of Cenozoic and Mesozoic plate motions, *Rev. Geophys.*, *36*(1), 27–78, doi:10.1029/97RG02282.
- Lorenz, E. N. (1965), A study of the predictability of a 28-variable atmospheric model, *Tellus, Ser. A*, *17*(3), 321–333, doi:10.3402/tellusa.v17i3.9076.
- Mitrovica, J. X., and A. M. Forte (2004), A new inference of mantle viscosity based upon joint inversion of convection and glacial isostatic adjustment data, *Earth Planet. Sci. Lett.*, *225*(1–2), 177–189, doi:10.1016/j.epsl.2004.06.005.
- Oeser, J., H.-P. Bunge, and M. Mohr (2006), Cluster design in the Earth sciences: TETHYS, in *High Performance Computing and Communications—Second International Conference, HPCC 2006, Munich, Germany, Lecture Notes in Computer Science*, vol. 4208, edited by M. Gerndt and D. Kranzlmüller, pp. 31–40, Springer, Berlin, doi:10.1007/11847366_4.
- Paulson, A., and M. A. Richards (2009), On the resolution of radial viscosity structure in modelling long-wavelength postglacial rebound data, *Geophys. J. Int.*, *179*(3), 1516–1526, doi:10.1111/j.1365-246X.2009.04362.x.
- Piazzoni, A. S., G. Steinle-Neumann, H.-P. Bunge, and D. Dolejš (2007), A mineralogical model for density and elasticity of the Earth's mantle, *Geochem. Geophys. Geosyst.*, *8*(11), doi:10.1029/2007GC001697.
- Ritsema, J., A. Deuss, H.-J. Van Heijst, and J. H. Woodhouse (2011), S40RTS: A degree-40 shear-velocity model for the mantle from new Rayleigh wave dispersion, teleseismic traveltime and normal-mode splitting function measurements, *Geophys. J. Int.*, *184*(3), 1223–1236, doi:10.1111/j.1365-246X.2010.04884.x.
- Schuberth, B. S. A., H.-P. Bunge, and J. Ritsema (2009a), Tomographic filtering of high-resolution mantle circulation models: Can seismic heterogeneity be explained by temperature alone?, *Geochem. Geophys. Geosyst.*, *10*(5), Q05W03, doi:10.1029/2009GC002401.
- Schuberth, B. S. A., H.-P. Bunge, G. Steinle-Neumann, C. Moder, and J. Oeser (2009b), Thermal versus elastic heterogeneity in high-resolution mantle circulation models with pyrolite composition: High plume excess temperatures in the lowermost mantle, *Geochem. Geophys. Geosyst.*, *10*(1), doi:10.1029/2008GC002235.
- Serrin, J. (1959), Mathematical principles of classical fluid mechanics, in *Fluid Dynamics I/Strömungsmechanik I, Encyclopedia of Physics/Handbuch der Physik*, vol. 3/8/1, edited by J. Serrin, pp. 125–263, Springer, Berlin.
- Seton, M., et al. (2012), Global continental and ocean basin reconstructions since 200 Ma, *Earth Sci. Rev.*, *113*(3–4), 212–270, doi:10.1016/j.earscirev.2012.03.002.
- Shephard, G. E., H.-P. Bunge, B. S. A. Schuberth, R. D. Müller, A. S. Talsma, C. Moder, and T. C. W. Landgrebe (2012), Testing absolute plate reference frames and the implications for the generation of geodynamic mantle heterogeneity structure, *Earth Planet. Sci. Lett.*, *317–318*, 204–217, doi:10.1016/j.epsl.2011.11.027.
- Solheim, L. P., and W. R. Peltier (1990), Heat transfer and the onset of chaos in a spherical, axisymmetric, anelastic model of whole mantle convection, *Geophys. Astrophys. Fluid Dyn.*, *53*(4), 205–255, doi:10.1080/03091929008208928.
- Steinberger, B., and R. J. O'Connell (1997), Changes of the Earth's rotation axis owing to advection of mantle density heterogeneities, *Nature*, *387*(6629), 169–173, doi:10.1038/387169a0.
- Stewart, C. A., and D. L. Turcotte (1989), The route to chaos in thermal convection at infinite Prandtl number. I—Some trajectories and bifurcations, *J. Geophys. Res.*, *94*(B10), 13,707–13,717, doi:10.1029/JB094iB10p13707.
- Stixrude, L., and C. Lithgow-Bertelloni (2011), Thermodynamics of mantle minerals—II. Phase equilibria, *Geophys. J. Int.*, *184*(3), 1180–1213, doi:10.1111/j.1365-246X.2010.04890.x.
- Talagrand, O. (1997), Assimilation of observations, an introduction, *J. Meteorol. Soc. Jpn.*, *75*(1B), 191–209.
- Trubitsyn, V., M. K. Kaban, and M. Rothacher (2008), Mechanical and thermal effects of floating continents on the global mantle convection, *Phys. Earth Planet. Inter.*, *171*(1–4), 313–322, doi:10.1016/j.pepi.2008.03.011.
- Vynnytska, L., and H.-P. Bunge (2014), Restoring past mantle convection structure through fluid dynamic inverse theory: Regularisation through surface velocity boundary conditions, *GEM - Int. J. Geomath.*, *6*(1), 83–100, doi:10.1007/s13137-014-0060-6.
- Wunsch, C. (1996), *The Ocean Circulation Inverse Problem*, 458 pp., Cambridge Univ. Press, Cambridge, U. K.
- Yoshida, M., and M. Santosh (2011), Future supercontinent assembled in the Northern Hemisphere, *Terra Nova*, *23*(5), 333–338, doi:10.1111/j.1365-3121.2011.01018.x.
- Zhang, N., S. Zhong, W. Leng, and Z.-X. Li (2010), A model for the evolution of the Earth's mantle structure since the Early Paleozoic, *J. Geophys. Res.*, *115*(B6), doi:10.1029/2009JB006896.

50 4. On retrodictions of global mantle flow with assimilated surface velocities

Chapter 5

On the ratio of dynamic topography and gravity anomalies in a dynamic Earth

This chapter was published in the Journal “Geophysical Research Letters” in 2016. It clarifies the relationship between internal mass anomalies, gravity anomalies and dynamic topography for the real Earth. In particular, it shows that due consideration must be given to Earth’s sphericity, radial mantle viscosity stratification and isostatic compensation at the Core-Mantle Boundary.



RESEARCH LETTER

10.1002/2016GL067929

Key Points:

- The relation between mass anomalies, gravity anomalies, and dynamic topography is complex
- A constant admittance cannot capture this complex behavior
- Significant dynamic topography may exist without accompanying free-air gravity signal

Correspondence to:

L. Colli,
lorenzo.colli@geophysik.uni-muenchen.de

Citation:

Colli, L., S. Ghelichkhan, and H.-P. Bunge (2016), On the ratio of dynamic topography and gravity anomalies in a dynamic Earth, *Geophys. Res. Lett.*, *43*, doi:10.1002/2016GL067929.

Received 22 JAN 2016

Accepted 29 FEB 2016

Accepted article online 2 MAR 2016

©2016. American Geophysical Union.
All Rights Reserved.

On the ratio of dynamic topography and gravity anomalies in a dynamic Earth

L. Colli¹, S. Ghelichkhan¹, and H.-P. Bunge¹

¹Department of Earth and Environmental Sciences, University of Munich, Munich, Germany

Abstract Growing evidence from a variety of geologic indicators points to significant topography maintained convectively by viscous stresses in the mantle. However, while gravity is sensitive to dynamically supported topography, there are only small free-air gravity anomalies (<30 mGal) associated with Earth's long-wavelength topography. This has been used to suggest that surface heights computed assuming a complete isostatic equilibrium provide a good approximation to observed topography. Here we show that the apparent paradox is resolved by the well-established formalism of global, self-gravitating, viscously stratified Earth models. The models predict a complex relation between dynamic topography, mass, and gravity anomalies that is not summarized by a constant admittance—i.e., ratio of gravity anomalies to surface deflections—as one would infer from analytic flow solutions formulated in a half-space. Our results suggest that sizable dynamic topography may exist without a corresponding gravity signal.

1. Introduction

Variations in local gravity (see Figure 1a for a map of free-air gravity anomalies) have been essential in understanding mass anomalies in Earth's lithosphere ever since the geodetic surveys of the eighteenth century [e.g., *Bouguer and de La Condamine*, 1749; *Everest*, 1847], eventually giving rise to the theory of isostasy [*Airy*, 1855; *Pratt*, 1855]. Mass and gravity anomalies were subsequently studied in the context of viscous mantle flow [e.g., *Pekeris*, 1935; *Morgan*, 1965; *McKenzie*, 1977; *Richards and Hager*, 1984], when it was realized that normal stresses related to convection in a fluid with deformable boundaries would deflect those boundaries. Such surface deflections of the mantle, known as dynamic topography (see *Braun* [2010] and *Flament et al.* [2013] for recent reviews), produce gravity anomalies of comparable amplitude to the primary mass anomalies inside the mantle. The interpretation of Earth's gravity anomalies thus requires mass anomalies, flow, and resultant surface deflections to be taken into account.

Although gravity anomalies are well suited to map mass anomalies near Earth's surface, they are less sensitive to anomalies at greater depth because gravitational attraction is proportional to the inverse of distance squared. The gravitational potential, whose sea level equipotential is the geoid (Figure 1b), instead decreases as the inverse of distance. This has allowed geodynamicists to exploit the geoid to constrain self-gravitating dynamic Earth models in spherical geometry and to infer a significant viscosity increase from the upper to the lower mantle [e.g., *Ricard et al.*, 1984; *Richards and Hager*, 1984; *Forte and Mitrovica*, 2001].

The geoid provides fundamental constraints for geodynamic models. But inferences of dynamic topography are growing in importance, drawn from passive continental margins [e.g., *Japsen et al.*, 2012], marginal continental basins [*Guillocheau et al.*, 2012; *Autin et al.*, 2013; *Dressel et al.*, 2015], and the oceanic realm, where our understanding of plate subsidence as a function of age permits residual depth anomalies to be identified and mapped [*Winterbourne et al.*, 2014]. There is also evidence for episodic vertical motion, with repeated burial and exhumation along passive margins [e.g., *Praeg et al.*, 2005; *Japsen et al.*, 2012], as well as transient uplifts [e.g., *Hartley et al.*, 2011] with amplitudes approaching 1 km. In the South Atlantic region, moreover, spreading rate changes appear to correlate with uplift events, presumably owing to variations in pressure driven upper mantle flow [*Colli et al.*, 2014]. Dynamic topography thus seems an important means to infer convective circulation of the sublithospheric mantle. Its temporal evolution has implications for past mantle flow [*Gurnis et al.*, 1998], which one can constrain from retrodictions [*Colli et al.*, 2015], inverse flow modeling techniques [*Bunge et al.*, 2003; *Spasojevic et al.*, 2009; *Horbach et al.*, 2014], and backward advection [*Moucha and Forte*, 2011].

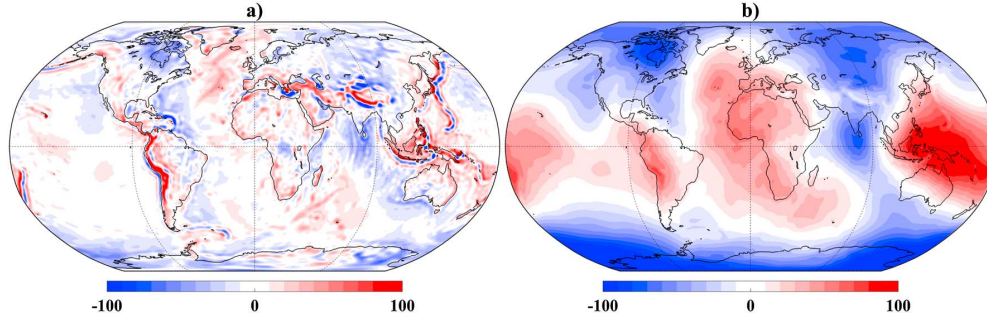


Figure 1. Robinson projection of (a) free-air gravity anomalies (mGal) and (b) low-pass-filtered geoid (meters), derived from GRACE and GOCE satellite missions, based on combined satellite-only model GOCO05S [Pail *et al.*, 2010], corrected for Earth's hydrostatic shape after Nakiboglu [1982]. Note that elevated southern Africa is characterized by a significant (50 m) geoid high but small free-air gravity anomalies.

While evidence for convectively maintained topography is mounting, it remains difficult to distinguish it from topography in isostatic support. Free-air gravity anomalies are sensitive to dynamically supported topography. Hence, Molnar *et al.* [2015] drew attention to the fact that only small free-air gravity anomalies (<30 mGal, see Figure 1a) are associated with long-wavelength topography and that most of the signal can be accounted for by assuming a complete isostatic compensation of the topography, concluding that normal stresses applied to the base of the lithosphere support less than ≈ 300 m of topography globally and little more ≈ 100 m in elevated terrains like southern Africa.

Molnar *et al.* [2015]'s analysis of the admittance, i.e., the ratio of surface deflections and gravity anomalies, employs analytical flow solutions for an infinite half-space. It provides physical insight and scaling rules. The gravitational analysis of deep mantle mass anomalies, however, must consider Earth's sphericity, radial mantle viscosity stratification, and isostatic compensation at the Core-Mantle Boundary (CMB), in addition to deflections at Earth's surface. These effects are embodied in global, self-gravitating, viscous mantle flow models. Here we refine the study of Molnar *et al.* [2015] by revisiting the theory of dynamic Earth models and exploring how a dynamically consistent relationship between gravity, surface deflections, and driving density contrasts affects the gravitational expression of convectively maintained topography.

2. Method

The theory for dynamic models of the geoid is well established [Hager, 1984; Richards and Hager, 1984] and involves solving for mass and momentum conservation together with Poisson's equation in a highly viscous spherical shell. Commonly, one represents the solutions through kernels, that is, Green's functions relating geoid undulation, N_{lm} , surface, S_{lm} , and CMB, C_{lm} , dynamic topography to a driving unit mass anomaly of given wavelength and depth. The spherical harmonic component F_{lm} of a quantity (e.g., geoid or boundary deflections) is computed in the spectral domain by a radial integration over the mantle depth:

$$F_{lm} = \int_{R_{\text{CMB}}}^{R_E} \delta\rho_{lm}(r) K_l^F(r) dr, \quad (1)$$

where $\delta\rho_{lm}$ is the a priori density anomaly at radius r and K_l^F is the appropriate kernel. The gravity anomaly Δg_{lm} is obtained from the geoid undulation N_{lm} via the fundamental equation of physical geodesy [e.g., Hofmann-Wellenhof and Moritz, 2006], which in spherical harmonics takes the form

$$\Delta g_{lm} = \frac{\gamma}{R_E} (l-1) N_{lm} \quad (2)$$

with γ being the reference gravity at the surface of the sphere. Furthermore, we define the *dynamic admittance* as the ratio of gravity over surface dynamic topography. For a unit mass anomaly of degree l and order m at depth r , the ratio writes as

$$K_l^a = \frac{K_l^{\Delta g}}{K_l^S} \quad (3)$$

We call K_l^a the *dynamic admittance kernel*. Note that estimating the *total* dynamic admittance for a given mantle density distribution requires separate integrations of numerator and denominator in (3).

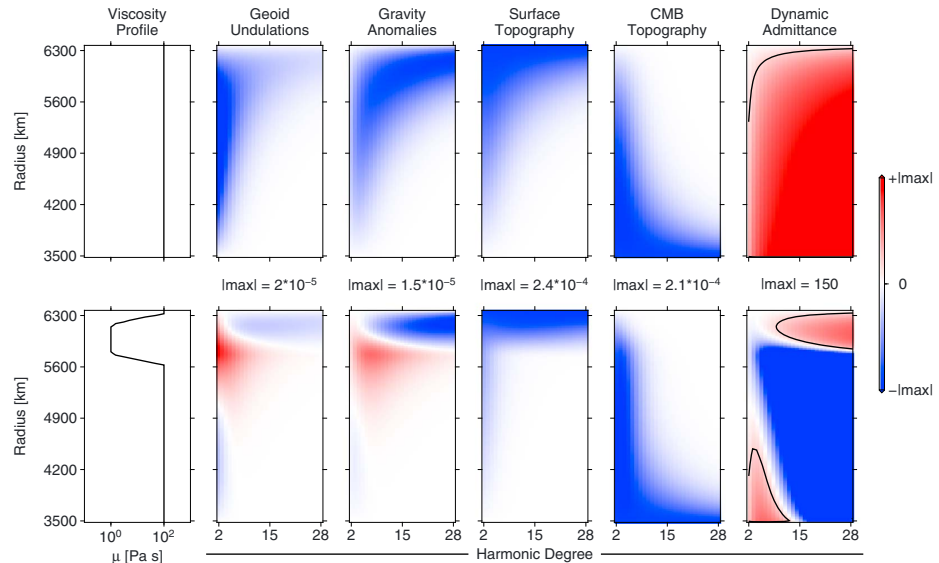


Figure 2. Viscosity profiles and kernels (see text) for geoid undulation, gravity anomaly, surface and CMB dynamic topography, and associated dynamic admittance, i.e., ratio of dynamic surface deflections and gravity anomalies, plotted as a function of radius and spherical harmonic degree for an isoviscous and layered viscosity (upper/lower row) Earth model. Colors show amplitude, normalized for minimum (blue), and maximum (red) value, with absolute value denoted for each column. Geoid, surface, and CMB dynamic topography kernels in $\text{m}/(\text{kg}/\text{m}^{-2})$, gravity kernel in $\text{mGal}/(\text{kg}/\text{m}^{-2})$, and dynamic admittance in mGal/km . Thick black line in dynamic admittance plots marks the 30 mGal/km isoline. Note that the low viscosity layer of the stratified viscosity model couples lower mantle density anomalies more strongly to the CMB; i.e., a larger part of the compensating mass is placed farther away from the surface so that geoid and gravity kernels become mostly positive. This renders dynamic admittance negative throughout most of the deep mantle, except for the lowest spherical harmonic degrees.

3. Results

For simplicity we consider two cases: a reference earth model with constant viscosity μ throughout the mantle and a layered viscosity case characterized by a 100-fold reduction in viscosity between 100 and 670 km depth. Figure 2 reports the viscosity profiles, together with the resulting kernels for geoid undulations, gravity anomalies, dynamic topography at the surface and the CMB, and the associated gravitational admittance.

Constant viscosity (Figure 2, top row) yields negative geoid kernels for all spherical harmonic degrees; i.e., density perturbations of all wavelengths and at all depth levels anticorrelate with the geoid undulations they induce. The kernels are zero at the surface and the CMB. For higher degrees their maximum absolute values are reached at shallower depth levels. The kernel amplitude moreover decreases rapidly with spherical harmonic degree so that long-wavelength lower mantle anomalies affect the geoid more strongly than short-wavelength upper mantle anomalies. The gravity kernels are negative as well. But the dependence of gravitational attraction on the inverse of the distance squared favors shallower and shorter-wavelength anomalies. Kernels for surface and CMB deflection are always negative and nearly mirror each other. The surface deflection kernels take the value of $-1/\rho_m$ at the surface for all harmonic degrees, falling off to zero toward the CMB with higher degrees decaying faster. At the same time, the CMB deflection kernels equal $-1/(\rho_c - \rho_m)$ at the CMB, while decaying toward the surface. This means that near surface density anomalies are isostatically compensated mostly by surface deflections (notice that we assume subaerial topography), while deeper anomalies involve growing compensation across the CMB. Figure 2 (sixth column) reports the gravitational admittance—i.e., the ratio of surface deflections and gravity anomalies—implied by an isoviscous Earth model. The admittance is wavelength dependent [Kiefer *et al.*, 1986] and for the most part larger than 30 mGal/km , except for long-wavelength anomalies near the surface.

Viscosity stratification alters the relation between geoid, surface deflections, and driving density contrast [e.g., Ricard *et al.*, 1984; Richards and Hager, 1984]. The kernels in this case (Figure 2, bottom row) change sign with

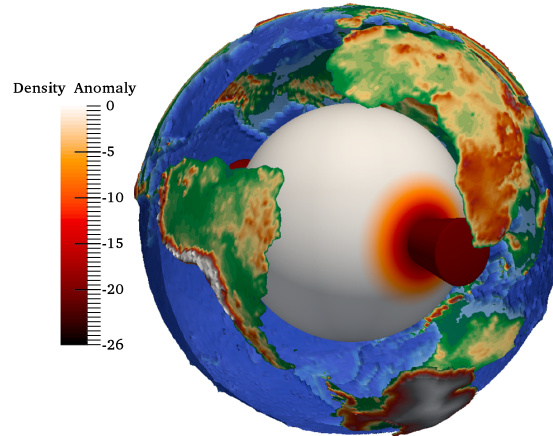


Figure 3. Three-dimensional view, centered on African hemisphere, of assumed (see text) long-wavelength, deep mantle (1000 km depth to CMB), antipodal density anomaly (kg/m^3), with an isosurface for the density anomaly drawn at -20 kg/m^3 , and continental outlines and topography shown for spatial reference. White inner sphere represents CMB.

depth, include zero crossings, and assume mostly positive values in the lower mantle. The surface deflection kernels remain negative but decay rapidly in amplitude beneath the low-viscosity layer. Conversely, the CMB deflection kernels assume larger values there, implying stronger compensation of lower mantle density perturbations by topography along the CMB. The gravitational admittance reflects these changes: we observe negative values for most spherical harmonic degrees and depth levels, with positive values larger than 30 mGal/km confined to low-degree anomalies in the lowermost mantle as well as high-degree anomalies in the upper mantle.

Kernels are useful to illustrate the gravitational response of a dynamic Earth to internal loads. But the spatial pattern of dynamic topography and gravity anomalies induced by any given density perturbation is equally illuminating. To this end, we approximate the prominent lower mantle LLSVPs inferred beneath Africa and the Pacific [e.g., *Ritsema et al.*, 2011; *French and Romanowicz*, 2014] by a long-wavelength antipodal density anomaly (see Figure 3), assuming a maximum amplitude of -26 kg/m^3 , consistent with a $250\text{--}350 \text{ K}$ thermal perturbation [*Schuberth et al.*, 2009a; *Davies et al.*, 2015]. Figure 4 displays the resulting geoid undulations, gravity anomalies, dynamic topography, and gravitational admittance, where the top row reports the isoviscous reference case, while the model involving mantle viscosity stratification is shown at the bottom.

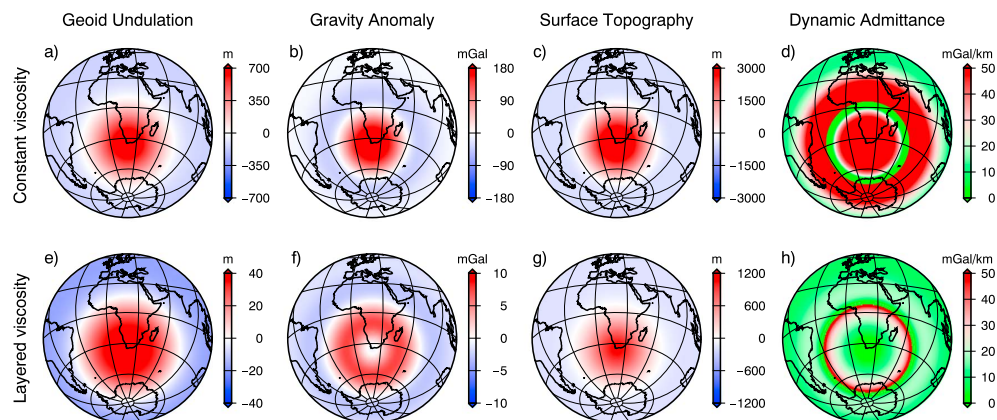


Figure 4. Lambert azimuthal projection of geoid undulations, gravity anomalies, surface topography, and dynamic admittance produced by density anomaly of Figure 3. (top and bottom rows) Isoviscous/layered viscosity case. Note that constant viscosity Earth model gives unrealistically high values for all quantities, while layered viscosity case shows Earth-like values for geoid and gravity anomaly and a low admittance nearly everywhere, especially in the most elevated regions.

The isoviscous model yields a maximum geoid high, gravity anomaly, and dynamic topography of, respectively, 740 m, 190 mGal, and 3.4 km, producing a gravitational admittance greater than 50 mGal/km. In contrast, the layered viscosity case yields smaller perturbations (geoid: 37 m, gravity: 8 mGal, and dynamic topography: 1.1 km). While gravity anomalies and geoid undulations are reduced by a factor of ≈ 20 , dynamic topography decreases only by a factor of ≈ 3 relative to the isoviscous Earth model, and the gravitational admittance in this case is for the most part less than 10 mGal/km.

4. Discussion

Growing evidence points to topography maintained convectively by flow in the underlying mantle. In the oceans it is suggested by accurate measurements of residual topography [Winterbourne *et al.*, 2014]. On the continents, where we lack reliable depth-age relations, it comes from the analysis of free-air gravity anomalies, assuming as a rule of thumb an admittance of 50 mGal/km to convert free-air anomalies into dynamically supported terrain [e.g., Molnar *et al.*, 2015]. Such analysis suggests, for instance, that Africa's distinct basin and swell topography owes partly to sublithospheric flow [Paul *et al.*, 2014].

Our results support the rule of thumb admittance scaling for a global isoviscous self-gravitating Earth model, which yields values of over 50 mGal/km (see Figure 4d). However, they indicate at the same time that the scaling underestimates the dynamic support in a viscously stratified Earth model, where significant convectively maintained terrain may exist without accompanying free-air gravity signal. The global mantle flow model with upper/lower mantle viscosity contrast displays dynamic topography > 1 km, while the admittance does not exceed 10 mGal/km (see Figure 4h) even in the most elevated regions.

This seemingly surprising result is expected from the dynamic response functions (Figure 2) of a viscous Earth [Hager, 1984; Richards and Hager, 1984]. Kernels for an isoviscous mantle are invariably negative. Viscously stratified Earth models, instead, display geoid and gravity kernels that change sign with depth: positive density anomalies yield negative or positive geoid and gravity signals or none, and vice versa, depending on their mantle depth. Essentially, the lower mantle density anomalies are compensated preferentially by dynamic topography along the CMB, an effect not captured by flow solutions formulated in a half-space. Admittance scalings based on half-space solutions thus provide us with lower bounds on dynamic topography inferred from free-air gravity anomalies, by emphasizing upper mantle convective support.

Our analysis should be qualified. For instance, we assumed a thermal origin for the lower mantle density perturbations to keep things simple. Seismic imaging reveals a substantial depthwise heterogeneity increase in the lowermost mantle [e.g., Grand *et al.*, 1997; Simmons *et al.*, 2010; Ritsema *et al.*, 2011; French and Romanowicz, 2014], for which deep mantle compositional variation has been invoked [McNamara and Zhong, 2005]. However, subadiabaticity [Bunge, 2005] and compressibility effects increase the heterogeneity strength with depth in isochemical mantle flow [Schuberth *et al.*, 2009a]. This has been used for a quantitative analysis of deep mantle seismic heterogeneity by temperature alone in mantle circulation models that account for tomographic filtering [Schuberth *et al.*, 2009b; Davies *et al.*, 2012].

In addition, our analysis considered incompressible mantle flow equations while, owing to mantle self-compression, density increases by almost a factor of 2 [Dziewonski and Anderson, 1981] from the surface to the CMB. Corrieu *et al.* [1995] and Panasyuk *et al.* [1996] computed Geoid kernels for compressible Earth models and concluded that compressibility has minor effects on the overall shape of geoid kernels compared to layered viscosity. In other words, Earth models having a viscosity increase between upper and lower mantle regions retain kernels that change sign with depth. As a consequence, lower mantle density anomalies involve a significant compensation by dynamic topography along the CMB also in a compressible Earth, leaving our primary observations unchanged.

5. Conclusions

Geodynamic Earth models that account for sphericity, finite mantle thickness, and viscosity stratification predict a complex relation between internal mass anomalies, gravity anomalies, and surface dynamic topography that is not summarized by a constant admittance. In such models, internal mass anomalies may produce sizable, kilometer-scale dynamic topography associated with either positive, negative, or zero gravity



anomalies, depending on their wavelength and depth within the mantle. We conclude that the use of global, self-gravitating, viscously stratified Earth models is advised, when applying free-air gravity anomalies in the study of convectively maintained surface topography.

Acknowledgments

The authors acknowledge valuable comments by Mark Richards and thank Mike Gurnis and Yanick Ricard for their constructive reviews. Support for L. Colli was provided by the DFG SAMPLE program. All data for this paper are properly cited and referred to in the reference list.

References

- Airy, G. B. (1855), On the computation of the effect of the attraction of mountain-masses, as disturbing the apparent and astronomical latitude of stations in geodetic surveys, *Philos. Trans. R. Soc.*, *145*, 101–104, doi:10.1098/rstl.1855.0003.
- Autin, J., et al. (2013), Colorado basin 3D structure and evolution, argentine passive margin, *Tectonophysics*, *604*, 264–279, doi:10.1016/j.tecto.2013.05.019.
- Bouguer, P., and C. de La Condamine (1749), *La figure de la terre: déterminée par les observations de messieurs Bouguer, et de la Condamine, de l'Académie Royale des Sciences, envoyés par ordre du roy au Pérou, pour observer aux environs de l'équateur; avec une relation abrégée de ce voyage, qui contient la description du pays dans lequel les opérations ont été faites*, Charles-Antoine Jombert, Paris.
- Braun, J. (2010), The many surface expressions of mantle dynamics, *Nat. Geosci.*, *3*(12), 825–833, doi:10.1038/ngeo1020.
- Bunge, H.-P. (2005), Low plume excess temperature and high core heat flux inferred from non-adiabatic geotherms in internally heated mantle circulation models, *Phys. Earth Planet. Inter.*, *153*(1–3), 3–10, doi:10.1016/j.pepi.2005.03.017.
- Bunge, H.-P., C. R. Hagelberg, and B. J. Travis (2003), Mantle circulation models with variational data assimilation: Inferring past mantle flow and structure from plate motion histories and seismic tomography, *Geophys. J. Int.*, *152*(2), 280–301, doi:10.1046/j.1365-246X.2003.01823.x.
- Colli, L., I. Stotz, H. Bunge, M. A. Smethurst, S. Clark, G. Iaffaldano, A. Tassara, F. Guillocheau, and M. C. Bianchi (2014), Rapid South Atlantic spreading changes and coeval vertical motion in surrounding continents: Evidence for temporal changes of pressure-driven upper mantle flow, *Tectonics*, *33*(7), 1304–1321, doi:10.1002/2014TC003612.
- Colli, L., H.-P. Bunge, and B. S. A. Schuberth (2015), On retrodictions of global mantle flow with assimilated surface velocities, *Geophys. Res. Lett.*, *42*, 8341–8348, doi:10.1002/2015GL066001.
- Corrieu, V., C. Thoraval, and Y. Ricard (1995), Mantle dynamics and geoid Green functions, *Geophys. J. Int.*, *120*(2), 516–523, doi:10.1111/j.1365-246X.1995.tb01835.x.
- Davies, D. R., S. Goes, J. H. Davies, B. S. A. Schuberth, H.-P. Bunge, and J. Ritsema (2012), Reconciling dynamic and seismic models of Earth's lower mantle: The dominant role of thermal heterogeneity, *Earth Planet. Sci. Lett.*, *353–354*, 253–269, doi:10.1016/j.epsl.2012.08.016.
- Davies, D. R., S. Goes, and H. C. P. Lau (2015), Thermally dominated deep mantle LLSVPs: A review, in *The Earth's Heterogeneous Mantle*, chap. 14, pp. 441–477, Springer Int. Publ., Switzerland, doi:10.1007/978-3-319-15627-9.
- Dressler, I., M. Scheck-Wenderoth, M. Cacace, B. Lewerenz, H.-J. Götze, and C. Reichert (2015), Reconstruction of the southwestern African continental margin by backward modeling, *Mar. Pet. Geol.*, *67*, 544–555, doi:10.1016/j.marpetgeo.2015.06.006.
- Dziewonski, A. M., and D. L. Anderson (1981), Preliminary reference Earth model, *Phys. Earth Planet. Inter.*, *25*, 297–356, doi:10.1111/j.1365-246X.2005.02780.x.
- Everest, G. (1847), *An Account of the Measurement of Two Sections of the Meridional Arc of India*, J. and H. Cox, Univ. of Minnesota.
- Flament, N., M. Gurnis, and R. D. Müller (2013), A review of observations and models of dynamic topography, *Lithosphere*, *5*(2), 189–210, doi:10.1130/L245.1.
- Forte, A. M., and J. X. Mitrovica (2001), Deep-mantle high-viscosity flow and thermochemical structure inferred from seismic and geodynamic data, *Nature*, *410*, 1049–1056, doi:10.1038/35074000.
- French, S. W., and B. A. Romanowicz (2014), Whole-mantle radially anisotropic shear velocity structure from spectral-element waveform tomography, *Geophys. J. Int.*, *199*(3), 1303–1327, doi:10.1093/gji/ggu334.
- Grand, S. P., R. D. van der Hilst, and S. Widiyantoro (1997), High resolution global tomography: A snapshot of convection in the Earth, *Geol. Soc. Am. Today*, *7*(4), 1–7.
- Guillocheau, F., D. Rouby, C. Robin, C. Helm, N. Rolland, C. Le Carlier de Veslud, and J. Braun (2012), Quantification and causes of the terrigenous sediment budget at the scale of a continental margin: A new method applied to the Namibia-South Africa margin, *Basin Res.*, *24*(1), 3–30, doi:10.1111/j.1365-2117.2011.00511.x.
- Gurnis, M., R. D. Müller, and L. Moresi (1998), Cretaceous vertical motion of Australia and the Australian-Antarctic discordance, *Science*, *279*(5356), 1499–1504, doi:10.1126/science.279.5356.1499.
- Hager, B. H. (1984), Subducted slabs and the geoid: Constraints on mantle rheology and flow, *J. Geophys. Res.*, *89*(B7), 6003–6015, doi:10.1029/JB089iB07p06003.
- Hartley, R. A., G. G. Roberts, N. J. White, and C. Richardson (2011), Transient convective uplift of an ancient buried landscape, *Nat. Geosci.*, *4*(8), 562–565, doi:10.1038/ngeo1191.
- Hofmann-Wellenhof, B., and H. Moritz (2006), *Physical Geodesy*, Springer, Vienna, doi:10.1007/978-3-211-33545-1.
- Horbach, A., H.-P. Bunge, and J. Oeser (2014), The adjoint method in geodynamics: Derivation from a general operator formulation and application to the initial condition problem in a high resolution mantle circulation model, *Int. J. Geomath.*, *5*(2), 163–194.
- Japsen, P., J. A. Chalmers, P. F. Green, and J. M. Bonow (2012), Elevated, passive continental margins: Not rift shoulders, but expressions of episodic, post-rift burial and exhumation, *Glob. Planet. Change*, *90–91*, 73–86, doi:10.1016/j.gloplacha.2011.05.004.
- Kiefer, W. S., M. A. Richards, B. H. Hager, and B. G. Bills (1986), A dynamic model of Venus's gravity field, *Geophys. Res. Lett.*, *13*(1), 14–17, doi:10.1029/GL013i001p00014.
- McKenzie, D. P. (1977), Surface deformation, gravity anomalies and convection, *Geophys. J. R. Astron. Soc.*, *48*, 211–238.
- McNamara, A. K., and S. Zhong (2005), Thermochemical structures beneath Africa and the Pacific Ocean, *Nature*, *437*(7062), 1136–1139, doi:10.1038/nature04066.
- Molnar, P., P. C. England, and C. H. Jones (2015), Mantle dynamics, isostasy, and the support of high terrain, *J. Geophys. Res. Solid Earth*, *128*, 1932–1957, doi:10.1002/2014JB011724.
- Morgan, W. J. (1965), Gravity anomalies and convection currents: 1. A sphere and cylinder sinking beneath the surface of a viscous fluid, *J. Geophys. Res.*, *70*(24), 6175–6187, doi:10.1029/JZ070i024p06175.
- Moucha, R., and A. M. Forte (2011), Changes in African topography driven by mantle convection, *Nat. Geosci.*, *4*(10), 707–712, doi:10.1038/ngeo1235.
- Nakiboglu, S. (1982), Hydrostatic theory of the Earth and its mechanical implications, *Phys. Earth Planet. Inter.*, *28*(4), 302–311, doi:10.1016/0031-9201(82)90087-5.
- Pail, R., et al. (2010), Combined satellite gravity field model GOCO01S derived from GOCE and GRACE, *Geophys. Res. Lett.*, *37*, L20314, doi:10.1029/2010GL044906.

- Panasjuk, S. V., B. H. Hager, and A. M. Forte (1996), Understanding the effects of mantle compressibility on geoid kernels, *Geophys. J. Int.*, *124*(1), 121–133, doi:10.1111/j.1365-246X.1996.tb06357.x.
- Paul, J. D., G. G. Roberts, and N. White (2014), The African landscape through space and time, *Tectonics*, *33*(6), 898–935, doi:10.1002/2013TC003479.
- Pekeris, C. L. (1935), Thermal convection in the interior of the Earth, *Geophys. J. Int.*, *3*(8), 343–367, doi:10.1111/j.1365-246X.1935.tb01742.x.
- Praeg, D., M. S. Stoker, P. M. Shannon, S. Ceramicola, B. Hjelstuen, J. S. Laberg, and A. Mathiesen (2005), Episodic cenozoic tectonism and the development of the NW European passive continental margin, *Mar. Pet. Geol.*, *22*(9–10), 1007–1030, doi:10.1016/j.marpetgeo.2005.03.014.
- Pratt, J. H. (1855), On the attraction of the Himalaya mountains, and of the elevated regions beyond them, upon the plumb-line in India, *Philos. Trans. R. Soc.*, *145*, 53–100, doi:10.1098/rstl.1855.0002.
- Ricard, Y., L. Fleitout, and C. Froidevaux (1984), Geoid heights and lithospheric stresses for a dynamic Earth, *Ann. Geophys.*, *2*(3), 267–286.
- Richards, M. A., and B. H. Hager (1984), Geoid anomalies in a dynamic Earth, *J. Geophys. Res.*, *89*(B7), 5987–6002, doi:10.1029/JB089iB07p05987.
- Ritsema, J., A. Deuss, H. J. van Heijst, and J. H. Woodhouse (2011), S40RTS: A degree-40 shear-velocity model for the mantle from new Rayleigh wave dispersion, teleseismic traveltimes and normal-mode splitting function measurements, *Geophys. J. Int.*, *184*(3), 1223–1236, doi:10.1111/j.1365-246X.2010.04884.x.
- Schuberth, B. S. A., H.-P. Bunge, G. Steinle-Neumann, C. Moder, and J. Oeser (2009a), Thermal versus elastic heterogeneity in high-resolution mantle circulation models with pyrolite composition: High plume excess temperatures in the lowermost mantle, *Geochem. Geophys. Geosyst.*, *10*, Q01W01, doi:10.1029/2008GC002235.
- Schuberth, B. S. A., H.-P. Bunge, and J. Ritsema (2009b), Tomographic filtering of high-resolution mantle circulation models: Can seismic heterogeneity be explained by temperature alone?, *Geochem. Geophys. Geosyst.*, *10*, Q05W03, doi:10.1029/2009GC002401.
- Simmons, N. A., A. M. Forte, L. Boschi, and S. P. Grand (2010), GyPSuM: A joint tomographic model of mantle density and seismic wave speeds, *J. Geophys. Res.*, *115*, B12310, doi:10.1029/2010JB007631.
- Spasojevic, S., L. Liu, and M. Gurnis (2009), Adjoint models of mantle convection with seismic, plate motion, and stratigraphic constraints: North America since the Late Cretaceous, *Geochem. Geophys. Geosyst.*, *10*, Q05W02, doi:10.1029/2008GC002345.
- Winterbourne, J., N. J. White, and A. Crosby (2014), Accurate measurements of residual topography from the oceanic realm, *Tectonics*, *33*, 982–1015, doi:10.1002/2013TC003372.

Chapter 6

Retrodictions of late Paleogene mantle flow and dynamic topography in the Atlantic region from compressible high resolution adjoint mantle convection models: sensitivity to deep mantle viscosity and tomographic input model

This chapter has been submitted for publication to the Journal “Gondwana Research” in 2016. It describes and discusses the first retrodictions of mantle flow and dynamic topography for geodynamically plausible, compressible, high resolution Earth models, going back in time to the late Paleogene.

Retrodictions of late Paleogene mantle flow and
dynamic topography in the Atlantic region from
compressible high resolution adjoint mantle convection
models: sensitivity to deep mantle viscosity and
tomographic input model

L. Colli^a, S. Ghelichkhan^a, H.-P. Bunge^a, J. Oeser^a

^a*Department of Earth and Environmental Sciences, University of Munich, Theresienstrasse
41, 80333 Munich, Germany*

Abstract

Although mantle convection at Earth-like vigor is a chaotic process, it has been shown by conceptual studies that one can constrain its flow history back in time for periods comparable to a mantle overturn, ≈ 100 million years, if knowledge of the horizontal surface velocity field and estimates on the present-day heterogeneity state are available. Such retrodictions, enabled through computationally demanding adjoint methods, are a promising tool to improve our understanding of deep Earth processes, and to link uncertain geodynamic modelling parameters to geologic observables. Here we present the first mantle flow retrodictions for geodynamically plausible, compressible, high resolution Earth models with ≈ 670 million finite elements, going back in time to the late Paleogene. Our retrodictions involve the dynamic effects from a low viscosity zone (LVZ) in the upper mantle, assimilate a past plate motion model for the horizontal surface velocity field, and probe the influence from uncertain modeling parameters by using two different estimates for the present-day heterogeneity state of the mantle as imaged by two recent seismic tomographic studies, and two different values for deep mantle viscosity. Focusing on the African hemisphere, we find that our retrodictions produce a spatially and temporally highly variable asthenosphere flow with faster-than-plate velocities, and a history of dynamic topography characterized by local doming events, in agreement with considerations on plate driving forces, and regional scale uplifts reported in the geologic literature. Our results suggest that improved constraints on non-isostatic vertical motion of Earth's surface — provided, for instance, by basin analysis, seismic stratigraphy, landform studies, or the sedimentation record — will play an important role in our understanding of the recent mantle flow history.

Keywords: mantle convection, adjoint method, dynamic topography,

Email address: colli@geophysik.uni-muenchen.de (L. Colli)

retrodicted, Atlantic region

1. Introduction

Over the last 25 years our geodynamic understanding of how to retrodict past mantle states has progressed significantly. Early backward advection schemes (e.g., *Bunge and Richards, 1992; Steinberger and O'Connell, 1997*), where one integrates model heterogeneity back in time by reversing the time step of the energy equation and ignoring thermal diffusion, have given way to a formal inverse problem based on an adjoint approach, with so-called adjoint equations providing sensitivity information in the geodynamic model relative to earlier system states. Adjoint equations have been derived for incompressible (*Bunge et al., 2003; Ismail-Zadeh et al., 2004; Horbach et al., 2014*) and compressible (*Ghelichkhan and Bunge, 2016*) mantle flow. Moreover, geodynamicists have related the uniqueness properties of the inverse problem explicitly to the horizontal component of the surface velocity field of a mantle convection model (*Colli et al., 2015*), showing that knowledge of the latter is essential to assure convergence (*Vynnytska and Bunge, 2014*) and to obtain a small null space for the restored flow evolution (*Horbach et al., 2014*).

At the same time, mantle convection models have become ever more sophisticated (*Zhong et al., 2015*). Many model features, such as complex rheologies or thermochemical flow properties, involve ad-hoc parameterizations and long-range extrapolations, so that testing mantle convection models against observables is important. The long time scales of mantle flow, on the order of millions of years, rule out predictions on future system states. But viable tests of mantle convection models, to resolve uncertainties in model parameters and the assumptions they are based upon, can be done by comparing past mantle states obtained through retrodictions against constraints gleaned from the geologic record.

Plate motions are a primary geologic observable, and a surface expression of mantle convection (*Davies and Richards, 1992*). However, one needs to assimilate the horizontal component of the surface velocity field (i.e., a past plate motion model) to assure convergence of the inverse problem (*Vynnytska and Bunge, 2014*). This makes past plate motions the input of retrodictions rather than their output. Moreover, plate motions reflect a balance of *deep* body forces related to mantle buoyancies and *shallow* plate-boundary forces (see *Iaffaldano and Bunge, 2015*, for a recent review) related, for instance, to topography and friction (*Iaffaldano and Bunge, 2009*). It is likely that some plate motion variations owe to evolving topography (*Iaffaldano et al., 2006; Austermann and Iaffaldano, 2013*) or changes in plate boundary strength resulting from variable sediment intake (*Iaffaldano, 2012*). In mantle convection models one would have to parameterize such effects, making plate motion histories suboptimal for testing mantle flow retrodictions.

It is well known that viscous stresses from mantle flow induce vertical deflections of Earth's surface (*Pekeris, 1935; Hager and Gurnis, 1987*) in addition to

driving the horizontal component of plate movement. These surface deflections, referred to as dynamic topography (see *Braun, 2010; Flament et al., 2013*, for recent reviews), were recognized early on in the sedimentary record (e.g., *Stille, 1919*). Recent years have seen much improvement in the amount and quality of dynamic topography inferences, drawn from passive continental margins (e.g., *Japsen et al., 2012a*), marginal continental basins (*Guillocheau et al., 2012; Autin et al., 2013; Dressel et al., 2015*), continental interiors (*Stanley et al., 2015*), or the oceanic realm, where our understanding of plate subsidence as a function of age permits residual depth anomalies to be identified and mapped (*Winterbourne et al., 2014*).

The passive continental margins of the Atlantic region (see Figure 1) are a prime location to map Earth's surface deflections. Located away from active plate boundaries, their post-rifting thermal subsidence generates accommodation space that preserves an archive in the sedimentary record. A variety of inferences suggests that topography in the Atlantic realm has changed in time: *Macgregor (2012)* summarizes episodes of margin uplifts for South America and Africa in Late Cretaceous and Oligocene, while *Japsen et al. (2012b)* document Late Cretaceous and Eocene uplift events along the Brazilian coast. In the North Atlantic region there is evidence for episodic vertical motion with repeated burial and exhumation (e.g., *Praeg et al., 2005; Japsen et al., 2012a*), as well as transient uplifts (e.g., *Hartley et al., 2011*) with amplitudes approaching 1 km. Spreading rate changes in the South Atlantic region, moreover, appear to correlate with uplift events, induced presumably by changes in pressure-driven upper mantle flow (*Colli et al., 2014*). Dynamic topography and its temporal changes thus have the potential to constrain convective circulation in the sublithospheric mantle.

Geodynamic retrodictions are limited at the current time by uncertainties in the assumed modelling parameters for Earth's mantle. In particular, the rheology is not well known. Direct measurements of the stress-strain relation for mantle rocks in laboratory deformation studies are difficult (*Karato, 2010*), as experimentally viable strain rates exceed geologically relevant ones by orders of magnitude, although multiscale material modelling may offer new constraints, for instance, on athermal deformation regimes in the deep mantle (*Amodeo et al., 2015*). Complementary information comes from geodynamic studies of glacial isostatic adjustment (GIA) (e.g., *Mitrovica, 1996*) and the geoid (e.g., *Richards and Hager, 1984*). The first are concerned with surface deformations following Holocene deglaciation, while the second exploit instantaneous solutions of the momentum equation in order to model perturbations to Earth's hydrostatic gravity field arising from mantle density anomalies and the surface deformation (dynamic topography) they induce.

A robust conclusion from these geodynamic studies is that the upper part of the mantle has a lower viscosity than its lower part. The resolving power, however, is limited (*Paulson et al., 2007*) and the resulting inference is affected by a strong trade-off between the thickness of the low-viscosity upper layer and its viscosity reduction (*Paulson and Richards, 2009; Schaber et al., 2009*). In geoid models the trade-off rests with the loading function, i.e., the assumed mantle

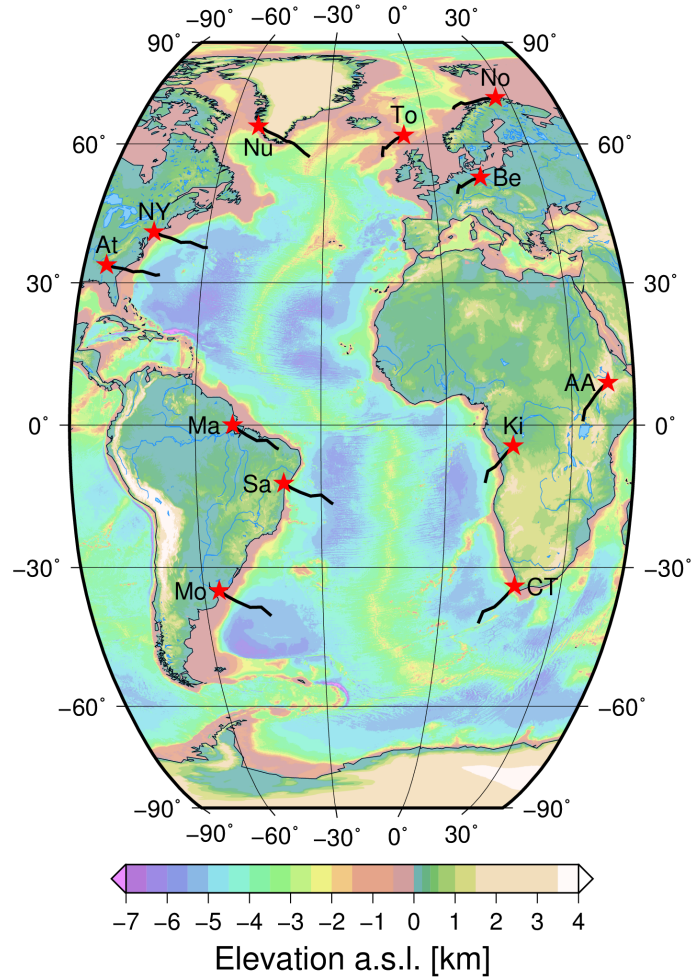


Figure 1: Topographic map of the Atlantic Ocean and adjacent continents from ETOPO1 (*Amante and Eakins, 2009*). Red stars and solid thick black lines denote the present position and the paleo locations of selected cities whose reconstructed histories of dynamic topography variations are plotted in Figure 15. AA: Addis Ababa, At: Atlanta, Be: Berlin, CT: Cape Town, Ki: Kinshasa, Ma: Macapa, Mo: Montevideo, NY: New York, No: Nordkapp, Nu: Nuuk, Sa: Salvador, To: Torshavn. Robinson projection.

density structure, which is fixed in space and time. Mantle flow retrodictions would yield time varying loading functions, i.e., density anomalies advected by mantle circulation. Their comparison with geologic inferences of evolving dynamic topography thus has the potential to help reduce the trade-off between competing mantle viscosity models.

The mantle thermochemical structure from which one retrodicts past mantle states is also not well known. It is possible in principle to map seismic

heterogeneity derived by global seismic tomography to temperature and density through thermodynamically self-consistent models of mantle mineralogy (e.g., *Piazzoni et al.*, 2007; *Stixrude and Lithgow-Bertelloni*, 2011). But this approach suffers from a number of uncertainties (e.g., *Cammarano et al.*, 2003; *Afonso et al.*, 2013; *Connolly and Khan*, 2016) and a well known trade-off between compositional and thermal variations (*Mosca et al.*, 2012). Some considerations are therefore required: First, mantle density increases by nearly a factor of two (*Dziewonski and Anderson*, 1981) from the surface to the Core Mantle Boundary (CMB) due to compression induced by self-gravitation. Compressibility effects should therefore be considered in retrodictions to account for mantle heterogeneity in a dynamically consistent way. For instance, the depthwise heterogeneity increase in the lowermost mantle revealed by seismic imaging (e.g., *Grand et al.*, 1997; *Ritsema et al.*, 2011; *Simmons et al.*, 2012; *French and Romanowicz*, 2014) seems best explained in mantle convection models restricted to an incompressible formulation by invoking compositional variations (*McNamara and Zhong*, 2005). But compressibility effects and mantle subadiabaticity (*Bunge*, 2005) raise the excess temperature of mantle plumes with depth (*Leng and Zhong*, 2008; *Schuberth et al.*, 2009a, and references therein). This makes it plausible to account for deep mantle heterogeneity by temperature alone (*Schuberth et al.*, 2009b; *Davies et al.*, 2012).

Second, the limited data coverage available for seismic studies makes tomographic inverse problems ill-posed. So an explicit regularization, usually in the form of damping and/or smoothing of the seismic model, is needed. While regularization parameters directly impact the size and amplitude of seismic anomalies, their choice is to a large extent subjective (*Ritsema et al.*, 2011). *Zaroli et al.* (2013) proposed some objective rationales to constrain the regularization parameters. But their span is still sufficiently large to permit a factor of ≈ 2 uncertainty in the RMS amplitude of seismic anomalies (*Zaroli et al.*, 2013). Additional uncertainties arise from theoretical simplifications (e.g., the high-frequency approximation in raypath tomography) and unmodelled effects. New tomographic techniques based on finite-frequency and full-waveform methods (*Tarantola*, 1988; *Dahlen et al.*, 2000) employ more complete physics to improve data coverage and reduce modeling errors. Seismic tomographies based on these techniques (e.g., *Fichtner et al.*, 2009; *Colli et al.*, 2013) should yield sharper images of seismic anomalies and more robust constraints on their amplitudes (*Zhou et al.*, 2005).

Still, current tomographic models agree over length scales of thousands of km (*Becker and Boschi*, 2002; *Debayle and Ricard*, 2012), while differences remain at smaller scales. As structures down to scales of ≈ 100 km (equivalent to a thermal boundary layer thickness) play an active role in mantle flow, the current seismic resolution limits imply dynamically significant features of Earth's mantle to be either smeared or absent (*Bunge and Davies*, 2001; *Schuberth et al.*, 2009b; *Ritsema et al.*, 2011), affecting our ability to retrodict past mantle states.

In this paper we discuss how retrodictions of past mantle states can help to advance our understanding of mantle rheology and buoyancy by linking geophysical and geologic constraints on present and past states of the Earth con-

sistently through geodynamic mantle flow evolutions. To this end, we employ two recent tomographic models by *Afanasiev et al.* (2015) and *Simmons et al.* (2015), and the mantle mineralogy model of *Stixrude and Lithgow-Bertelloni* (2011) to obtain two different state estimates of present thermal mantle structure. We retrodict both state estimates 40 Myrs back in time, equivalent to the late Paleogene, and account for rheologic model uncertainty in a simple way, by assuming two plausible radial viscosity profiles, for a total of four different mantle flow retrodictions. While our results demonstrate the overall feasibility of the method, yielding broadly similar results across the retrodictions, they also motivate the search for tighter bounds on mantle seismic structure and estimates of past dynamic topography, to address the different model results that are permissible in the range of current uncertainty.

We organize our paper as follows: A method section specifies forward and adjoint mantle convection equations, our assumptions for misfit function and state estimate of present mantle heterogeneity, as well as the numerical modeling code, and dynamic topography calculations. We then present retrodictions in the results section, and end our paper with a discussion and conclusion.

2. Method

Mantle convection is an initial condition problem, that is an appropriate *starting condition* for past mantle structure is needed to model its past evolution. The latter is not merely unknown, but unknowable through direct observations. However, direct information on the present-day mantle state can be obtained from seismic imaging and other means. In principle Monte Carlo approach (e.g., *Sambridge and Mosegaard*, 2002) can sample the space of initial conditions to produce a final state that resembles the current mantle state. Computational cost, however, makes this unfeasible for all but simplified 2-D convection studies (*Atkins et al.*, 2016).

Instead we use an optimization technique to recover past deep Earth structure. We minimize the difference between the current mantle state and its predictions from a geodynamic model by computing the model derivative relative to the initial state. Obtaining the derivative by finite differencing is impractical, owing to the large number of parameters (on the order of 10^{10}) in modern geodynamic Earth models. The adjoint method provides the derivative in a computationally efficient way (*Bunge et al.*, 2003).

Given a *misfit function* χ that quantifies the difference between the present mantle state T^E and its model prediction T^F , we compute the total (Fréchet) derivative $\mathcal{D}_{T^I}\chi(T^F)(\Delta T^I)$, that is the sensitivity of χ relative to changes ΔT^I in the initial condition T^I . The Fréchet derivative is obtained from the solution of an ancillary set of so-called *adjoint equations*. Starting from a *first-guess* initial condition T_0^I , we compute a *first-guess* final state T_0^F . The adjoint equations allow us to obtain an updated initial condition T_1^I , from which in turn we produce a new final state T_1^F . Forward and adjoint equations are solved iteratively until the misfit function χ is minimized. Thus, we require forward and their corresponding adjoint mantle convection equations, an estimate of the

present mantle state, a misfit function χ to compare the modelled and inferred mantle state, and a computational model to execute the simulations.

2.1. Forward equations

The forward mantle convection equations embody conservation principles for mass, momentum and energy. To account for mantle compressibility effects, we solve them in the anelastic-liquid approximation (*Jarvis and McKenzie, 1980*), in a time interval $I := [t_0, t_1]$ within a spherical shell V (i.e., the Earth’s mantle) with boundary $\partial V = S \cup C$, where S denotes the Earth’s surface and C the CMB:

$$\begin{aligned} \nabla \cdot (\rho_r v) &= 0, \\ \nabla \cdot \left[\eta \left(\nabla v + (\nabla v)^T - \frac{2}{3} (\nabla \cdot v) \mathbf{1} \right) \right] - \nabla P + \alpha \rho_r g (T_{av} - T) &= 0, \\ \partial_t T + \gamma T \nabla \cdot v + v \cdot \nabla T - \frac{1}{\rho_r c_v} \{ \nabla \cdot (k \nabla T) + \tau : \nabla v \} + H &= 0, \end{aligned}$$

where v is the velocity, ρ_r is the radial density profile, η is the viscosity, P is the pressure, α is the thermal expansivity, g is the acceleration of gravity, T is the temperature while T_{av} is its layer-average value, γ is the Grüneisen parameter, c_v is the specific heat capacity at constant volume, k is the thermal conductivity, τ is the deviatoric stress tensor and H is the rate of radiogenic heat production.

The plate motion history model of *Seton et al. (2012)* is imposed on S through a time-dependent velocity boundary condition on the momentum equation (*Bunge et al., 1998*) to assure convergence (*Vynnytska and Bunge, 2014*), and C is treated as free-slip (i.e., no horizontal shear stress), while the energy equation employs Dirichlet boundary conditions (i.e., fixed temperatures) on $\partial V = S \cup C$.

2.2. Adjoint equations

The corresponding adjoint equations for compressible mantle flow have been derived by *Ghelichkhan and Bunge (2016)*. They employ so-called adjoint variables for three fields, termed adjoint velocity ϕ , pressure λ and temperature Ψ , in analogy to the forward velocity, pressure and temperature fields:

$$\begin{aligned} \nabla \cdot \phi &= 0, \\ \nabla \cdot \left[\eta (\nabla \phi + (\nabla \phi)^T) \right] + \Psi \nabla T - \rho_r \nabla \lambda - 2 \nabla \cdot \left(\frac{\Psi}{\rho_r c_v} \tau \right) &= 0, \\ \partial_t \Psi + v \cdot \nabla \Psi - (\gamma - 1) \Psi \nabla \cdot v + \nabla \cdot \left(k \nabla \left(\frac{\Psi}{\rho_r c_v} \right) \right) + \alpha \rho_r g \cdot \phi &= \partial_{T^F} \hat{\chi}(T^F). \end{aligned}$$

Adjoint and forward equations are similar, the main difference being in the adjoint energy equation. This equation involves a change of sign for the diffusion term, which makes the equation unconditionally stable to integration back in time. The adjoint energy equation also includes a source term related to the

misfit function that acts as a final time condition. The adjoint equations, too, require a set of boundary conditions in addition to this final time condition. A detailed explanation of the equations, variables and boundary conditions is given by *Ghelichkhan and Bunge (2016)*.

2.3. Inferences on the present-day thermal state of the mantle

Inferences on the thermo-chemical state of Earth’s mantle are complex (see *Davies et al., 2015b*, for a review). Here we follow recent studies (*Schuberth et al., 2009b,a; Davies et al., 2012*) and assume a homogeneous pyrolitic mantle composition for the sake of simplicity. The latter is consistent with the geographical distribution of hotspots (*Austermann et al., 2014; Davies et al., 2015a*) and implies a predominantly thermal origin for large-scale mantle seismic anomalies. We compute the stable mineral assemblage and its average mechanical and thermodynamical properties at each p-T point from the thermodynamically self-consistent model of mantle mineralogy by *Stixrude and Lithgow-Bertelloni (2011)* (hereafter called SLB2011). Figure 2A reports the S-wave velocity as a function of pressure and temperature as predicted by SLB2011. The sharp changes of seismic velocity in the transition zone are due to abrupt changes in phase proportions, most importantly the phase transitions of olivine to wadsleyite around 410 km depth and of ringwoodite to bridgmanite around 660 km depth. They are also a distinct feature of 1D seismic reference models (e.g., *Dziewonski and Anderson, 1981; Kennett et al., 1995*).

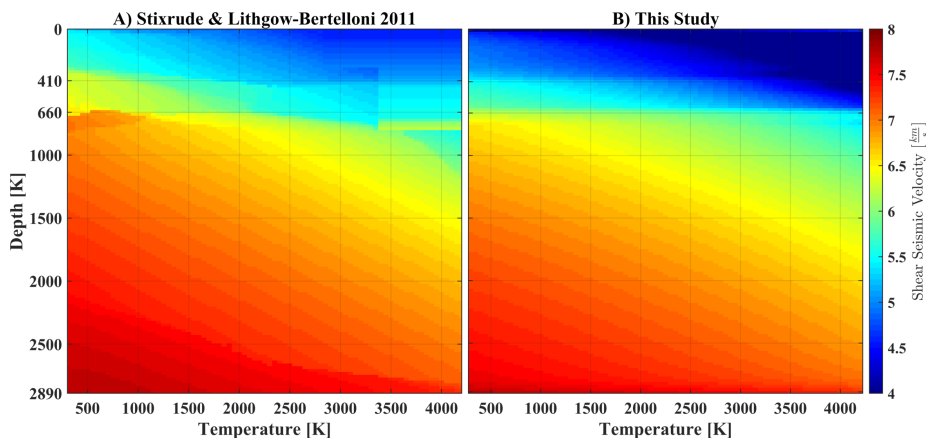


Figure 2: **A)** Shear wave velocity as a function of depth and temperature obtained from the thermodynamic model of mantle mineralogy SLB2011 (*Stixrude and Lithgow-Bertelloni, 2011*) assuming a pyrolitic composition with six components: CaO , FeO , Na_2O , Al_2O_3 , MgO and SiO_2 . The major phase transitions are marked by abrupt changes of seismic velocity with temperature and depth. **B)** The shear velocity, temperature and depth mapping used in this study. The variation of seismic velocity and temperature is based on an $exp(v_S) - T$ fit best representing the SLB2011 model at each depth.

These phase transitions have a non-zero Clapeyron slope, i.e. their depth

depends on temperature, so that the related seismic discontinuities display a thermally-induced topography. While the latter can be investigated with SS and PP precursors (*Deuss, 2009*), and while global tomographic models are beginning to incorporate them (*Simmons et al., 2012*), current uncertainties in seismic and mineralogical models induce some bias (*Styles et al., 2011*) by mapping phase topography into unphysical temperature jumps in the transition zone. We mitigate this effect with a smoothed version of SLB2011 (Figure 2B) that parameterizes the temperature dependence of S-wave velocities as $\exp(v_S) = \alpha^{vs} T + \beta^{vs}$, with the parameters α^{vs} and β^{vs} obtained from a best-fit of the mineralogically-derived S-wave velocities at each depth. The choice of our functional form provides an excellent fit in regions with no phase transitions (e.g., the mid mantle), while removing artificial temperature jumps in the transition zone. Importantly, our approach preserves the non-linear mapping of seismic velocity to temperature that is expected for a compressible mantle, and assures a smooth temperature field over the thermally induced phase jumps. Figure 2B shows the resulting S-wave velocity as a function of pressure and temperature. A comparison with Figure 2A confirms that our method, while avoiding jumps in the temperature field, keeps the overall seismic velocity variations consistent with SLB2011.

Figure 3A reports α^{vs} as a function of depth. Near surface values are ≈ -0.025 and reach up to -0.2 at the CMB, indicating a more non-linear seismic velocity to temperature relation at depth, as expected for a compressible mantle. We convert temperature to density by adopting the same approach, and report α^ρ at each depth in Figure 3B. While there is a depthwise increase of α^ρ similar to α^{vs} , its absolute value is smaller by an order of magnitude, implying a milder non-linearity between temperature and density.

Current uncertainties in the thermodynamic parameters on which mineralogical models are based imply a 3% (5%) uncertainty in the absolute value of P (S) wave speed, and a corresponding uncertainty of 1000–1500 degrees in absolute temperature (*Connolly and Khan, 2016*). We work around this limitation by tying the lateral density variations to the radial density profile of PREM (*Dziewonski and Anderson, 1981*), and a reference thermal profile (see Figure 5A) obtained from a recent mantle circulation model (*Nerlich et al., 2016*).

2.4. Misfit function

Mantle flow retrodictions minimize a misfit function χ , which measures the distance between the present-day mantle heterogeneity state predicted from a geodynamic model and estimated from a seismic tomography. Commonly one obtains χ from the L_2 norm of the grid point difference (*Bunge et al., 2003; Horbach et al., 2014; Ghelichkhan and Bunge, 2016*) between model and reference state. However, tomographic imaging filters small-wavelength features relative to heterogeneity predicted for a vigorously convecting mantle (e.g., *Schuberth et al., 2009a*), so that dynamically significant mantle structure may either

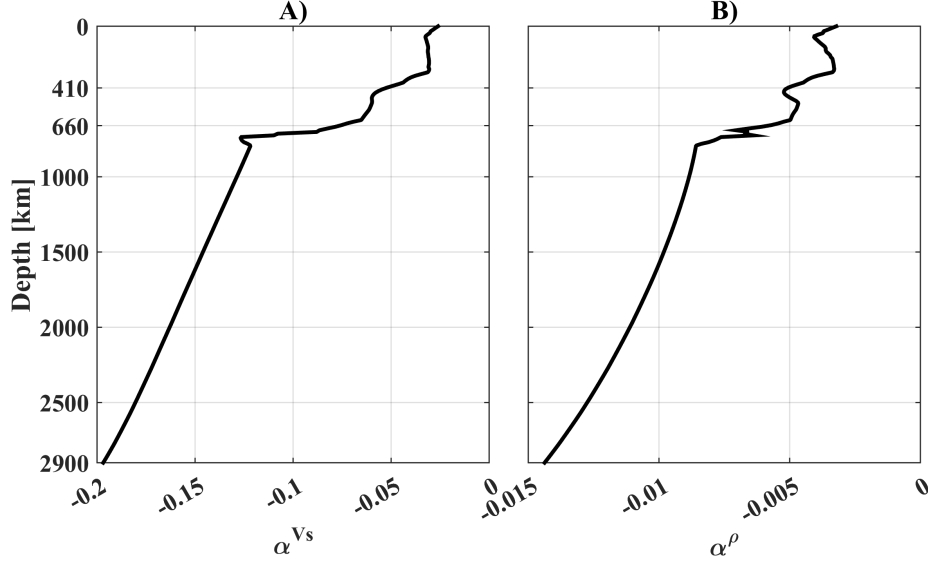


Figure 3: **A)** α^{v_s} , obtained by a $\exp(v_s) - T$ regression on model SLB2011 at each depth. **B)** α^ρ , obtained by a $\exp(\rho) - T$ regression on model SLB2011 at each depth. While $\rho - T$ relation is almost linear, the non-linearity in $v_s - T$ is non-negligible for a compressible mantle.

be smeared or absent, as noted before. We take into account this intrinsic scale-length difference by expanding the modeled and tomographic heterogeneity fields over spherical harmonics Y_{lm} , defining χ as:

$$\chi = \int_{R_b}^{R_a} \frac{1}{2} \sum_{l=0}^{l_{\max}} \sum_{m=-l}^l (T_{lm}^F(r, t_1) - T_{lm}^E(r))^2 r^2 dr = \int_{R_b}^{R_a} \sum_{l,m} \hat{\chi} r^2 dr, \quad (1)$$

where R_b and R_a denote the CMB and surface radii, respectively, l_{\max} refers to the maximum degree retained by the expansion, and T_{lm} lists the spherical harmonic coefficient of T of degree l and order m , i.e.:

$$T_{lm}(r) = \int_{\Omega} T(r, \theta, \phi) Y_{lm}(\theta, \phi) d\Omega. \quad (2)$$

The chain rule yields the Fréchet derivative of χ w.r.t. the initial condition T^I :

$$\mathfrak{D}_{T^I} \chi(\Delta T^I) = \int_{R_b}^{R_a} \sum_{l,m} \left(\mathfrak{D}_{T_{lm}^F} \hat{\chi} \mathfrak{D}_{T^F} T_{lm}^F \mathfrak{D}_{T^I} T^F(\Delta T^I) \right) r^2 dr.$$

The first term is calculated as the explicit derivative of $\hat{\chi}$ w.r.t. T_{lm} , while the second corresponds to a spherical harmonic decomposition operating on the third term, as seen from eq. (2). Thus we rewrite the total Fréchet derivative as:

$$\mathfrak{D}_{T^I} \chi(\Delta T^I) = \int_V \mathfrak{D}_{T^I} T^F(\Delta T^I) \tilde{T} dV = \left\langle \mathfrak{D}_{T^I} T^F(\Delta T^I), \tilde{T} \right\rangle,$$

Table 1: Model parameters employed in this study

Parameter	Value	Units
Surface temperature	300	K
CMB temperature	4200	K
Internal heating rate	6×10^{-12}	W kg ⁻¹
Inner radius	3480	km
Outer radius	6370	km
Density	4500	kg
Reference viscosity	5×10^{19}	Pa s
Thermal expansivity (surface)	3.3×10^{-5}	K ⁻¹
Thermal expansivity (CMB)	1.2×10^{-5}	K ⁻¹
Thermal conductivity	3	W m ⁻¹ K ⁻¹
Specific heat capacity	1000	J kg ⁻¹ K ⁻¹
Grüneisen parameter	1.1	
Rayleigh number	2.1×10^8	

where we use \tilde{T} as the shorthand to denote the truncation of the spherical harmonic re-summation of the full difference between modeled and estimated temperature fields. The choice of the maximum degree l_{\max} is determined by the spectral characteristics of the seismic tomography. For the present study we have selected $l_{\max} = 20$. Figure 4 compares the evolution of the harmonic norm defined in eq. (1) and of the L_2 norm (Horbach *et al.*, 2014) of the end states obtained in an inversion driven by the harmonic misfit.

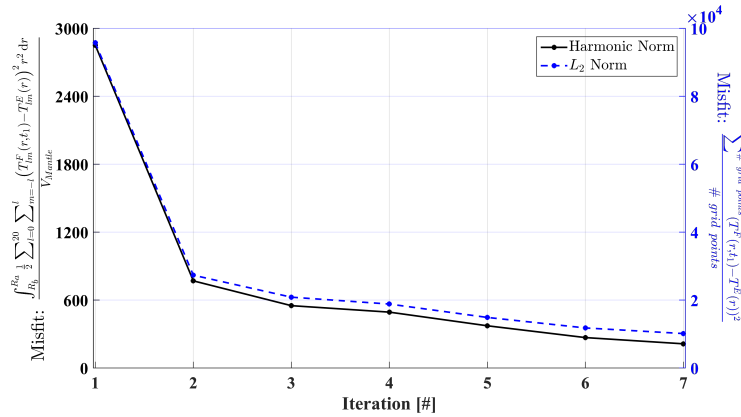


Figure 4: Black solid line: misfit reduction over successive iterations of forward and adjoint calculation driven by the harmonic misfit defined in eq. (1). Blue dashed line: misfit norm for the same end states (inconsistently) quantified with an L_2 norm (Horbach *et al.*, 2014). Note that a misfit reduction of $\approx 80\%$ is achieved in the first few iterations.

2.5. Mantle Convection Model

We solve the forward and adjoint equations using the 3-D spherical parallel finite element code TERRA (Bunge *et al.*, 1996, 1997), with calculations performed on the *SuperMUC* facility of the Leibniz Supercomputing Centre (LRZ, www.lrz.de) and a local compute cluster dedicated to large-scale geophysical modeling (Oeser *et al.*, 2006). Our high resolution mesh discretises Earth’s mantle with more than 670 million finite element nodes, corresponding to a grid point resolution of 11 km radially, and horizontally of 14 km at the surface, decreasing to half that value at the CMB. Consequently, our mantle convection simulations are performed at Earthlike convective vigor, employing a basal-heating Rayleigh number (based on the volume-averaged mantle viscosity) of 2×10^8 . Importantly, the high convective vigor allows us to assimilate past plate motions at their true velocity, alleviating the need in earlier Mantle Circulation Models (e.g.: Bunge *et al.*, 1998) to re-scale model time to Earth time. A list of model parameters is given in Table 1.

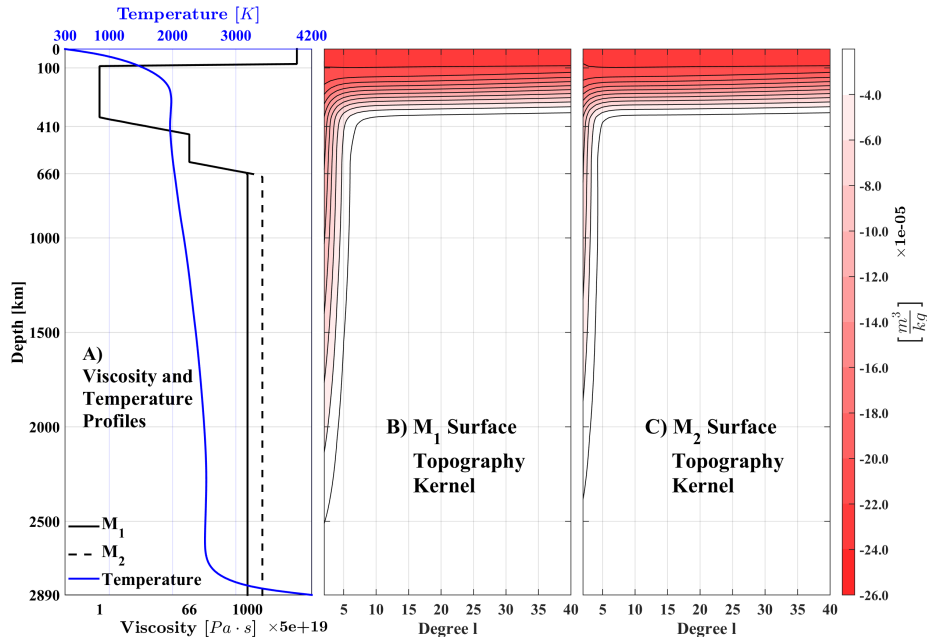


Figure 5: A) radial viscosity profiles (black solid and dashed lines) used in this study and reference radial temperature profile (blue curve) used for the visualization of temperature anomalies, as well as for the conversion to and from temperature (cf. section 2.3). B) Surface topography kernels computed with the viscosity profile M_1 . C) Surface topography kernels computed with the viscosity profile M_2 . The kernels are similar, with only long wavelength contribution from lower mantle density anomalies. The difference in lower mantle viscosity between M_1 and M_2 , however, results in a reduced contribution of the lower mantle for M_2 . The kernels are computed using 4500 kg/m^3 as the effective density contrast between the mantle and free-air.

Our radial viscosity profile involves a stiff lithosphere and lower mantle, a

Table 2: Summary of reconstructed histories

Model Name	Tomography Model	Viscosity
AM ₁	<i>Afanasiev et al. (2015)</i>	M ₁
SM ₁	<i>Simmons et al. (2015)</i>	M ₁
AM ₂	<i>Afanasiev et al. (2015)</i>	M ₂
SM ₂	<i>Simmons et al. (2015)</i>	M ₂

thin sub-lithospheric channel of low viscosity and a moderate-viscosity transition zone (see Figure 5A). While geoid and GIA studies (e.g., *Richards and Hager, 1984; Mitrovica, 1996*) require the radial mantle viscosity to reach a minimum in the upper mantle, the amount of viscosity reduction and the thickness of the low-viscosity layer are not well constrained, as noted before, in part because a trade-off exists between these two parameters in geoid and GIA studies (*Paulson and Richards, 2009; Schaber et al., 2009*). A range of observations from seismic anisotropy (e.g., *Debayle et al., 2005*), seismic imaging (*Colli et al., 2013; French et al., 2013; Rickers et al., 2013*), oceanic intraplate seismicity (*Wiens and Stein, 1985*) and ocean ridge bathymetry (*Buck et al., 2009*), however, points towards a thin asthenosphere channel of much reduced strength, motivating us to account explicitly for this layer in our models. Important geodynamic implications of the low viscosity channel include an increased lithosphere-asthenosphere coupling (*Höink et al., 2012*), a correlation of horizontal and vertical plate motions (*Colli et al., 2014; Iaffaldano and Bunge, 2015*), and fast asthenosphere flow velocities of some tens of cm/yr (*Weismüller et al., 2015*).

Two different viscosity profiles, M₁ and M₂ (see Figure 5A), allow us to test the sensitivity of our models to variations in deep mantle viscosity. A lower one of 5×10^{22} Pa·s is based on studies of Earth’s rotational variations and deglaciation-induced true polar wander (*Matsuyama et al., 2010; Nakada et al., 2015*), while a higher value of 10^{23} Pa·s is motivated by the speed of sinking slabs (*Butterworth et al., 2014*). As well, we explore two different estimates of the present-day mantle heterogeneity state, derived from two recent tomographic models obtained with different methods and datasets. The model of *Afanasiev et al. (2015)* is based on the assimilation of a global model (S20RTS, *Ritsema et al., 1999*) and a number of regional submodels into a consistent multiscale model. Of particular relevance for our present discussion is the assimilation of submodels for the South Atlantic (*Colli et al., 2013*) and Europe (*Fichtner et al., 2013*), which were obtained with a full-waveform inversion of regional surface waves and body waves, thus yielding a relatively high resolution in the upper mantle. The model by *Simmons et al. (2015)*, instead, employs regional and teleseismic body-wave traveltimes data and, in our region of interest, reaches its maximum resolution in the lower mantle. The two models can thus be considered as complementary in their strengths and weaknesses. For example, the model by *Simmons et al. (2015)* has arguably a more detailed image of the African large low shear velocity province (LLSVP), while the model by *Afanasiev et al. (2015)* provides a better image of the upper mantle under Iceland. Combining

the two viscosity profiles with the two heterogeneity estimates we present here a total of four model cases, summarized in Table 2.

2.6. Dynamic Topography: Semi-Analytical Solutions

We compute dynamic topography in our models using the well established formalism of *Richards and Hager* (1984) in its compressible form (*Panasjuk et al.*, 1996; *Thoraval and Richards*, 1997) and assuming a free-slip (no horizontal stress) boundary condition. The solutions are commonly presented through so-called sensitivity kernels $K_l(r)$, relating dynamic topography to a unit mass anomaly of given wavelength and depth $\delta\rho_{lm}$, so that the spherical harmonic component δh_{lm} of the dynamic topography is computed in the spectral domain by a radial integration over the mantle thickness:

$$\delta h_{lm} = \int_{R_{CMB}}^{R_E} \delta\rho_{lm} K_l(r) dr, . \quad (3)$$

The kernel $K_l(r)$ in eq. (3) depends on radial viscosity variations and is inversely proportional to the effective density contrast between the mantle and the overlying medium (e.g., free-air or water). Figures 5-B/C report the surface dynamic topography kernels for the two radial viscosity profiles M_1 and M_2 shown in Figure 5-A.

In all our dynamic topography calculations we disregard all density anomalies shallower than 200 km, as they are related to either the thermal cooling of oceanic lithosphere or the continent-ocean dichotomy (*Lithgow-Bertelloni and Silver*, 1998).

3. Results

3.1. Hemispherical scale

Using the theory presented before, we invert for the heterogeneity state of Earth’s mantle 40 Myrs ago. Figure 6 shows the retrodicted structure obtained after six adjoint iterations by assuming the viscosity profile M_1 and using the seismic tomography of *Afanasiev et al.* (2015) as a representation of the present-day mantle state (i.e.: model AM_1). Each column shows 3-D snapshots of the modeled temperature anomalies, velocity field and surface dynamic topography through time at 5 Myrs intervals.

The lower mantle under Africa and Europe (Figure 6, column A) is characterized by the slow evolution of a large positive temperature anomaly, consistent with a purely thermal interpretation of the LLSVP imaged by seismic tomographers. The hot anomaly is flatter and has a larger lateral extent at 40 Ma than at present-day. In time the hot anomalies near the CMB gather along a median axis under Africa striking in a northwest-southeast direction. From there they rise towards the surface, in particular beneath southern-central Africa and in

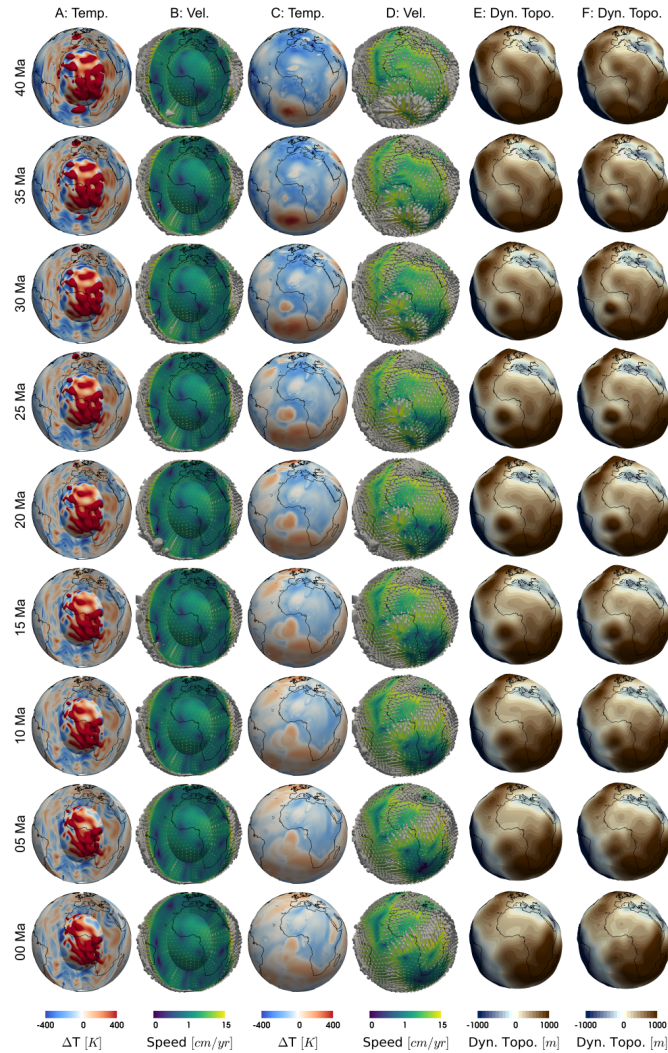


Figure 6: 3-D views, centered on the African hemisphere, showing successive snapshots of the reconstructed mantle history AM₁, obtained by using the tomographic model of *Afanasiev et al. (2015)* to estimate the present-day reference thermal state of the mantle. Column 1: temperature anomalies (with respect to a fixed radial profile (see Figure 5) on a color scale saturated at -400 K and +400 K, together with the isosurface for +400 K. This view is obtained by cutting out a 90° wedge from the mantle, centered on the prime meridian, with the inner and outer spherical boundaries corresponding to 2790 km depth and 270 km depth, respectively. Column 2: mantle flow speed on a logarithmic scale between 0.1 and 15 cm/yr, with grey arrows representing the complete velocity vector. Same view as column 1. Column 3: temperature anomalies (same as column 1) in the asthenosphere (270 km depth). Column 4: flow velocities (same as column 2) in the asthenosphere. Column 5: dynamic topography (deformation is exaggerated 400×) expanded up to $l_{\max} = 20$. Column 6: same as column 5 but expanded up to $l_{\max} = 40$.

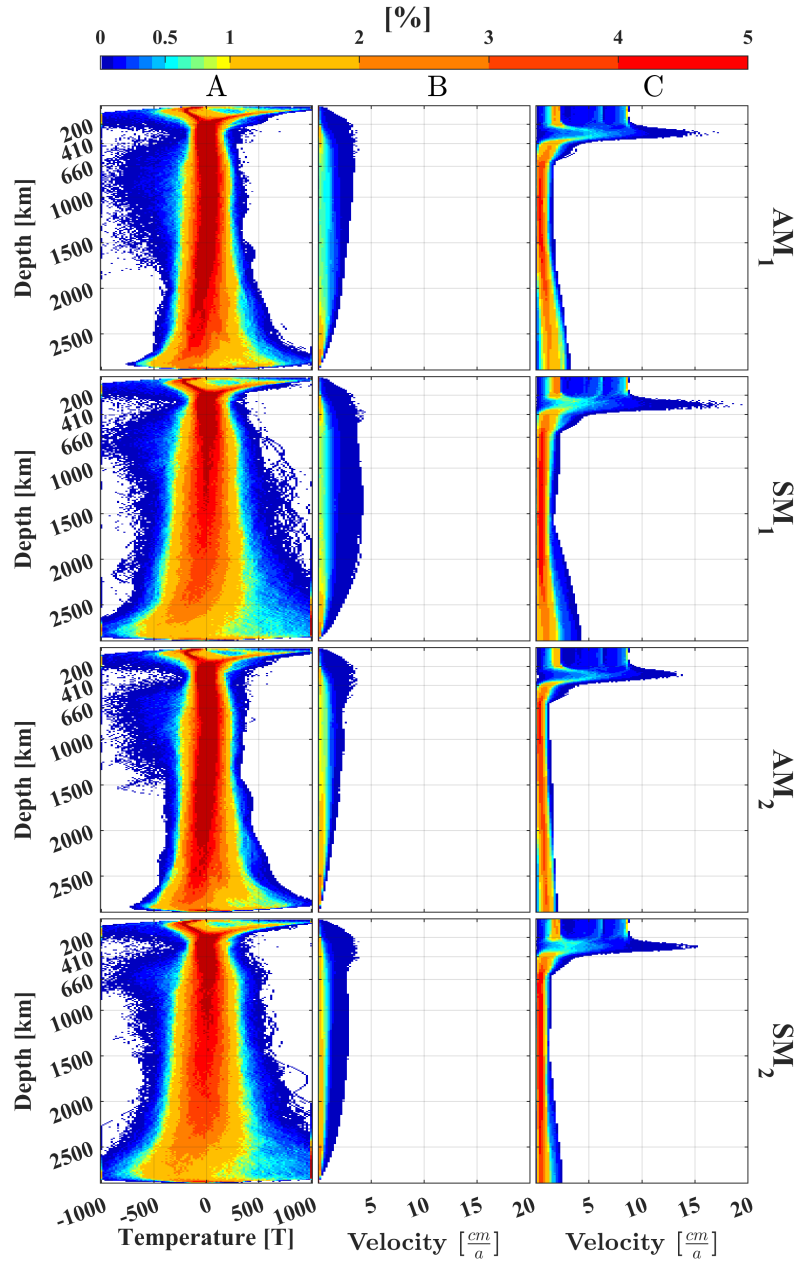


Figure 7: Histograms of temperature anomalies (first column), radial velocities (second column) and tangential velocities (third column) for the modeled present-day state of the mantle obtained with model AM₁ (first row), SM₁ (second row), AM₂ (third row) and SM₂ (fourth row). The logarithmic color scale shows percentage of grid points per binned interval.

the North Atlantic, while the upwelling underneath the Afar region is characterized by lower temperatures. Large-scale downwellings are associated with the closure of the Tethys Ocean, the opening of the Scotia Sea and the subduction of the Nazca slab. The return flow they excite contributes to the evolution of thermal anomalies near the CMB and closes the African convective cell. The temperature anomalies entrained by major upwellings and downwellings are advected by around 1000 km, giving an average sinking speed for slabs of ≈ 2.5 cm/yr.

Lower mantle flow velocities (Figure 6, column B) are smaller than plate velocities (RMS velocity is 1.2–1.6 cm/yr, with maximum velocities around 3 cm/yr) going from mainly tangential near the CMB to predominantly radial in the mid-mantle (see Fig 7B and C). The global convection pattern is characterized by a convection cell ten-thousand km in scale, with downward flow driven by the Tethys, Nazca and South Sandwich Islands subductions and upward flow under Southern and Western Africa and the North Atlantic. The velocity field is spatially quite variable, with many regions characterized by negligible velocities as indicated by blue colors. But it remains relatively constant in time. Looking at the upper rim of the vertical transects one appreciates the marked flow velocity increase in the transition zone and upper mantle that owes to the viscosity reduction in these layers.

The temperature field in the asthenosphere, above 410 km (see Figure 6, column C) is characterized by the arrival and subsequent lateral spreading of hot anomalies coming from the lower mantle. This results in more homogeneous asthenospheric temperatures at present-day compared to both the initial condition at 40 Ma and the lower mantle (cf. the narrowing of the temperature histogram between 200 and 400 km depth in Figure 7A). The retrodiction features the arrival of a major thermal anomaly in the South Atlantic near Tristan da Cunha just before 40 Ma and another one near Iceland around 25 Ma. Other minor pulses of hot material, reminiscent of splash-plumes (*Davies and Bunge, 2006*) arrive around 35–30 Ma in the Atlantic and around 5 Ma in the Afar region.

In the asthenosphere the velocity field (see Figure 6, column D) reverts to predominantly horizontal, and increases in speed by about an order of magnitude compared to the mantle below. The relatively steady subduction of the Nazca and Tethys slabs excites a strongly convergent velocity field, with little spatial and temporal variability in these regions. The arrival of hot anomalies in the intervening regions, instead, excites strongly divergent and temporally variable velocity fields. Northern and Northeastern Africa experience a fairly stable flow directed towards the Tethys subduction zone. Western Africa instead is caught between westward flow coming from a mantle upwelling west of the Canary Islands and northward flow induced by the upwelling between present-day Saint Helena and Ascension. Southern Africa experiences marked north-westward and northward flow due to an upwelling near Tristan da Cunha until about 15 Ma, when the flow gradually transitions to southward under the

influence of the pronounced upwelling under Eastern and Central Africa. Overall, asthenosphere velocities are on average faster than plate velocities (RMS speed 7–9 cm/yr, max speed 30–50 cm/yr) albeit highly spatially variable.

The dynamic topography (Figure 6, columns E–F) reflects the evolution of mantle thermal anomalies. It is characterized by broad swells over Africa, the Atlantic and the Indian oceans, while South America is significantly depressed. A large swath of ocean going from the Cape basin in the west to the Mascarene basin in the east is predicted to be elevated by about 1.5–2.5 km at 40 Ma, slowly decreasing in elevation to about 1.2 km at present-day. Africa’s southern and eastern portions are stable at around 700 m elevation, until a major dome rises to 1.2 km during the last 15 Ma, causing a general westward tilt of the continent. This dome also uplifts the southwestern part of Arabia, while the northeastern part of the peninsula subsides under the influence of the Tethys subduction. Northern Africa slowly subsides and flattens. A prominent swell in the central North Atlantic migrates north-eastward towards the Azores, peaking ≈ 25 Ma and then subsides, while further north a dome develops over northern Greenland, migrating southward and peaking ≈ 20 Ma over Iceland.

Figure 8 shows an alternate mantle flow retrodiction, obtained by using the seismic model of *Simmons et al.* (2015) as our representation for the present-day mantle state (i.e.: model SM₁), and acting as the final state condition applied in the adjoint procedure. General character and behavior of this reconstruction resemble the previous one, with a sluggish lower mantle characterized by the assemblage of the African LLSVP and fast unsteady asthenosphere flow. However, already at the global scale both models yield notable differences. The temperature field of SM₁ displays smaller-scale structures (cf. columns A–B of Figure 6 and 8) and larger amplitudes (see Figure 7A) relative to AM₁, in particular in the lower mantle. This is a direct consequence of the different seismic structures imaged by the two tomographies. The different buoyancy field, in turn, is reflected in the flow field: SM₁ shows a velocity field more variable in space and in time. Although the RMS velocities of both models are similar, their velocity distribution differs, with SM₁ having a flatter distribution. This is particularly noticeable in the lower mantle, where a larger number of gridpoints have small (<0.5 cm/yr) or large (>2.5 cm/yr) speeds.

The corresponding dynamic topography (Figure 8, columns E–F) has lower amplitudes and shorter wavelength features. Some global features, such as the rise of a high dome in southeastern Africa and the uplift of central Europe, show qualitative similarities with the dynamic topography evolution of AM₁. Both models, however, make different predictions. For instance, the large topographic swell in the Indian and southern South Atlantic ocean is substituted by isolated domes over the Mascarene basin and Kerguelen. A dome centered on the Canary islands subsides until 25 Ma, when it starts to rise again. Northeastern Africa is predicted to be low around 40 Ma and subsequently gets uplifted.

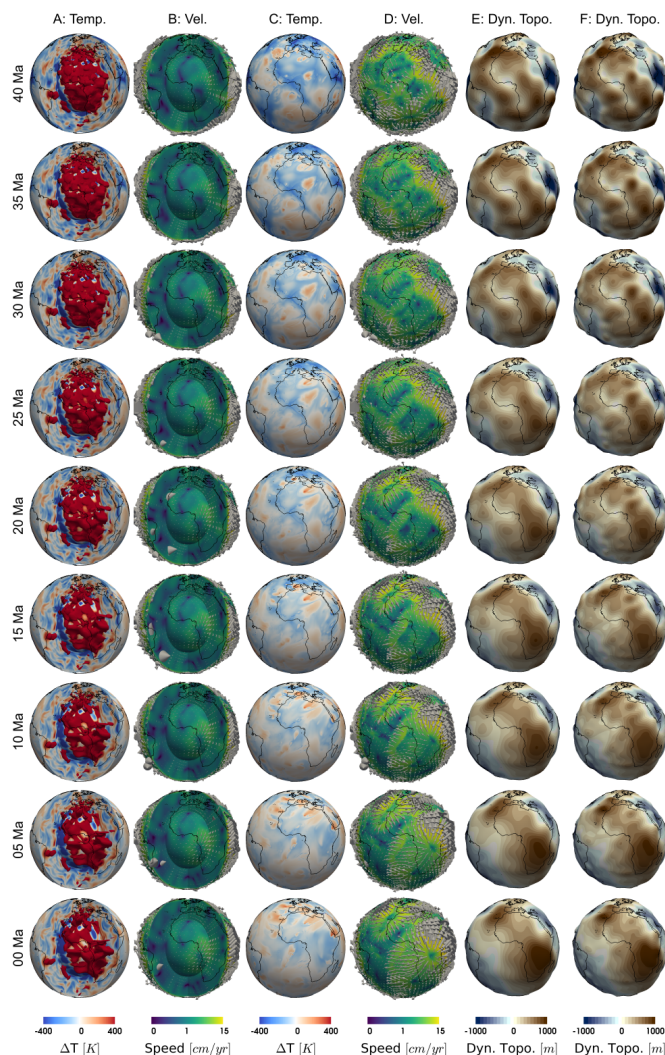


Figure 8: Same as Figure 6, but for the reconstructed mantle history SM_1 , obtained by using the tomographic model of *Simmons et al.* (2015) to estimate the present-day reference thermal state of the mantle.

Figure 9 shows a mantle flow retrodiction obtained by keeping the present-day heterogeneity structure of AM_1 , but using a stiffer lower mantle viscosity profile (see Figure 5A) characterized by a twofold (compared to AM_1) increase in lower mantle viscosity (i.e. model AM_2). In this case the overall velocity field is similar in direction to AM_1 . But the lower mantle flow velocities are reduced by about one-third, in line with an expected scaling of $v \propto \eta^{-2/3}$ (*Davies*, 1999), while the upper mantle speeds are reduced only $\approx 10\%$. Thus the overall evolution of the lower mantle in AM_2 is to first order a slowed version of AM_1

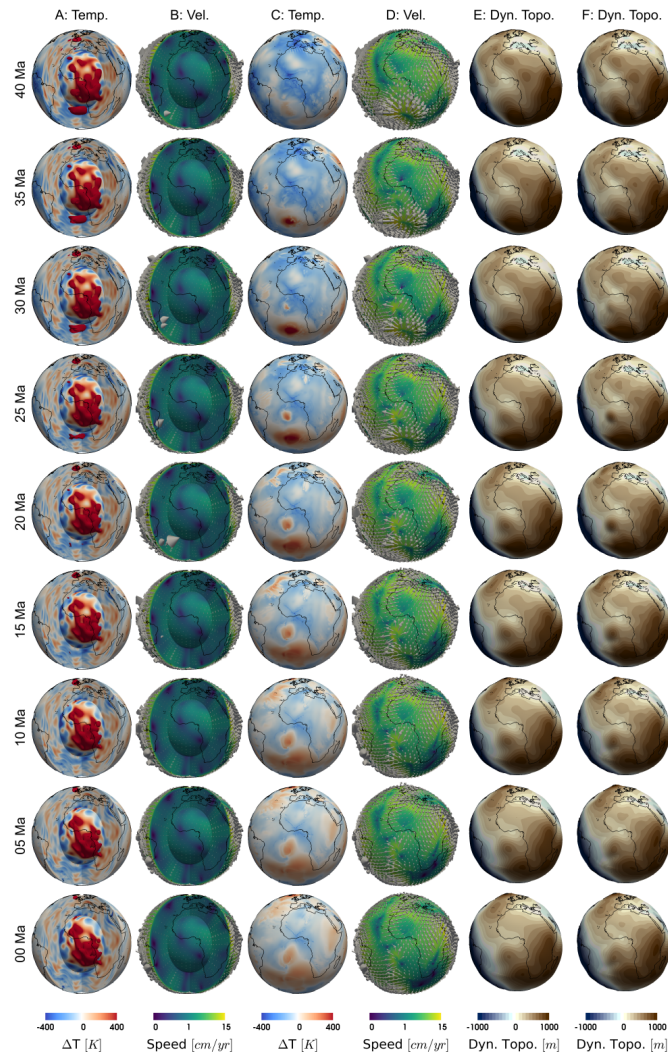


Figure 9: Same as Figure 6, but for the reconstructed mantle history AM₂, obtained by assuming a more viscous lower mantle.

(cf. e.g. Figure 6A at 25 Ma with Figure 9A at 40 Ma). The asthenosphere, instead, presents differences both in terms of velocity and thermal structure. The major difference, however, comes from the predicted dynamic topography. The long wavelength contribution from the lower mantle is smaller, as expected from the kernels (cf. Figure 5B and C), and less variable in time. The upper mantle contribution, while similar in amplitude, instead has changed somewhat in location. For example the central African dome is now shifted northwards some 2000 km, and the Iceland dome only rises in the last 15 Ma.

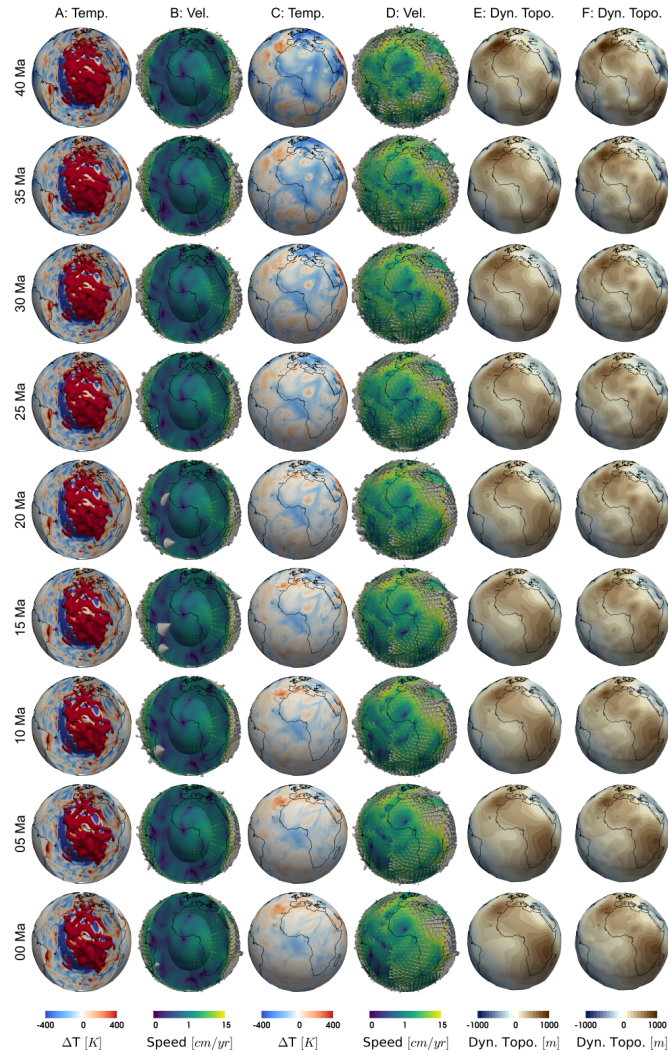


Figure 10: Same as Figure 8, but for the reconstructed mantle history SM₂, obtained by assuming a more viscous lower mantle.

Similar considerations apply to SM₂ (see Figure 10): Lower mantle velocities are reduced and they generate smoother and larger-scale convection cells compared to SM₁. Thermal anomalies in the lower mantle are advected by a shorter distance, reaching the asthenosphere at different times and in different locations relative to the retrodiction from SM₁. The resulting dynamic topography is characterized by smaller amplitudes, with a peak-to-peak amplitude of less than two kilometers for most of the reconstructed time.

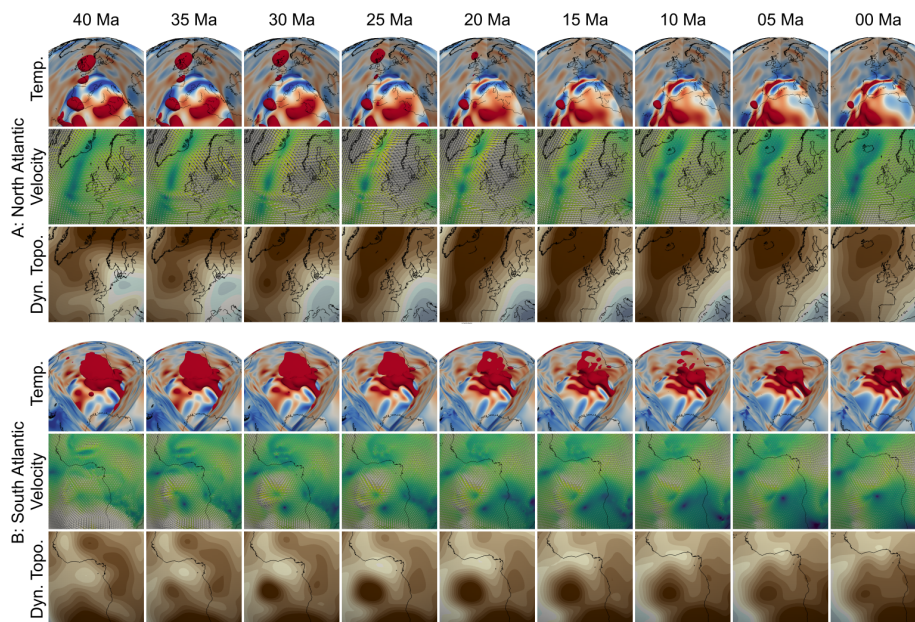


Figure 11: Regional views of the mantle history reconstructed with model AM_1 (cf. Figure 6). A) North Atlantic region. B) South Atlantic region. The first row of each panel shows 3D temperature anomalies of the sublithospheric mantle. The second row shows the velocity field at 270 km depth. The third row shows the predicted dynamic topography expanded up to spherical harmonic degree 40.

3.2. Regional scale

The differences between the four models are more pronounced at the regional scale. Zooming into the North and South Atlantic regions, Figures 11–14 show the evolution of the sublithospheric temperature anomalies, the asthenospheric velocity field and the dynamic topography for the four different reconstructions AM_1 , SM_1 , AM_2 and SM_2 .

In the North Atlantic, AM_1 (Figure 11A) predicts the rise of a hot thermal anomaly under eastern Greenland. It reaches the transition zone ≈ 25 Ma and quickly spreads in the asthenosphere, mostly in a direction perpendicular to the ridge axis. It is worth noting that upon rising the hot anomaly loses excess temperature, as expected (*Bunge, 2005*), and when it reaches the asthenosphere the excess temperature is below +400 K. By 10 Ma the supply of hot material to the upper mantle stops, while a new hot anomaly forms at the mantle base. At 40 Ma the asthenosphere east of the mid-atlantic ridge flows mostly westward, except for the fennoscandian region, where the flow is directed to the south and southwest. The arrival of the hot anomaly under Iceland causes increased westward flow, peaking ≈ 25 Ma and then decreasing in amplitude. The surface evolution mirrors the flow history, and develops a large positive dynamic topography over east Greenland and Iceland, which peaks ≈ 20 Ma

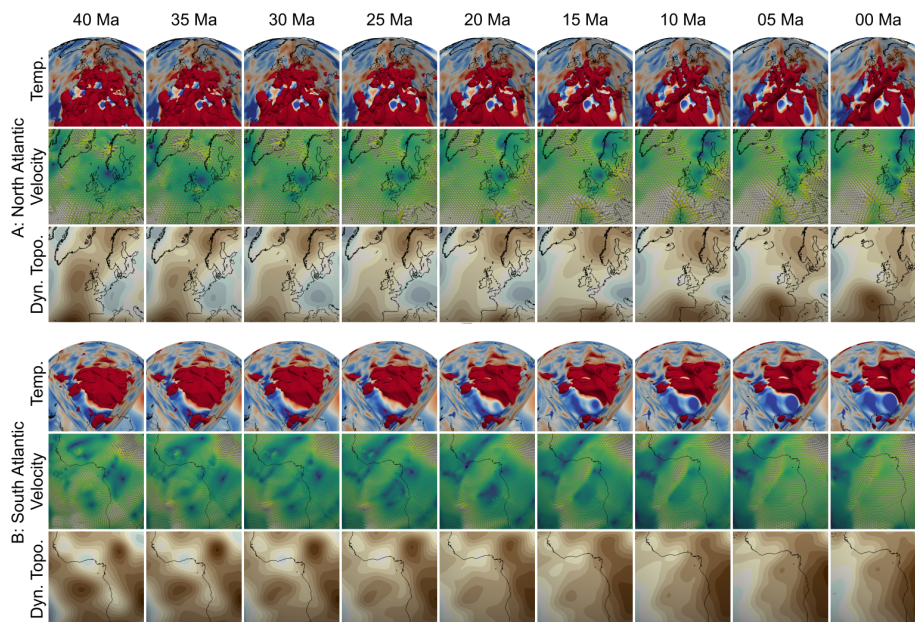


Figure 12: Regional views of the mantle history reconstructed with model SM_1 (cf. Figure 8). A) North Atlantic region. B) South Atlantic region. The first row of each panel shows 3D temperature anomalies of the sublithospheric mantle. The second row shows the velocity field at 270 km depth. The third row shows the predicted dynamic topography expanded up to spherical harmonic degree 40.

and decreases afterwards. In Scandinavia the topographic gradient changes from mostly north-south ≈ 40 Ma to mostly west-east from 15 Ma. Central Europe is slightly lowstanding until ≈ 25 Ma, but is gradually uplifted as the hot material from Iceland spreads laterally in the asthenosphere.

The South Atlantic (Figure 11B) is characterized by the evolution of the African LLSVP in the lower mantle, the spreading and cooling of a strong hot anomaly around Tristan da Cunha, together with the arrival of a hot anomaly 35 Ma between the islands of Ascension and Saint Helena. The coast of West Africa remains stable in a slightly elevated state, while the northern part of the Congo basin and the Western Sahara are reconstructed as being elevated by some hundred meters at 40 Ma but subside thereafter. The western Congo basin and northern Angola, instead, remain elevated in a persistent dome even when the region to the north subsides. The southern and southeastern parts of the African plate are reconstructed with a substantial highstand at 40 Ma, but subside to around 1 km elevation by present-day. Overall, southern Africa experiences a change from a northward tilt at 40 Ma to being gently westward tilted at present-day.

Model SM_1 predicts a markedly different history of asthenospheric flow and dynamic topography. In the North Atlantic (Figure 12A) the Iceland upwelling

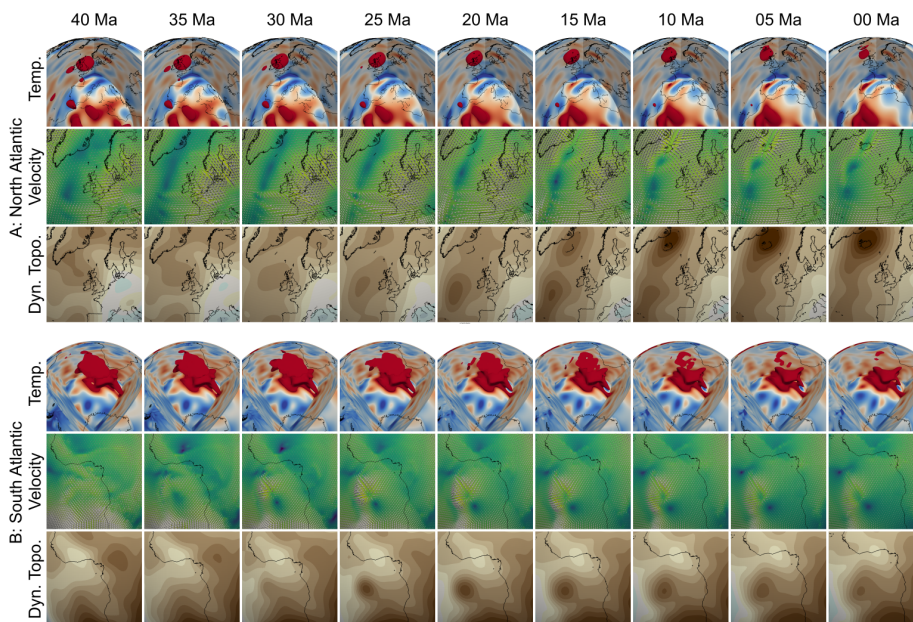


Figure 13: Regional views of the mantle history reconstructed with model AM_2 (cf. Figure 9). A) North Atlantic region. B) South Atlantic region. The first row of each panel shows 3D temperature anomalies of the sublithospheric mantle. The second row shows the velocity field at 270 km depth. The third row shows the predicted dynamic topography expanded up to spherical harmonic degree 40.

is less pronounced and shifted eastward. The asthenosphere beneath Scandinavia is very slow, while central and eastern Europe experience faster southwestern flow. Stronger upwellings in the Iberia-Morocco region cause pronounced northwardly directed asthenospheric flow in southwestern Europe. The resulting dynamic topography is reduced in amplitude and noticeably different in its evolution. Central Europe undergoes an initial phase of moderate subsidence, before being uplifted in the last 15 Ma, the British Islands experience a tilt reversal, and Greenland is stable at a moderate elevation, with only minor subsidence occurring in its northeastern part.

Also in the South Atlantic region, SM_1 (Figure 12B) is characterized by smaller-scale mantle thermal anomalies. There is no major upwelling that corresponds to Tristan da Cuna, and the hot anomaly between Ascension and Saint Helena arrives earlier and decays faster. The large-scale lower mantle hot anomaly rises by about a thousand km in 40 Ma, reaching the transition zone by present-day and exciting a divergent asthenosphere flow of growing strength, centered under East Africa. This is particularly visible in the last ≈ 10 Ma, with large-scale westward velocities beneath central-western Africa and the Southeast Atlantic ocean, while the asthenosphere under southern Africa flows southwards. The domes that characterize the dynamic topography of the oceanic basin at 40 Ma subside in time, while central and southern Africa get

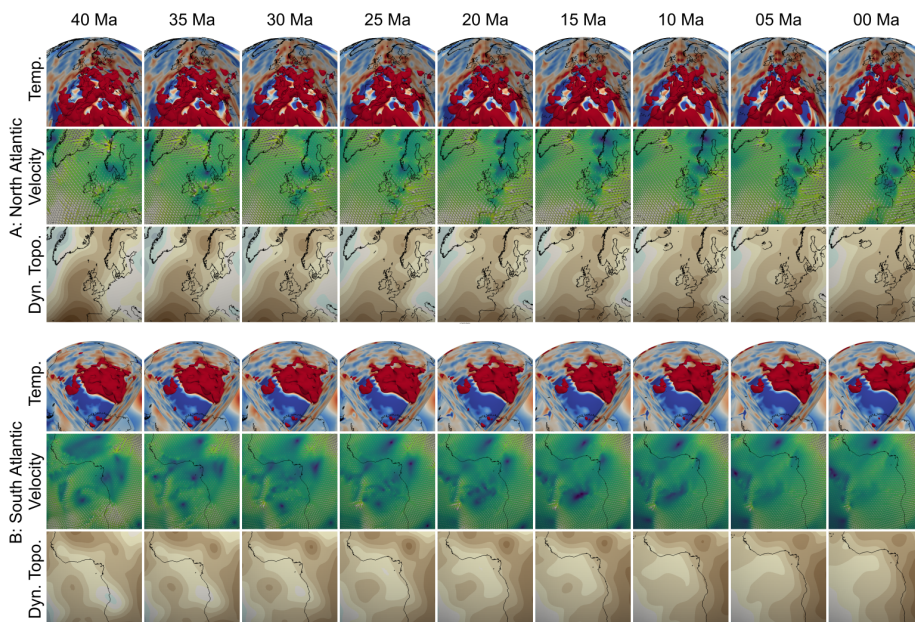


Figure 14: Regional views of the mantle history reconstructed with model SM_2 (cf. Figure 10). A) North Atlantic region. B) South Atlantic region. The first row of each panel shows 3D temperature anomalies of the sublithospheric mantle. The second row shows the velocity field at 270 km depth. The third row shows the predicted dynamic topography expanded up to spherical harmonic degree 40.

uplifted. This results in a large-scale east-west topography gradient south of the equator that mirrors the westward asthenospheric flow. North of the equator there are two prominent doming features, one in northern Mali and a second in Cameroon. Both reach their maximum elevation ≈ 35 Ma and then subside slowly.

The evolution of the North Atlantic realm reconstructed from AM_2 (Figure 13A) shows the rise of a hot anomaly under present-day Iceland, and overall south-eastward flow velocities in the asthenosphere under Europe. Unlike AM_1 , the hot anomaly rises more slowly and is partially still present in the lower mantle today. Asthenosphere flow velocities are lower and spatially more variable until 10 Ma, when the hot anomaly reaches the transition zone and the flow field underneath Iceland becomes strongly divergent. The corresponding dynamic topography dome is smaller, more localized, and uplifts only in the last 20 Ma, peaking at 5 Ma. Prior to 10 Ma the major topographic feature is a dome off the western coast of Ireland. An analogous dome existed in AM_1 . But it was dwarfed by the Icelandic dome. Continental Europe undergoes a moderate uplift and is characterized by small topographic gradients throughout the reconstructed history. In the South Atlantic, instead, AM_2 implies a similar evolution to AM_1 of lower mantle anomalies. The dome over Cameroon and the

northern Congo basin is now more prominent and persistent, while the region to the south is affected throughout the reconstructed period by a large-scale dome centered to the south east. Reconstructed asthenosphere velocities and dynamic topography are also similar to those obtained from AM₁, albeit with smaller amplitudes (cf. Figure 11B and Figure 13B).

SM₂ predicts the main upwelling region in the North Atlantic to be located along the coast of Norway and in the southern North Sea (see Figure 14A). Under continental Europe the flow is distinctly eastward, albeit with local variability, while in the oceanic realm the asthenosphere flows westward largely undisturbed. The central North Atlantic is predicted to be elevated at 40 Ma. It subsequently subsides, in particular off the coast of Ireland. A small dome develops in the southern North Sea, expands southeastward, and causes uplift in most of continental Europe. For the South Atlantic (see Figure 14B) SM₂ predicts the flow field be more variable at 40 Ma, with multiple upwelling centers both in the oceanic realm and under Africa. But this evolves into a more regular pattern characterized by the predominance of a major upwelling under East Africa and westward flow in the asthenosphere, decreasing in magnitude towards the West. This is reflected in the evolution of dynamic topography: it shows a number of small domes both on land and in the ocean at 40 Ma, and subsequently is dominated by a large-scale dome centered on the Great Lakes region.

3.3. Local scale

Figure 15 reports dynamic topography trends for selected locations (cf. Figure 1). In a few places (Berlin and, to a lesser extent, New York) all four models give similar results both in terms of amplitude and of time variation. In most cases, however, the reconstructed histories are sensibly different. The choice of the present-day estimate frequently dictates the main differences in amplitude and trend, while the viscosity profile only causes minor differences in amplitude and negligible differences in trend. This, however, is not a general rule, as can be seen for Atlanta, where the different viscosity profile has the biggest impact, changing both amplitudes and trends in a coherent way for both present-day estimates. In Thorshavn models SM₁ and SM₂ both predict an extremely similar history of stability at a modest highstand, while models AM₁ and AM₂ predict completely different trends.

4. Discussion

Enabled by the dramatic growth of computational capabilities, the adjoint method and numerical differentiation techniques are becoming important tools for geophysical models - in, for example, seismology (*Tromp et al.*, 2005; *Fichtner et al.*, 2006a,b), and simulations of tectonics (*Iaffaldano et al.*, 2007) or the geodynamo (*Fournier et al.*, 2010) - to compute gradient information relative to model parameters. In geodynamics the method allows one to derive retrodictions of past mantle flow, by providing gradient information of a current relative

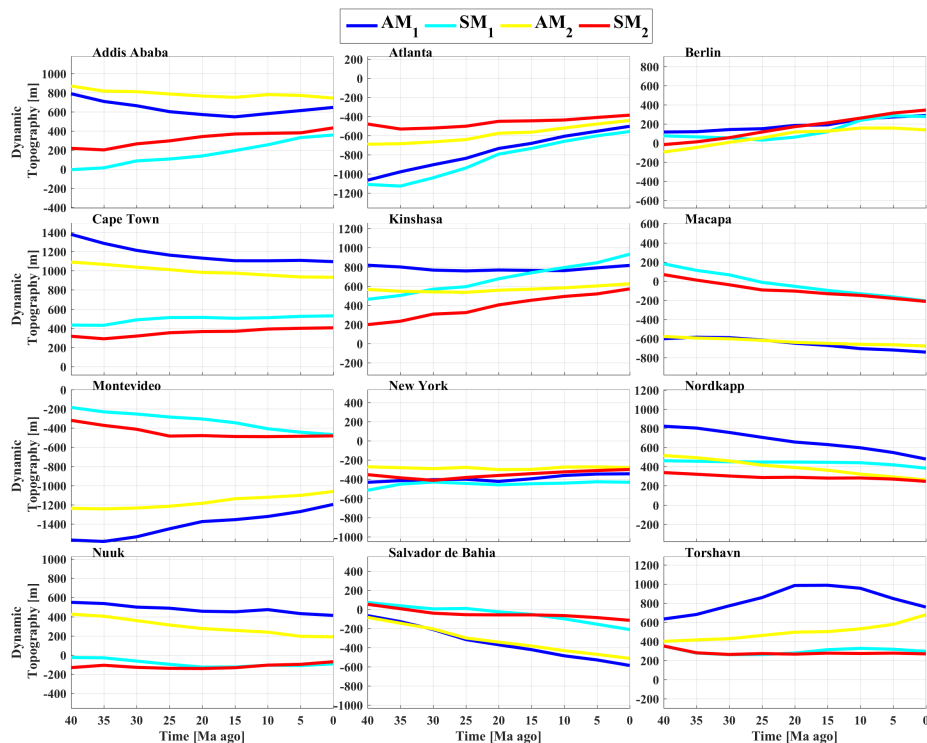


Figure 15: Dynamic topography history at a number of selected locations. Different models predict discordant histories in terms of both amplitudes and trends at most locations.

to an earlier system state, so that mantle flow models can be tested against constraints gleaned from the geologic record. Our high resolution models employ ≈ 670 million finite element nodes, and each retrodiction requires about two months of compute time on 2048 processors of the *SuperMUC* facility of the LRZ. The high numerical resolution is needed to simulate global mantle flow at Earth-like convective vigor and to incorporate a thin low viscosity layer (LVZ) that has been advocated (*Paulson and Richards, 2009*).

While theory and uniqueness properties of geodynamic inversions are well understood (*Horbach et al., 2014; Vynnytska and Bunge, 2014; Ghelichkhan and Bunge, 2016*), their application to real Earth studies is still in its infancy, and limited by observational constraints. For instance, the existence of non-tectonic vertical motions has been recognized early on by geologists (*Stille, 1919*). But only recent years have seen sustained attention to constraining the patterns and timings of these vertical motions (e.g.: *Praeg et al., 2005; Japsen et al., 2006; Stoker and Shannon, 2005; Roberts and White, 2010; Guillocheau et al., 2012; Wilson et al., 2014; Dressel et al., 2015; Stanley et al., 2015*), finding that they are characterized by relatively short spatial and temporal scales (*Hartley*

et al., 2011; *Japsen et al.*, 2012a; *Parnell-Turner et al.*, 2014; *Hoggard et al.*, 2016), and implying an active role of the LVZ. Our retrodictions account for the LVZ, and an important result of the simulations is that they support a form of dynamic topography having a significant component of small-scale doming induced by active mantle upwellings, and evolving on timescales of a few tens Myrs, in agreement with geologic inferences of present-day and past dynamic topography (*Burke and Gunnell*, 2008; *Hartley et al.*, 2011; *Hoggard et al.*, 2016).

4.1. Mantle flow velocities

One consequence of the LVZ is a marked change of the velocity field between the lower mantle and the asthenosphere (see Figure 7), with asthenospheric flow being predominantly horizontal and significantly faster than both lower mantle and plate speeds. This agrees with previous geodynamic studies on the behavior of a thin asthenosphere channel (*Höink et al.*, 2011; *Weismüller et al.*, 2015), and with the need to provide an active flow driving component beneath the lithosphere to satisfy the tectonic force balance (*Iaffaldano and Bunge*, 2015).

Although the convective planform of our models is dominated by large aspect-ratio cells, the asthenosphere flow is highly variable in space and time. This implies strong regional and temporal changes in basal drag of the lithosphere, providing a potential mechanism for rapid plate motion variations (*Colli et al.*, 2014), and perhaps going some way in explaining rapid changes in hotspot motion (*Tarduno et al.*, 2009). In our models the variability is a product of small-scale anomalies in the temperature field, and occurs even for simple depth-dependent viscosity profiles. Since the rheology of asthenosphere material is expected to be both temperature and stress dependent (*Karato and Wu*, 1993), asthenosphere flow variability could be more pronounced in the real Earth.

Lower mantle flow velocities are predicted to be small in our models, as expected from the existence of a hotspot reference frame (*Duncan and Richards*, 1991). Viscosity profile M_1 results in slab sinking rates of 2 cm/yr or more, slightly larger than values inferred from seismic images and reconstructions of past plate configurations (*Butterworth et al.*, 2014; *Domeier et al.*, 2016). M_2 , characterized by a larger viscosity in the lower mantle and chosen on the basis of previous work on slab sinking rates (*Butterworth et al.*, 2014), yields rates of ≈ 1.5 cm/yr. The latter is more in line with the previously cited estimates. M_2 also yields reduced temporal variations in dynamic topography, so that improved geologic constraints on the rate of non isostatic vertical motion could improve our knowledge of the mantle viscosity structure.

4.2. Tomographic resolution and mantle convection lengthscales

Uncertainties in our retrodictions stem from the limited resolution of seismic tomography. Small scale structure of a few hundred kilometers is currently not well imaged, and even at scales of thousands of kilometers, where the seismic anomaly patterns are reasonably well constrained, their amplitudes remain uncertain to at least a factor of ≈ 2 (*Zaroli et al.*, 2013). This, combined with

uncertainties of current mineralogical models, leaves room for substantial inaccuracy in the conversion of seismic to thermal and density heterogeneity. To address this problem, more work is needed on the geodynamic forward problem, i.e., going from the thermal state predicted by a mantle convection model to an elastic structure, and computing seismic observables that can be tested explicitly with data (*Schuberth et al.*, 2009a, 2012, 2015).

The fact that mantle flow retrodictions rely on the inferences of seismic imaging is illustrated by our choice of two tomographic models for this study. Each seismic model implies a different present-day mantle state estimate and, consequently, a different flow history. For example, AM₁ and AM₂ predict Cenozoic doming in the North Atlantic centered on Iceland, while SM₁ and SM₂ predict smaller doming centered just off the coast of central Norway. The deviation owes to different upper mantle structure imaged by the two seismic studies. The effect of different lower mantle structure is appreciated by considering the doming of central and eastern Africa, with SM₁ and SM₂ predicting a smaller dome with more short-wavelength features. Thus while the overall character of our models agrees with first order geologic inferences of present and past dynamic topography in the Atlantic realm, it is clear that detailed model interpretations are premature at present (see Figure 15).

4.3. Misfit function

Current seismic resolution limits have another consequence: they induce a mismatch between the heterogeneity lengthscales generated by geodynamic modelling and those imaged by seismic tomography that influences the cost function. Imposing a pointwise misfit guarantees a strong misfit reduction (*Horbach et al.*, 2014), albeit at the cost that the reconstructed initial state may have unnatural features, such as a lack of small-scale structures or overly thick thermal boundary layers. We mitigate this effect through a misfit function that decomposes the temperature field in spherical harmonics, so that only long-wavelength heterogeneity differences enter the adjoint inversion. Consequently, short-wavelength features in our models are not explicitly constrained. But neither are they actively penalized. In other words, they are constrained implicitly by the physics of the mantle convection model through our choices for the relevant parameters.

The mismatch between model heterogeneity scales and scales imaged by seismic tomography has implications for the computed dynamic topography. Using merely the seismically inferred long-wavelength features of mantle heterogeneity produces an artificial lack of short-wavelength structure. Including the model generated short-wavelength structure, instead, honors additional information inherent in the assumed modeling parameters, albeit not explicitly constrained by observation. To clearly indicate this choice, we report the dynamic topography resulting from density anomalies up to harmonic degree $l=20$ (Figures 6 and 8–10, column E), i.e., from the *explicitly* constrained part of the density field, and from density anomalies up to harmonic degree $l=40$ (*ibid.*, column F),

i.e. with part of the density field constrained *implicitly* by the flow dynamics.

4.4. Viscosity structure

Earth’s rheology is not well known and a range of contrasting choices can be made. Our choice of lower mantle viscosity profiles (i.e., M_1 and M_2) explores a small range, and implies reduced sensitivity to lower-mantle long-wavelength structure for M_2 (see Figure 5). This lowers, as expected, the overall amplitude of dynamic topography and increases the relative contribution of small-scale upper mantle structures (cf. Figures 6, 9, 8 and 10), suggesting that retrodictions are sensitive even to modest variations in the assumed rheology. Thus further constraints on Earth’s dynamic topography (its amplitude and rates of change) evolution are needed as an important information for geodynamic models. However, it must be noted, that such comparison is not straightforward, for a number of reasons. Our present work focuses on the long-wavelength (> 1000 km) end of the dynamic topography spectrum. But mantle convection may excite dynamic topography down to scales of a few hundreds of km. Dynamic topography variations at all scales can cause surface and rock uplift/subsidence both directly and, together with rock exhumation/burial, indirectly through erosion and sedimentation caused by changes in accommodation space. This would likely result in a perturbation of the local isostatic and flexural state as well, thus causing additional indirect vertical motion. As a consequence, we note that there is no simple one-to-one relationship between dynamic topography variations and rock or surface vertical motion, in particular at the local scale at which geologic observations are made and where the effects of additional factors such as climate and lithology are most important.

4.5. Plate motion history

We finish by noting that our analysis assumes no error in the surface velocity field, i.e., the past plate motion model, that is used over the assimilation period. In reality our knowledge of past plate motions is not perfect. One may reduce measurement noise and improve the temporal resolution of relative plate motions via Bayesian analysis (*Iaffaldano et al.*, 2012), but further assumptions, such as the choice of a reference frame, contribute to uncertainty in past plate motion models, especially as one goes further back in time (*Shephard et al.*, 2012). This should be accounted for, if retrodictions are to be extended further back in time.

5. Conclusion

We have applied the adjoint method to high resolution global geodynamic Earth models with ≈ 670 million finite element nodes, retrodicting the thermal heterogeneity state of Earth’s mantle 40 Ma ago, for two different seismic tomography models and two mantle viscosity profiles. Because mantle flow retrodictions assimilate the horizontal component of the surface velocity field

(i.e., they use a plate reconstruction model as an input in the inversion for past mantle flow) they make testable predictions on the evolution of dynamic topography. We find that the retrodicted history of mantle convection and dynamic topography in our simulations is sensitive to the assumptions about the present-day mantle state and its rheology, suggesting that mantle flow retrodictions obtained from adjoint modeling can provide powerful constraints on the assumptions of structural and rheologic parameters of Earth models, by comparing their predicted dynamic topography evolution to constraints gleaned from the geologic record. We conclude that improved constraints on non-isostatic vertical motion of Earth's surface, provided, for instance, by basin analysis, seismic stratigraphy, landform studies, or the sedimentation record will play an important role in our understanding of the recent mantle flow history.

6. Acknowledgments

The authors thank N. Simmons and M. Afanasiev for providing their tomographic models. This work was funded in part by the German Research Foundation (DFG) within the priority program SPP 1375-SAMPLE. The authors acknowledge the Gauss Centre for Supercomputing e.V. (www.gauss-centre.eu) for funding this project by providing computing time on the GCS Supercomputer SuperMUC at Leibniz Supercomputing Centre (LRZ, www.lrz.de).

Afanasiev, M., D. Peter, K. Sager, S. Simute, L. Ermert, L. Krischer, and A. Fichtner (2015), Foundations for a multiscale collaborative Earth model, *Geophys. J. Int.*, *204*, 3958, doi:10.1093/gji/ggv.

Afonso, J. C., J. Fullea, W. L. Griffin, Y. Yang, A. G. Jones, J. A. D. Connolly, and S. Y. O'Reilly (2013), 3-D multiobservable probabilistic inversion for the compositional and thermal structure of the lithosphere and upper mantle. I: a priori petrological information and geophysical observables, *Journal Of Geophysical Research: Solid Earth*, *118*, 25862617, doi:10.1002/jgrb.50124.

Amante, C., and B. W. Eakins (2009), ETOPO1 1 Arc-Minute Global Relief Model: Procedures, Data Sources and Analysis, *Tech. rep.*, National Geophysical Data Center, NOAA, doi:10.7289/V5C8276M.

Amodeo, J., B. Schuberth, H.-P. Bunge, P. Carrez, and P. Cordier (2015), On the role of thermal heterogeneities on the rheology of mgo under conditions of the earths lower mantle, *Physics of the Earth and Planetary Interiors*, *242*, 18, doi:10.1016/j.pepi.2015.02.008.

Atkins, S., A. P. Valentine, P. J. Tackley, and J. Trampert (2016), Using pattern recognition to infer parameters governing mantle convection, *Physics of the Earth and Planetary Interiors*, *257*, 171186, doi:10.1016/j.pepi.2016.05.016.

Austermann, J., and G. Iaffaldano (2013), The role of the zagros orogeny in slowing down arabia-eurasia convergence since 5 ma, *Tectonics*, *32*(3), 351363, doi:10.1002/tect.20027.

- Austermann, J., B. T. Kaye, J. X. Mitrovica, and P. Huybers (2014), A statistical analysis of the correlation between large igneous provinces and lower mantle seismic structure, *Geophys. J. Int.*, *197*(1), 1–9, doi:10.1093/gji/ggt500.
- Autin, J., M. Scheck-Wenderoth, M. Loegering, Z. Anka, E. Vallejo, J. Rodriguez, F. Dominguez, D. Marchal, C. Reichert, R. di Primio, and et al. (2013), Colorado Basin 3D structure and evolution, Argentine passive margin, *Tectonophysics*, *604*, 264279, doi:10.1016/j.tecto.2013.05.019.
- Becker, T. W., and L. Boschi (2002), A comparison of tomographic and geodynamic mantle models, *Geochemistry, Geophys. Geosystems*, *3*(1), N/A, doi:10.129/2001GC000168.
- Braun, J. (2010), The many surface expressions of mantle dynamics, *Nature Geoscience*, *3*(12), 825833, doi:10.1038/ngeo1020.
- Buck, W. R., C. Small, and W. B. F. Ryan (2009), Constraints on asthenospheric flow from the depths of oceanic spreading centers: The east pacific rise and the Australian-antarctic discordance, *Geochem. Geophys. Geosyst.*, *10*(9), n/an/a, doi:10.1029/2009gc002373.
- Bunge, H., and M. A. Richards (1992), The backward-problem of plate tectonics and mantle convection, (abstract), *Eos Trans. AGU*, *73*(14), 281, spring Meeting suppl.
- Bunge, H., M. A. Richards, and J. R. Baumgardner (1996), Effect of depth-dependent viscosity on the planform of mantle convection, *Nature*, *379*(6564), 436–438, doi:10.1038/379436a0.
- Bunge, H., M. A. Richards, and J. R. Baumgardner (1997), A sensitivity study of three-dimensional spherical mantle convection at 10^8 Rayleigh number: Effects of depth-dependent viscosity, heating mode, and an endothermic phase change, *J. Geophys. Res.*, *102*(B6), 11,991, doi:10.1029/96JB03806.
- Bunge, H., C. R. Hagelberg, and B. J. Travis (2003), Mantle circulation models with variational data assimilation: inferring past mantle flow and structure from plate motion histories and seismic tomography, *Geophys. J. Int.*, *152*(2), 280–301, doi:10.1046/j.1365-246X.2003.01823.x.
- Bunge, H.-P. (2005), Low plume excess temperature and high core heat flux inferred from non-adiabatic geotherms in internally heated mantle circulation models, *Phys. Earth Planet. Inter.*, *153*(1–3), 3–10, doi:10.1016/j.pepi.2005.03.017.
- Bunge, H.-P., and J. H. Davies (2001), Tomographic images of a mantle circulation model, *Geophysical Research Letters*, *28*(1), 77–80, doi:10.1029/2000GL011804.

- Bunge, H. P., M. A. Richards, C. Lithgow-Bertelloni, J. R. Baumgardner, S. P. Grand, and B. A. Romanowicz (1998), Time scales and heterogeneous structure in geodynamic earth models, *Science*, *280*(5360), 91–95, doi:10.1126/science.280.5360.91.
- Burke, K., and Y. Gunnell (2008), *The African Erosion Surface: A Continental-Scale Synthesis of Geomorphology, Tectonics, and Environmental Change Over the Past 180 Million Years*, Memoir (Geological Society of America), Geological Society of America.
- Butterworth, N., A. Talsma, R. Mller, M. Seton, H.-P. Bunge, B. Schubert, G. Shephard, and C. Heine (2014), Geological, tomographic, kinematic and geodynamic constraints on the dynamics of sinking slabs, *Journal of Geodynamics*, *73*, 1 – 13, doi:http://dx.doi.org/10.1016/j.jog.2013.10.006.
- Cammarano, F., S. Goes, P. Vacher, and D. Giardini (2003), Inferring upper-mantle temperatures from seismic velocities, *Physics of the Earth and Planetary Interiors*, *138*(3-4), 197222, doi:10.1016/s0031-9201(03)00156-0.
- Colli, L., A. Fichtner, and H. Bunge (2013), Full waveform tomography of the upper mantle in the South Atlantic region: Imaging a westward fluxing shallow asthenosphere?, *Tectonophysics*, *604*, 26–40, doi:10.1016/j.tecto.2013.06.015.
- Colli, L., I. Stotz, H. Bunge, M. A. Smethurst, S. Clark, G. Iaffaldano, A. Tassara, F. Guillocheau, and M. C. Bianchi (2014), Rapid South Atlantic spreading changes and coeval vertical motion in surrounding continents: Evidence for temporal changes of pressure-driven upper mantle flow, *Tectonics*, *33*(7), 1304–1321, doi:10.1002/2014TC003612.
- Colli, L., H.-P. Bunge, and B. S. A. Schubert (2015), On retrodictions of global mantle flow with assimilated surface velocities, *Geophysical Research Letters*, *42*(20), 83418348, doi:10.1002/2015gl066001.
- Connolly, J. A. D., and A. Khan (2016), Uncertainty of mantle geophysical properties computed from phase equilibrium models, *Geophysical Research Letters*, *43*(10), 50265034, doi:10.1002/2016gl068239.
- Dahlen, F. A., S.-H. Hung, and G. Nolet (2000), Frechet kernels for finite-frequency traveltimes—i. theory, *Geophys. J. Int.*, *141*(1), 157–174, doi:10.1046/j.1365-246X.2000.00070.x.
- Davies, D., S. Goes, and M. Sambridge (2015a), On the relationship between volcanic hotspot locations, the reconstructed eruption sites of large igneous provinces and deep mantle seismic structure, *Earth and Planetary Science Letters*, *411*, 121130, doi:10.1016/j.epsl.2014.11.052.
- Davies, D. R., S. Goes, J. H. Davies, B. S. A. Schubert, H.-P. Bunge, and J. Ritsema (2012), Reconciling dynamic and seismic models of earth’s lower

- mantle: The dominant role of thermal heterogeneity, *Earth Planet. Sci. Lett.*, *353–354*(0), 253–269, doi:10.1016/j.epsl.2012.08.016.
- Davies, D. R., S. Goes, and H. C. P. Lau (2015b), *Thermally Dominated Deep Mantle LLSVPs: A Review*, pp. 441–477, Springer International Publishing, Cham, doi:10.1007/978-3-319-15627-9_14.
- Davies, G. F. (1999), *Dynamic Earth: Plates, Plumes and Mantle Convection*, Cambridge University Press, doi:10.1017/CBO9780511605802.
- Davies, G. F., and M. A. Richards (1992), Mantle convection, *The Journal of Geology*, *100*(2), 151–206.
- Davies, J. H., and H.-P. Bunge (2006), Are splash plumes the origin of minor hotspots?, *Geology*, *34*(5), 349–352, doi:10.1130/G22193.1.
- Debayle, E., and Y. Ricard (2012), A global shear velocity model of the upper mantle from fundamental and higher Rayleigh mode measurements, *J. Geophys. Res. Solid Earth*, *117*(10), 1–24, doi:10.1029/2012JB009288.
- Debayle, E., B. L. N. Kennett, and K. Priestley (2005), Global azimuthal seismic anisotropy and the unique plate-motion deformation of Australia, *Nature*, *433*, 509–512, doi:10.1038/nature03247.
- Deuss, A. (2009), Global Observations of Mantle Discontinuities Using SS and PP Precursors, *Surv. Geophys.*, *30*(4-5), 301–326, doi:10.1007/s10712-009-9078-y.
- Domeier, M., P. V. Doubrovine, T. H. Torsvik, W. Spakman, and A. L. Bull (2016), Global correlation of lower mantle structure and past subduction, *Geophysical Research Letters*, *43*, 4945–4953, doi:10.1002/2016GL068827.
- Dressel, I., M. Scheck-Wenderoth, M. Cacace, B. Lewerenz, H.-J. Götze, and C. Reichert (2015), Reconstruction of the southwestern african continental margin by backward modeling, *Marine and Petroleum Geology*, *67*, 544–555, doi:10.1016/j.marpetgeo.2015.06.006.
- Duncan, R. A., and M. A. Richards (1991), Hotspots, mantle plumes, flood basalts, and true polar wander, *Reviews of Geophysics*, *29*(1), 31–50, doi:10.1029/90RG02372.
- Dziewonski, A. M., and D. L. Anderson (1981), Preliminary reference Earth model, *Phys. Earth Planet. Inter.*, *25*(4), 297–356, doi:10.1016/0031-9201(81)90046-7.
- Fichtner, A., H. Bunge, and H. Igel (2006a), The adjoint method in seismology. I. Theory, *Phys. Earth Planet. Inter.*, *157*(1-2), 86–104, doi:10.1016/j.pepi.2006.03.016.

- Fichtner, A., H. Bunge, and H. Igel (2006b), The adjoint method in seismology. II. Applications: traveltimes and sensitivity functionals, *Phys. Earth Planet. Inter.*, *157*(1-2), 105–123, doi:10.1016/j.pepi.2006.03.018.
- Fichtner, A., B. L. N. Kennett, H. Igel, and H. Bunge (2009), Full seismic waveform tomography for upper-mantle structure in the Australasian region using adjoint methods, *Geophys. J. Int.*, *179*(3), 1703–1725, doi:10.1111/j.1365-246X.2009.04368.x.
- Fichtner, A., J. Trampert, P. Cupillard, E. Saygin, T. Taymaz, Y. Capdeville, and A. Villaseor (2013), Multiscale full waveform inversion, *Geophysical Journal International*, *194*, 534556, doi:10.1093/gji/ggt118.
- Flament, N., M. Gurnis, and R. D. Müller (2013), A review of observations and models of dynamic topography, *Lithosphere*, *5*(2), 189–210, doi:10.1130/L245.1.
- Fournier, A., G. Hulot, D. Jault, W. Kuang, A. Tangborn, N. Gillet, E. Canet, J. Aubert, and F. Lhuillier (2010), An introduction to data assimilation and predictability in geomagnetism, *Sp. Sci. Rev.*, *155*, 247–291, doi:10.1007/s11214-010-9669-4.
- French, S., V. Lekić, and B. Romanowicz (2013), Waveform tomography reveals channeled flow at the base of the oceanic asthenosphere., *Science (80-.)*, *342*(6155), 227–30, doi:10.1126/science.1241514.
- French, S. W., and B. A. Romanowicz (2014), Whole-mantle radially anisotropic shear velocity structure from spectral-element waveform tomography, *Geophysical Journal International*, *199*(3), 13031327, doi:10.1093/gji/ggu334.
- Ghelichkhan, S., and H.-P. Bunge (2016), The compressible adjoint equations in geodynamics: derivation and numerical assessment, *Int J Geomath*, *7*(1), 130, doi:10.1007/s13137-016-0080-5.
- Grand, S. P., R. van der Hilst, and S. Widiyantoro (1997), Global seismic tomography; a snapshot of convection in the Earth, *GSA Today*, *7*, 1–7.
- Guillocheau, F., D. Rouby, C. Robin, C. Helm, N. Rolland, C. Le Carlier de Veslud, and J. Braun (2012), Quantification and causes of the terrigenous sediment budget at the scale of a continental margin: a new method applied to the Namibia-South Africa margin, *Basin Res.*, *24*(1), 3–30, doi:10.1111/j.1365-2117.2011.00511.x.
- Hager, B. H., and M. Gurnis (1987), Mantle convection and the state of the earth’s interior, *Reviews of Geophysics*, *25*(6), 1277–1285, doi:10.1029/RG025i006p01277.
- Hartley, R. A., G. G. Roberts, N. J. White, and C. Richardson (2011), Transient convective uplift of an ancient buried landscape, *Nat. Geosci.*, *4*(8), 562–565, doi:10.1038/ngeo1191.

- Hoggard, M. J., N. White, and D. Al-Attar (2016), Global dynamic topography observations reveal limited influence of large-scale mantle flow, *Nature Geosci.*, doi:10.1038/ngeo2709.
- Höink, T., A. M. Jellinek, and A. Lenardic (2011), Viscous coupling at the lithosphere-asthenosphere boundary, *Geochemistry, Geophys. Geosystems*, *12*(10), doi:10.1029/2011GC003698.
- Höink, T., A. Lenardic, and M. A. Richards (2012), Depth-dependent viscosity and mantle stress amplification: implications for the role of the asthenosphere in maintaining plate tectonics, *Geophys. J. Int.*, *191*(1), 30–41, doi:10.1111/j.1365-246X.2012.05621.x.
- Horbach, A., H. Bunge, and J. Oeser (2014), The adjoint method in geodynamics: derivation from a general operator formulation and application to the initial condition problem in a high resolution mantle circulation model, *Int J Geomath*, *5*(2), 163–194, doi:10.1007/s13137-014-0061-5.
- Iaffaldano, G. (2012), The strength of large-scale plate boundaries: Constraints from the dynamics of the Philippine Sea plate since 5Ma, *Earth Planet. Sci. Lett.*, *357-358*, 21–30, doi:10.1016/j.epsl.2012.09.018.
- Iaffaldano, G., and H. Bunge (2009), Relating rapid plate-motion variations to plate-boundary forces in global coupled models of the mantle/lithosphere system: Effects of topography and friction, *Tectonophysics*, *474*(1-2), 393–404, doi:10.1016/j.tecto.2008.10.035.
- Iaffaldano, G., and H.-P. Bunge (2015), Rapid plate motion variations through geological time: Observations serving geodynamic interpretation, *Annual Review of Earth and Planetary Sciences*, *43*(1), 571592, doi:10.1146/annurev-earth-060614-105117.
- Iaffaldano, G., H.-P. Bunge, and T. H. Dixon (2006), Feedback between mountain belt growth and plate convergence, *Geology*, *34*(10), 893, doi:10.1130/g22661.1.
- Iaffaldano, G., H. Bunge, and M. Bücke (2007), Mountain belt growth inferred from histories of past plate convergence: A new tectonic inverse problem, *Earth Planet. Sci. Lett.*, *260*(3-4), 516–523, doi:10.1016/j.epsl.2007.06.006.
- Iaffaldano, G., T. Bodin, and M. Sambridge (2012), Reconstructing plate-motion changes in the presence of finite-rotations noise, *Nat. Commun.*, *3*(May), 1048, doi:10.1038/ncomms2051.
- Ismail-Zadeh, A., G. Schubert, I. Tsepelev, and A. Korotkii (2004), Inverse problem of thermal convection: numerical approach and application to mantle plume restoration, *Phys. Earth Planet. Inter.*, *145*(1-4), 99–114, doi:10.1016/j.pepi.2004.03.006.

- Japsen, P., J. M. Bonow, P. F. Green, J. A. Chalmers, and K. Lidmar-Bergström (2006), Elevated, passive continental margins: Long-term highs or neogene uplifts? new evidence from west greenland, *Earth and Planetary Science Letters*, *248*(12), 330 – 339, doi:<http://dx.doi.org/10.1016/j.epsl.2006.05.036>.
- Japsen, P., J. A. Chalmers, P. F. Green, and J. M. Bonow (2012a), Elevated, passive continental margins: Not rift shoulders, but expressions of episodic, post-rift burial and exhumation, *Glob. Planet. Change*, *90-91*, 73–86, doi:10.1016/j.gloplacha.2011.05.004.
- Japsen, P., J. M. Bonow, P. F. Green, P. R. Cobbold, D. Chiossi, R. Lilletveit, L. P. Magnavita, and A. Pedreira (2012b), Episodic burial and exhumation in NE Brazil after opening of the South Atlantic, *Geol. Soc. Am. Bull.*, *124*(5-6), 800–816, doi:10.1130/B30515.1.
- Jarvis, G. T., and D. P. McKenzie (1980), Convection in a compressible fluid with infinite prandtl number, *J. Fluid Mech.*, *96*(03), 515–583, doi:10.1017/S002211208000225X.
- Karato, S.-I. (2010), Rheology of the deep upper mantle and its implications for the preservation of the continental roots: A review, *Tectonophysics*, *481*(1-4), 82–98, doi:10.1016/j.tecto.2009.04.011.
- Karato, S.-I., and P. Wu (1993), Rheology of the Upper Mantle: A Synthesis, *Science*, *260*, 771–778.
- Kennett, B. L. N., E. R. Engdahl, and R. Buland (1995), Constraints on seismic velocities in the Earth from traveltimes, *Geophys. Journal-Oxford*, *122*(1), 108–124, doi:10.1111/j.1365-246X.1995.tb03540.x.
- Leng, W., and S. Zhong (2008), Controls on plume heat flux and plume excess temperature, *Journal of Geophysical Research*, *113*(B4), doi:10.1029/2007jb005155.
- Lithgow-Bertelloni, C., and P. G. Silver (1998), Dynamic topography, plate driving forces and the African superswell, *Nature*, *395*, 269–272, doi:10.1038/26212.
- Macgregor, D. S. (2012), Late Cretaceous-Cenozoic sediment and turbidite reservoir supply to South Atlantic margins, *Geol. Soc. London, Spec. Publ.*, *369*(1), 109–128, doi:10.1144/SP369.7.
- Matsuyama, I., J. X. Mitrovica, A. Daradich, and N. Gomez (2010), The rotational stability of a triaxial iceage earth, *Journal of Geophysical Research*, *115*, B05,401, doi:10.1029/2009JB006564.
- McNamara, A. K., and S. Zhong (2005), Thermochemical structures beneath Africa and the Pacific Ocean, *Nature*, *437*(7062), 1136–1139, doi:10.1038/nature04066.

- Mitrovica, J. X. (1996), Haskell [1935] revisited, *J. Geophys. Res.*, *101*(B1), 555, doi:10.1029/95JB03208.
- Mosca, I., L. Cobden, A. Deuss, J. Ritsema, and J. Trampert (2012), Seismic and mineralogical structures of the lower mantle from probabilistic tomography, *Journal of Geophysical Research*, *117*(B6), doi:10.1029/2011jb008851.
- Nakada, M., J. Okuno, K. Lambeck, and a. Purcell (2015), Viscosity structure of Earth’s mantle inferred from rotational variations due to GIA process and recent melting events, *Geophys. J. Int.*, *202*(2), 976–992, doi:10.1093/gji/ggv198.
- Nerlich, R., L. Colli, S. Ghelichkhan, B. Schuberth, and H.-P. Bunge (2016), Mantle convection models constrain central Neo-Tethys Ocean reconstructions, *Geophys. Res. Lett.*
- Oeser, J., H. Bunge, and M. Mohr (2006), Cluster Design in the Earth Sciences: TETHYS, in *High Perform. Comput. Commun. – Second Int. Conf. HPCC 2006, Munich, Ger., Lecture Notes in Computer Science*, vol. 4208, edited by M. Gerndt and D. Kranzlmüller, pp. 31–40, Springer, doi:10.1007/11847366_4.
- Panasjuk, S. V., B. H. Hager, and A. M. Forte (1996), Understanding the effects of mantle compressibility on geoid kernels, *Geophys. J. Int.*, *124*(1), 121–133, doi:10.1111/j.1365-246X.1996.tb06357.x.
- Parnell-Turner, R., N. White, T. Henstock, B. Murton, J. Maclennan, and S. M. Jones (2014), A continuous 55-million-year record of transient mantle plume activity beneath iceland, *Nat. Geosci.*, *7*(12), 914–919.
- Paulson, A., and M. A. Richards (2009), On the resolution of radial viscosity structure in modelling long-wavelength postglacial rebound data, *Geophys. J. Int.*, *179*(3), 1516–1526, doi:10.1111/j.1365-246X.2009.04362.x.
- Paulson, A., S. J. Zhong, and J. Wahr (2007), Limitations on the inversion for mantle viscosity from postglacial rebound, *Geophys. J. Int.*, *168*(3), 1195–1209, doi:10.1111/j.1365-246X.2006.03222.x.
- Pekeris, C. L. (1935), Thermal convection in the interior of the earth, *Geophys. J. Int.*, *3*(8), 343–367, doi:10.1111/j.1365-246X.1935.tb01742.x.
- Piazzoni, A. S., G. Steinle-Neumann, H. Bunge, and D. Dolejš (2007), A mineralogical model for density and elasticity of the Earth’s mantle, *Geochemistry, Geophys. Geosystems*, *8*(11), doi:10.1029/2007GC001697.
- Praeg, D., M. Stoker, P. Shannon, S. Ceramicola, B. Hjelstuen, J. Laberg, and a. Mathiesen (2005), Episodic Cenozoic tectonism and the development of the NW European passive continental margin, *Mar. Pet. Geol.*, *22*(9-10), 1007–1030, doi:10.1016/j.marpetgeo.2005.03.014.

- Richards, M. A., and B. H. Hager (1984), Geoid anomalies in a dynamic Earth, *J. Geophys. Res.*, *89*(B7), 5987, doi:10.1029/JB089iB07p05987.
- Rickers, F., A. Fichtner, and J. Trampert (2013), The IcelandJan Mayen plume system and its impact on mantle dynamics in the North Atlantic region: Evidence from full-waveform inversion, *Earth Planet. Sci. Lett.*, *367*, 39–51, doi:10.1016/j.epsl.2013.02.022.
- Ritsema, J., H.-J. Van Heijst, and J. H. Woodhouse (1999), Complex shear wave velocity structure imaged beneath Africa and Iceland, *Science (80-.)*, *286*(5446), 1925–1928, doi:10.1126/science.286.5446.1925.
- Ritsema, J., A. Deuss, H. J. van Heijst, and J. H. Woodhouse (2011), S40RTS: a degree-40 shear-velocity model for the mantle from new rayleigh wave dispersion, teleseismic traveltime and normal-mode splitting function measurements, *Geophys. J. Int.*, *184*(3), 1223–1236.
- Roberts, G. G., and N. White (2010), Estimating uplift rate histories from river profiles using african examples, *Journal of Geophysical Research: Solid Earth*, *115*(B2), n/a–n/a, doi:10.1029/2009JB006692, b02406.
- Sambridge, M., and K. Mosegaard (2002), Monte Carlo methods in geophysical inverse problems, *Reviews of Geophysics*, *40*(3), doi:10.1029/2000rg000089.
- Schaber, K., H. Bunge, B. S. A. Schuberth, R. Malservisi, and A. Horbach (2009), Stability of the rotation axis in high-resolution mantle circulation models: Weak polar wander despite strong core heating, *Geochemistry, Geophys. Geosystems*, *10*(11), n/a–n/a, doi:10.1029/2009GC002541.
- Schuberth, B. S. A., H.-P. Bunge, G. Steinle-Neumann, C. Moder, and J. Oeser (2009a), Thermal versus elastic heterogeneity in high-resolution mantle circulation models with pyrolite composition: High plume excess temperatures in the lowermost mantle, *Geochemistry, Geophys. Geosystems*, *10*(1), doi:10.1029/2008GC002235.
- Schuberth, B. S. A., H.-P. Bunge, and J. Ritsema (2009b), Tomographic filtering of high-resolution mantle circulation models: Can seismic heterogeneity be explained by temperature alone?, *Geochemistry, Geophys. Geosystems*, *10*(5), doi:10.1029/2009GC002401.
- Schuberth, B. S. A., C. Zaroli, and G. Nolet (2012), Synthetic seismograms for a synthetic Earth: long-period P- and S-wave traveltime variations can be explained by temperature alone, *Geophys. J. Int.*, *188*(3), 1393–1412, doi:10.1111/j.1365-246X.2011.05333.x.
- Schuberth, B. S. A., C. Zaroli, and G. Nolet (2015), Traveltime dispersion in an isotropic elastic mantle: strong lower-mantle signal in differential-frequency residuals, *Geophysical Journal International*, *203*(3), 2099–2118, doi:10.1093/gji/ggv389.

- Seton, M., R. D. Müller, S. Zahirovic, C. Gaina, T. Torsvik, G. Shephard, A. Talsma, M. Gurnis, M. Turner, S. Maus, and M. Chandler (2012), Global continental and ocean basin reconstructions since 200 Ma, *Earth-Sci. Rev.*, *113*(3–4), 212–270.
- Shephard, G., H. Bunge, B. S. A. Schuberth, R. D. Müller, A. S. Talsma, C. Moder, and T. C. W. Landgrebe (2012), Testing absolute plate reference frames and the implications for the generation of geodynamic mantle heterogeneity structure, *Earth Planet. Sci. Lett.*, *317-318*, 204–217, doi:10.1016/j.epsl.2011.11.027.
- Simmons, N. a., S. C. Myers, G. Johannesson, and E. Matzel (2012), LLNL-G3Dv3: Global P wave tomography model for improved regional and teleseismic travel time prediction, *J. Geophys. Res. Solid Earth*, *117*(10), 1–28, doi:10.1029/2012JB009525.
- Simmons, N. A., S. C. Myers, G. Johannesson, E. Matzel, and S. P. Grand (2015), Evidence for long-lived subduction of an ancient tectonic plate beneath the southern Indian ocean, *Geophysical Research Letters*, *42*(21), 92709278, doi:10.1002/2015gl066237.
- Stanley, J. R., R. M. Flowers, and D. R. Bell (2015), Erosion patterns and mantle sources of topographic change across the southern African Plateau derived from the shallow and deep records of kimberlites, *Geochemistry, Geophys. Geosystems*, *16*(9), 3235–3256, doi:10.1002/2015GC005969.
- Steinberger, B., and R. J. O’Connell (1997), Changes of the Earth’s rotation axis owing to advection of mantle density heterogeneities, *Nature*, *387*(6629), 169–173, doi:10.1038/387169a0.
- Stille, H. (1919), Die begriffe orogenese und epirogenese, *Zeitschrift der Deutschen Geologischen Gesellschaft*, *71*, 164–208.
- Stixrude, L., and C. Lithgow-Bertelloni (2011), Thermodynamics of mantle minerals - II. Phase equilibria, *Geophys. J. Int.*, *184*(3), 1180–1213, doi:10.1111/j.1365-246X.2010.04890.x.
- Stoker, M. S., and P. M. Shannon (2005), Neogene evolution of the NW european atlantic margin: Results from the STRATAGEM project, *Mar. Pet. Geol.*, *22*(9), 965–968.
- Styles, E., D. R. Davies, and S. Goes (2011), Mapping spherical seismic into physical structure: biases from 3-D phase-transition and thermal boundary-layer heterogeneity, *Geophysical Journal International*, *184*(3), 13711378, doi:10.1111/j.1365-246x.2010.04914.x.
- Tarantola, A. (1988), Theoretical background for the inversion of seismic waveforms, including elasticity and attenuation, *Pure and Applied Geophysics*, *128*(1), 365–399, doi:10.1007/BF01772605.

- Tarduno, J. A., H. Bunge, N. H. Sleep, and U. Hansen (2009), The bent Hawaiian-Emperor hotspot track: inheriting the mantle wind., *Science* (80-.), *324* (5923), 50–3, doi:10.1126/science.1161256.
- Thoraval, C., and M. A. Richards (1997), The geoid constraint in global geodynamics: viscosity structure, mantle heterogeneity models and boundary conditions, *Geophys. J. int.*, *131* (1), 1–8, doi:10.1111/j.1365-246X.1997.tb00591.x.
- Tromp, J., C. Tape, and Q. Liu (2005), Seismic tomography, adjoint methods, time reversal and banana doughnut kernels, *Geophys. J. Int.*, *160* (1), 195–216, doi:10.1111/j.1365-246X.2004.02453.x.
- Vynnytska, L., and H.-P. Bunge (2014), Restoring past mantle convection structure through fluid dynamic inverse theory: regularisation through surface velocity boundary conditions, *Int J Geomath*, *6* (1), 83–100, doi:10.1007/s13137-014-0060-6.
- Weismüller, J., B. Gmeiner, S. Ghelichkhan, M. Huber, L. John, B. Wohlmuth, U. Rüde, and H.-P. Bunge (2015), Fast asthenosphere motion in high-resolution global mantle flow models, *Geophys. Res. Lett.*, *42* (18), 7429–7435, doi:10.1002/2015GL063727.
- Wiens, D. A., and S. Stein (1985), Implications of Oceanic Intraplate Seismicity for Plate Stresses, Driving Forces and Rheology, *Tectonophysics*, *116*, 143–162, doi:10.1016/0040-1951(85)90227-6.
- Wilson, J. W. P., G. G. Roberts, M. J. Hoggard, and N. J. White (2014), Cenozoic epeirogeny of the arabian peninsula from drainage modeling, *Geochem. Geophys. Geosyst.*, *15* (10), 3723–3761.
- Winterbourne, J., N. J. White, and A. Crosby (2014), Accurate measurements of residual topography from the oceanic realm, *Tectonics*, *33* (6), 9821015, doi:10.1002/2013TC003372.
- Zaroli, C., M. Sambridge, J.-J. Lvque, E. Debayle, and G. Nolet (2013), An objective rationale for the choice of regularisation parameter with application to global multiple-frequency s-wave tomography, *Solid Earth*, *4* (2), 357371, doi:10.5194/se-4-357-2013.
- Zhong, S. J., D. A. Yuen, L. N. Moresi, and M. G. Knepley (2015), *Numerical Methods for Mantle Convection, Treatise on Geophysics*, vol. 7: Mantle Dynamics, chap. 7.05.1, pp. 197–222, 2nd edition ed., Elsevier, doi: 10.1016/B978-0-444-538.
- Zhou, Y., F. A. Dahlen, G. Nolet, and G. Laske (2005), Finite-frequency effects in global surface-wave tomography, *Geophys. J. Int.*, *163* (3), 1087–1111, doi: 10.1111/j.1365-246X.2005.02780.x.

Chapter 7

Outlook

Geodynamic retrodictions are just starting to be computationally feasible, and much work is still needed. A first critical point is the choice of a suitable misfit function, i.e., how to best compare seismic and geodynamic models. It is important to stress that seismic tomography doesn't provide a direct observation of the Earth's interior but rather a best-fitting model, the solution of an inverse problem of its own. Additional work should be done on how and to what extent the conversion of a tomographic image to a temperature field through a model of mantle mineralogy is affected by the uncertainties of both seismic and thermodynamic models.

Also of importance is the knowledge of the past history of plate motions. Assimilating past plate velocities regularizes the inverse problem and strongly reduces the null space. Kinematic models of past plate motions, however, suffer from uncertainties on many levels, in particular from finite-rotation noise, which affects plate velocities instantaneously, and from the impossibility to choose a true "mantle" frame of reference, which potentially introduces a long-term drift. Given the key role of plate motions for the convergence of the adjoint method, this issue needs to be explored further.

A final point that needs careful consideration is which type of geologic data provides a better opportunity to constrain geodynamic models. In particular, any geodynamic model is bound to capture only some of the processes that influence the geologic record, and as such the output of a geodynamic model may not be readily comparable with geological observations. On the other hand, geological observations are mostly made at a local scale of a few meters to a few kilometers, but they need to be examined at the regional or even continental scale for the contribution of deep mantle processes to become apparent. Tackling this problem requires a truly interdisciplinary and multi-scale approach by scientists with a strong background in both geology and geophysics.

Acknowledgments

As obvious as it may seem, let me state here clearly that this work would not have been in the least possible without the fundamental contribution of many other people. First and foremost I want to heartily thank my supervisor, Hans-Peter Bunge. Peter, you have been a constant source of inspiration and a big spur for self-improvement. I learned many lessons thanks to you and I hope to be able to pass on this knowledge to future generations of PhD students. My sincere thanks also go to two other quasi-supervisors of mine, Andreas Fichtner and Giampiero Iaffaldano, for their thoughtful advices about geoscience, academia and life.

I am grateful to the THESIS program of the Elite-Netzwerk Bayern and to the SAMPLE program of the DFG for providing most of the funding; to Helen Pfuhl, Yvonne Neßler and Elena Verbovetska for making sure that those fundings were arriving in my pockets at a reliable monthly rate; and to Greta for being the best manager any project can dream of having.

There are many people I'm scientifically in debt with: everyone in the geophysics section, in particular Siavash Ghelichkhan, Kasra Hosseini Zad, Rainer Nerlich, Thomas Chust, Lion Krischer, Jens Weismüller and Bernhard Schubert for many helpful discussions and for helping me to better understand other fields of the geosciences. My gratitude also goes to Jens Oeser for providing an impeccable computing infrastructure. I am deeply thankful to Céline Hadziioannou who has been an invaluable source of inspiration both as a colleague and as a friend. Thank you to all my former officemates for your company and for always keeping a nice atmosphere in the office: Christoph, André, Roberta, Moritz, Thomas, Xiangyu, Lion, Mafe, Felix and Johannes. You're all gone now and I'm the only one left in this big, freezing, crumbling office. Which reminds me to thank Heiner Igel who bought us some electric heaters and gave to our office the necessary level of Gemütlichkeit. I would now be Dr. Icecube if it weren't for your kindness. But jokes apart, you also showed me the importance of openness and collaborations in science, and for this you have my gratitude and my profound respect. Fundamental to this work has been my introduction to the beauty of geology, thanks to Anke Friedrich, Sara Carena, Steffi Rieger, Markus Hoffman, Simon Kübler, Alessandro Verdecchia and all the people in the geology section.

A lot of productive ideas had their inception in the course of a series of joint geology-

geodynamics workshops held in Luisenstraße, where some fundamental contributions were made by visiting professors Dietmar Müller, Seth Stein and Carol Stein, to whom I am also very much in debt. My geologic knowledge of thermochronology, basin analysis, reflection seismology, petrography and geomorphology increased exponentially thanks to the interaction with the PIs, the PhD students and the guests from SAMPLE, in particular Ulli Glasmacher, Michael Weber, Leni Scheck-Wenderoth, Bob Trumbull, René Gassmüller, Stefanie Hempel, Sebastian Kollenz, François Guillocheau, Peter Hackspacher and Peter Japsen. I'm also in debt with Brian Kenneth for his support, his insightful comments and his immense geophysical knowledge. I also want to thank Julia Wiebe, Stuart Clark, Ingo Stotz, Grace Shephard and Maria Chiara Bianchi.

During this years I also dabbled in volcanology and, although not much came out of that scientifically, I had the opportunity to meet many wonderful people: Oryaëlle, Ulli, Corrado, Paul, Miguel, Fabian, Jeremie, Guilheme and Betty.

I could not have survived this PhD, in particular in the first years, without the Italian connection: Roberta, Corrado, Dario, Teresa, Irene, Ilaria, Cristian, Roberto, Daniele, Edoardo, Valeria, Laura e Danilo. Grazie per aver tenuto un'alito d'Italia nella mia vita.

And since man shall not live by bread alone, let me thank here also all my lunchmates over the years, with a particular mention to Steffi because she insisted that I do so.